DATA DRIVEN APPROACHES FOR IMPROVING QUANTIFICATION ACCURACY IN SURFACE ENHANCED RAMAN SPECTROSCOPY SENSING

by

SAKSHI SARDAR

A dissertation submitted to the

School of Graduate Studies

Rutgers, The State University of New Jersey

in partial fulfillment of the requirements

for the joint degree of

Doctor of Philosophy

Graduate Program in Electrical and Computer Engineering and,

Quantitative Biomedicine

Written under the direction of

Laura Fabris and Mehdi Javanmard

and approved by

_____

_____

_____

_____

New Brunswick, New Jersey

OCTOBER, 2019

ABSTRACT OF THE DISSERTATION

Data Driven Approaches for Improving Quantification Accuracy in Surface Enhanced Raman Spectroscopy Sensing

by Sakshi Sardar

Dissertation Director: Laura Fabris and Mehdi Javanmard

Surface enhanced Raman spectroscopy (SERS) is one of the most sensitive and selective techniques available. In the past couple of decades numerous applications of SERS for the development of sensors have been reported. Even though it is an excellent qualitative technique, its full quantitative potential has yet to be realized. One of the major categories of SERS based sensors are heterogeneous sensors, based on nanostructured substrates. The performance of these sensors is highly dependent on the distance between the enhancing nanostructure and the analyte, which in turn influences its sensitivity, and the reproducibility of the substrates. These factors play a very important role in controlling the SERS intensity associated with the sensors. We aimed to address these issues through different methodologies to improve the performance of SERS-based sensors. SERS enhancements achieved with the heterogeneous platforms are highly dependent on the surface morphology of the substrates used. For low-cost substrates, which are usually prepared from bottom-up approaches, control over the surface properties is low, resulting in variability among the substrates as well as at different locations within the same substrate. In order to overcome the reproducibility

issue, we developed a dual-modality multi-site sensing methodology. In this methodology, we intentionally induced diversity on the substrate to modulate the SERS signal from analyte . Electrochemistry was combined with SERS for dual modality sensing to improve precision by adding redundancy and encoding features, thus increasing measurement robustness and predictability. This technique works by calibrating the SERS response with respect to the active surface area, a parameter known to be proportional to charge, which can be estimated via electrochemical measurements. The dual-modality multi-site measurement demonstrates at least 2.8x improvement in assay precision compared to the traditional single-site Raman measurements. The technique yields overall improved precision of measurement and is not limited to any particular SERS substrate or geometry, and thus can be adapted and incorporated readily in any SERS sensing assay .

Raman spectral variation can be analyzed with another perspective where the pattern obtained for the same analyte for different spot measurements provide information about the spot. In other words, the local environment at the measurement spot have bearing on the Raman spectrum. For instance, the location and orientation of the molecule on the substrate contribute to Raman spectral signature. In addition, the location, orientation, and interaction of the nanoparticles used to prepare the substrates also affect the spectral signature . As a result, the peak intensities and positions are modulated by these factors. Thus, in turn, a Raman spectrum contains all this information, and only by decoding it we can achieve a distinct picture of the local environment, which includes the analyte molecules. In order to understand the contribution of analyte concentration in the spectra, we carried out supervised classification using support vector machines. We found that the classification accuracy can be increased by properly incorporating different features contained in the spectrum.

Selectivity and sensitivity of the sensor are crucial properties for designing a SERS system. The system has to be optimized to achieve acceptable sensitivity and selectivity towards the analyte of interest. In order to improve upon these two properties, we chose phenylalanine (Phe), an biomarker for Phenylketonuria(PKU), an in-born metabolic

error that leads to errors in the metabolism of Phe. Patients with PKU can have complications like intellectual disability, microcephaly, severe mental retardation, motor deficits, eczematous rash, autism, difficulty swallowing, seizures/convulsions, developmental problems, aberrant behavior, dystonias, dyskinesias, hyperreflexia, or spasticity, and psychiatric symptom. The treatment usually involves reduce dietary Phe intake and regular monitoring of Phe levels. The sensors were designed to detect Phe using different sensing approaches.

In conclusion, our work addresses important properties and issues that can assist in manufacturing better SERS-based sensors.

Acknowledgements

First of all, I would like to thank my advisors, Dr. Fabris and Dr. Javanmard. Thank you for your guidance and willingness to mentor me. I have learned a lot from both of you in the past four years of my graduate studies. I am very fortunate to have great advisors who have helped me to realize the potential I have through constant support, guidance and challenges. You have taught me the importance of well-rounded research to solve the problems that can have very impactful implications and explore new ideas. You both are the best mentors I could have asked for.

I would also like to thank all the members of Dr. Fabris and Dr. Javanmards group, Azam, Tuan, Kavya, Manjari, Riyanka, Hao, Karan, Supriya, Ted, Matina, Kholud, Maria, Pengfei, Zhongtian, Jianye and Prateek for their help and support with different projects and techniques over the years. I am thankful for their willingness to suggest ways to overcome the obstacles that I faced during various stages of research. I consider myself privileged to be a part of these groups.

I would also like to thank Shawn and Damien for their help with Raman spectroscopy and AFM. I would also like to express my thankfulness to Dr. Chhowalla and his group for their invaluable help.

I am thankful to Christy, John, Arletta, Tea and Pam for their help with different tasks at ECE. They have been a tremendous help.

Thank you Paul, Shashank, Priya, Krishnaveni, Rohit and Tejas for your constant help and support over the past year. Thank you for your motivation when the studies seemed difficult.

Last but not the least, I would like to thank my family and God. I am where I am because of their love and support. I would like to dedicate this work to my parents.

Table of Contents

List of Tables

List of Figures

Chapter 1

Introduction

1.1 Background

Surface enhanced Raman spectroscopy is one of the most sensitive and specific techniques available. Virtually, all polyatomic molecules have characteristic vibrational spectra through the oscillating induced dipoles. These induced dipoles have characteristic vibrational frequencies giving rise thus giving rise to high specificity detection through Raman shift information and the associated intensity [1, 2]. Rapid developments in the field of nanoscience in past couple of decades have led to an acceleration in the rate of sensor design employing SERS. These sensors find application in various fields ranging from materials science, biochemistry, biosensing, catalysis, and electrochemistry [3] . The unique high selectivity of Raman allows for analysis of multiple components simultaneously, which enables the design of multiplexed sensing assays [4] .These are great advancements in the field of commercially available Raman spectrophotometers, even the portable ones, which could be envisioned to soon become deployable in low-resource settings. Faster analysis and ease of sample preparation are other advantages associated with these sensors. [5] In this chapter I will discuss the basic principles of Raman scattering and SERS to understand their importance in sensors design. These sections will be followed by the scope of the thesis.

1.2 Raman Scattering

Raman scattering is the inelastic scattering of photons which occurs when the energy of the incident photon is different from that of an emitted photon. The energy difference corresponds to a transition between two vibrational/rotational states in the molecule.

The scattering process in Raman is instantaneous and does not necessarily require the existence of an electronic transition resonant with the incident wavelength. In other words, in Raman scattering the absorption of the incident photon excites the molecule to an intermediate virtual state. If this virtual state corresponds to an actual electronic state, resonant scattering occurs, further increasing the efficiency of the process. Raman scattering can broadly be divided into Stokes and anti-Stokes processes.

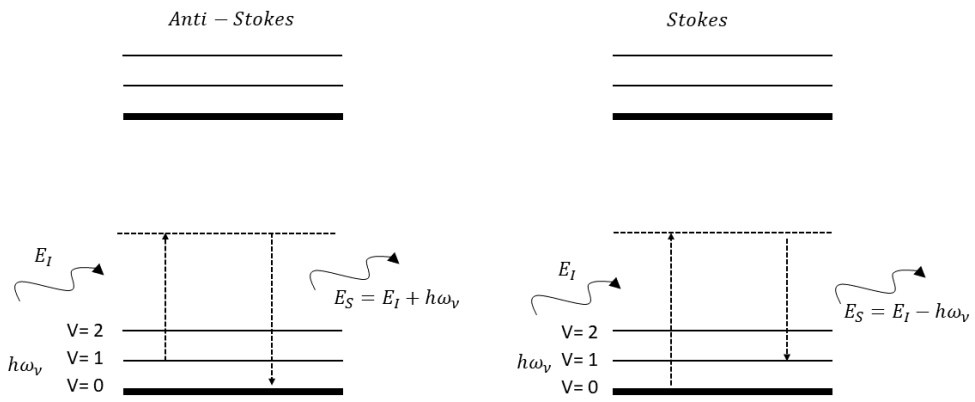

Figure 1.1: Simplified Jablonski diagram showing the Stokes and anti-Stokes Raman scattering processes.

Stokes process occurs when the scattered photon has lower energy than the incident photon, that is, when the incident photon excites the molecule from the ground state to a virtual state, followed by a spontaneous emission of a scattered photon that brings the molecule to an excited vibrational mode. The energy of the scattered photon is lower than that of the incident one and this difference provides information about the vibrational state of the molecule. Anti-Stokes processes take place when the energy of the scattered photon is higher than that of the incident one. they usually occur when the molecule is excited to a virtual state originally from one of the excited vibrational states and relaxes to the ground state after spontaneous scattering. This leads to the scattered photon having higher energy that the incident one. The intensity of

anti-Stokes scattering bands is much lower than that of the Stokes scattering. The measured Raman shift measures the energy lost by the photon in the scattering process and is usually expressed in wavenumbers. The Raman spectrum is the variation of the scattered intensity with energy or wavelength of Raman scattering for a given incident wavelength [5].

1.3 Surface Enhanced Raman Scattering

Surface enhanced Raman scattering is the enhancement in the Raman signal of a molecule when it is placed in close proximity to a plasmonic nanostructure. Plasmonic structures are good substrates for SERS. For a metal to be plasmonic, the real part of the dielectric function should be negative, preferable in range of -1 to -20 and the imaginary part of the dielectric contact should be as small as possible (negative). These conditions are met readily for metals like silver, gold, and copper. However, given various properties, such as stability and ease of surface functionalization, gold finds more applications compared to the others. SERS intensity is proportional to the laser intensity and the normal Raman cross section of the analyte. However, these intensities can be affected by enhancements experienced by the molecule. These enhancements usually come from two multiplicative contributions, namely, electromagnetic and chemical enhancement. Electromagnetic enhancements are generally due to coupling of the incident and Raman electromagnetic fields with the SERS substrate. Chemical enhancements occur when the molecule is chemisorbed on the surface leading to change in its electronic polarizability properties. Such changes can induce resonant Raman scattering as well [6].

1.4 SERS Substrates

There are three main classes of SERS substrates: Metallic nanostructures in solution, metallic nanostructures supported on a planar surface, and metallic electrodes [5, 7]. There have been extensive developments in the area of metallic colloids. The most common ones involve reduction of metal salts for chemical synthesis [7]). In addition

to chemical synthesis, metallic colloids could be prepared through physical methods like pulsed laser ablation of noble metal in liquid media [5]. The metallic nanostructures can be synthesized in different sizes and morphologies using different reaction condition. The size of the particles plays a crucial role in the SERS enhancements, enhancements, leading them to increase with the size of nanoparticles up to a certain size and then to decrease again. The nanostructures shape also has a bearing on the resulting enhancement. For instance, certain nanoparticles such as nanostars, which possess sharp spikes that lead to the formation of hot spots, give much higher enhancements [8, 9]. The metal colloid is usually stabilized using molecular species that form a coating around the nanoparticles and prevent the nanostructures from coalescing [5]. SERS substrates can be created on plan surfaces through top-down and bottom-up approaches. Bottom-up approaches include functionalization of substrates with a linker molecule that can immobilize the nanoparticles on the surface. The identity and functional groups of these linker molecules depend on the composition of the surface and that of the nanostructure. For gold, there are different functionalization ligand having amino, thiol, or carboxyl groups. These nanoparticles can further be functionalized for the specific purposes with appropriate surface functionalization [10] .Functionalization of planar substrates can be carried out through drop-casting or dip-coating [5, 7]. These substrates can also be prepared by using nanolithography and nano-imprint lithography techniques [5].

1.5 Scope

In order to create good SERS substrates there are a number of factors that must be considered. Intensity response for an analyte depends on the adsorption efficiency and analyte concentration (surface coverage). Another important aspect is the distance of the analyte from the surface as the response decreases drastically when the separation between analyte and the substrate increases. The orientation of a molecule enhances different Raman peaks differently. Sometime adsorption leads to modifications in the intrinsic Raman polarizability of the molecule. All these factors lead to variability in the SERS response making the quantification of an analyte difficult [6]. SERS is an

excellent qualitative technique providing high specificity and sensitivity. However, due to lack of proper control over the different factors mentioned above, achieving quantification in analyte detection proves challenging. With the projects described in this dissertation, we address some of these issues through multiple approaches. In Chapter 2, we address the issue of quantification through the implementation of a novel dual-modality multi-site sensing approach. One of the major hurdles with SERS based sensors is the reproducibility in morphology and optical response achievable in low cost substrates. Lack of reproducibility among substrate leads to variability in SERS enhancement, thus rendering quantification difficult and hindering the translation of these platforms into the ones that could find application in real world situations. We believe that this is an area holding SERS back from realizing its full potential in the sensing field. With the development of this new methodology, we hope to advance the field of SERS quantification and provide a stepping stone for more robust quantification approaches and eventually enable quantitative SERS measurements with high accuracy and precision. When combined with portable Raman spectrometers, such sensors could find application in low-resource setting. In order to improve the quantification capability of the system, we induce diversity on the SERS substrate through intentional induction of diversity. This diversity leads to modulation in the Raman response for a same analyte concentration. Not only this, we keep track of the diversity induced through electrochemical measurements. We chose to induce diversity through the concentration of nanoparticles being used for the substrate preparation. However, there are other ways of inducing diversity, for instance, through the size of the nanoparticles being used. We found that as we increased the concentration of nanoparticles, the Raman intensity from the analyte also increased and so did the charge measured using coulometry. Important observations in the study were the trade-off between the error associated with the measurement and the signal intensity. The substrate with lower concentration of nanoparticles had lower Raman intensity but the error associated with the measurements was also low. As we increased the concentration, the intensity increased but so did the error. Despite this trade-off, we find linear correlation between charge and Raman intensity for different nanoparticle concentrations but for the same

analyte concentration. There are multiple advantages of this approach. With this approach, we can overcome the issue of reproducibility associated with low-cost substrates. Any changes on the surface could be monitored through the electrochemical parameters and, based on the response from the calibration curves for that analyte, we can predict where the intensity would be. Another advantage of this approach is that it is agnostic to the SERS substrate or the analyte. Thus, it is a generalizable approach that can be followed for quantification on substrates made out of different morphology of nanoparticles.

In Chapter 3, We worked on developing a heterogeneous SERS sensor for detection of phenylalanine. Phenylealanine (Phe) was chosen as it is a biomaker for phenylketonuria (PKU). PKU is an in-born metabolic error which leads to error in Phe metabolism. Patients with PKU can have elevated levels of Phe in their blood with severe ensuing complications, especially related to brain damage and dysfunctions. High levels of Phe in blood streams eventually lead to elevated levels of Phe in the brain altering the transport of other important amino acids to and from the brain. These effects taken in combination lead to dopamine deficiency, neurotransmitter dysfunction, and issues with protein synthesis. These primary effects lead to secondary complications like intellectual disability, microcephaly, sever mental retardation, motor deficits, eczematous rash, autism, difficulty swallowing, seizures/convulsions,, developmental problems, aberrant behavior, dystonias, dyskinesias, hyperreflexia, or spasticity, and psychiatric symptom [11–13]. Therefore, children suffering from PKU have to be put on treatment as soon as possible. The treatment usually involves controlling the intake of dietary Phe. Parents have to weigh everything the child eats or eliminate certain foods entirely. It is not just about cutting down certain foods, the child also needs to reach the prescribed daily intake of Phe or else the low levels of Phe can trigger muscle breakdown, which in turn elevates the concentration of Phe in the bloodstream again. PKU is a rare disease, occurring on overage once per 10,000 births in the UK, with different rates in different regions. European guidelines on PKU prescribes that the blood Phe levels should be monitored weekly for children under 1 year of age, once every fortnight for children between the age 1 to 12, monthly for adolescents and adults, and twice a

week for pregnant women [14]. Currently, the blood is usually analyzed using expensive instrumentation requiring highly trained personnel. In this project we develop a SERS sensing platform for detecting Phe, characterized by high simplicity and low cost. Importantly, we aimed to detect Phe in blood, which is much less invasive and be easily performed by the patient. We based this assay on our novel multi-site approach. We created the multi-site component by varying the pH of the analyte solution and the nanomaterials used for the making the sensor. SERS intensities are highly dependent on the orientation of the molecular analyte on the SERS substrates. Certain orientations can enhance peaks by several orders of magnitude while certain orientations could reduce them or even eliminate them altogether. We modulated this property by changing the pH of analyte solution. This property can also be modulated by choosing the properties of the nanomaterial employed. The interaction of molecular groups with the underlying substrate is also dependent on the composition of the nanostructures, thus providing another parameter for modulation. With the ability to modulate these features, different modes can be enhanced by different magnitudes on different substrates for the same analyte. We hypothesize that this process can help in detecting the target molecule in a complex matrix against other molecules. Our results show that the multi-site approach could provide a way to detect an analyte by validating its presence through different peak enhancements on different substrates and at different pH. Future steps would entailing detecting it in presence of similarly structured molecules. This work could provide a solid foundation for label-free detection of analytes through the multi-site approach. In Chapter 4, we address the issue of SERS quantification through machine learning. As mentioned before, the intensity of SERS signals varies with the substrate features if those are not uniformly distributed, which is usually the case for low cost substrates. In addition, the coverage and distribution could vary given the incubation condition variations from one day to another unless the environment is tightly controlled. Intensity variation could also be introduced through the location of analyte on the nanostructure, especially for anisotropic particles like nanostars or closely coupled nanostructures. Nanostars and coupled nanostructures provide sharp

tips and gaps, respectively, that have hot spots. Hot spots are characterized by intense, localized electromagnetic fields associated, which lead to higher enhancements in SERS signal compared to the remaining regions on the nanostructure. Thus, this is an excellent way to enhance the signal and achieve low limits of detection. Apart from this, even in case of the uniform nanostructure like spheres, there are still variations in the intensity measurements given to the possible coupling between the particle and the substrate and among the nanoparticles, thus exposing the analytes to different electromagnetic fields and causing different intensity enhancements for an analyte. As could be seen, there are numerous factors that affect the way and the degrees by which intensities are enhanced. All these factors contribute to variation in the SERS spectrum,thus, it encompasses the state of the system. In other words, the spectrum will be characterized by spectral signatures that carry information about the local environment of the analyte. The information about the enhancements, the orientation and location of analyte, orientation and location of nanostructure is embedded in the spectrum from that point. Given the multi component nature of a Raman spectrum, our approach could allow us to extract different combinations of signatures associated with the analyte for an individual sensing platform. This in turn could assist in classificating the analyte concentration on the sensor, if we can identify a way to decode that information to reveal the underlying local environment at the measurement spot. We started with analysis to classify the concentration of an analyte. With this goal in mind, we used machine leaning algorithms like support vector machines with quadratic kernel and decision trees to show that combining the information extracted from the Raman spectra can provide a way to classify concentration of an analyte through single point Raman measurements. Based on the SERS process involved in the system, we decided to work with few characteristic vibrations of 4-aminotiophenol molecule. In SERS there are shifts in the Raman characteristic peak positions because of local environment effects on the molecule. Therefore, we had to extract the peak intensity for a particular vibration from a small range Raman shift values around the exact peak from the pure analyte . In addition, pre-processing has to be done while taking into account

the physical phenomena associated with each measurement. We find that using machine learning can improve the classification accuracy depending upon the processing done before training the data. In addition, we find that by adding multiple peaks for analysis can increase the classification accuracy

Chapter 2

Dual-Modality Multi-Site Sensing

2.1 Introduction

Accurate quantification of analytes using surface enhanced Raman spectroscopy (SERS) is a desired, yet unfulfilled, ability that could enable a plethora of diagnostic- and defense-related applications. The major hurdles to overcome to achieve this goal the high manufacturing costs to produce highly ordered and reproducible substrates and, the low reproducibility of substrates produced through low cost methods. A technology that can set industry standards for manufacturing/ processing of SERS substrates is still yet to be achieved. A dual modality multi-site sensing approach was developed that overcomes the limitations experienced when fabricating bottom-up, reproducible, sensitive, and low-cost SERS substrates. Electrochemistry was combined with SERS for dual modality sensing to improve precision by adding redundancy and encoding features, thus in-creasing measurement robustness and predictability. This technique works by calibrating the SERS response with respect tothe active surface area, a parameter known to be proportional to charge, which can be estimated via electrochemical measurements. The dual-modality multi-site measurement demonstrates at least 2.8x improvement in assay precision compared to the traditional single-site Raman measurements. The technique yields overall improved precision of measurement and is not limited to any particular SERS substrate or geometry, and thus can be adapted and incorporated readily in any SERS sensing assay

The integration of biosensors into various industries can transform the ability to monitor personal and public health, food safety, and the environment. [15] The research

community has already developed a plethora of sensors that have pushed detection limits down to femtomolar and even attomolar concentrations by utilizing diverse sensing modalities. In particular, among various modalities, high sensitivity and specificity has been realized using surface enhanced Raman spectroscopy (SERS). The selectivity of this technique can be attributed to the characteristic vibrations of a molecule, which depend not only on its intrinsic molecular structure but also on its orientation with respect to the surface of the sensing plat-form. This information can be very useful in biomarker analysis. [16–18] The Raman probe can also be used as a biomolecule receptor to provide intensity variation or even characteristic spectral changes to report analyte binding events. [18] Given the above reasons, SERS has emerged as an excellent tool for detection and characterization and has been a workhorse in qualitative sensing. However, for quantitative measurements, due to variability in measurements from one site to another on the same substrate, as a consequence of nanoparticle clustering and variation in analyte, orientation on the substrate, averaging is required, and exact concentration estimates always strongly depend on the presence of internal standards and ad hoc calibration curves. The nanoscale properties of the entire SERS substrate are often difficult to obtain given its macroscopic scale. Also, the mobility of atoms on noble metal surfaces and the reorganization of the nanoparticles are well-studied phenomena which can add to the complexity. Another issue to take into account is the enhancement factor (EF) of the substrate, which should be kept high and reproducible within and among plat-forms. To calculate EFs in SERS it is necessary to closely determine the active surface area of the sensor to estimate the number of molecules contributing to the SERS signal at any given location. This number is difficult to quantify, especially for complex substrate morphology. The majority of the SERS substrates suffer from spot to spot variability, substrate-to-substrate variability, instability, and reduced shelf life, and the analyte of interest can be detected upon entering the SERS active area of the substrate. Therefore, even though the end users of this technology are mainly concerned with detection limit and dynamic range of the sensor, the manufacturers need also to ensure batch-to-batch EF reproducibility and extended shelf life. [19, 20] Furthermore, they need to be able to accurately and precisely determine EF values for

their substrates, which can be a substantial hurdle when dealing with complex surfaces, which is often the case for low-cost SERS substrates. To determine SERS EFs, one has to take into account the following equation:

$$EF = \frac{I_{SERS}/N_{Surf}}{I_{RS}/N_{Vol}} \tag{2.1}$$

Where, $I_{SERS}$is the Raman intensity in presence of nanoparticles, N_{surf} is the number of molecules probed, I_{RS} is the Raman signal intensity, and N_{vol} is the number of probed molecules in the absence of nanoparticles. To calculate N_{vol} we need to use the equation $N_{vol} = C_{RS}V$, where V is the scattering volume and C_{RS} is the concentration of analyte used. [21] One should expect an increase in the intensity of Raman signal with increase in surface roughness as the number of molecules capable of physisorbing or chemisorbing to the surface increases, provided that the surface has not reached its jamming limit or the analyte in the solution itself has been not been fully exhausted. The resulting Raman signal is further enhanced by the field enhancement near the nanosized structures, with higher roughness (or smaller radius of curvature for the nanoparticles) producing the highest enhancements. Based on this rationale, the intensity of a SERS signal should always display a correlation with the surface area of the substrate. We used electrochemical techniques to obtain information about the available geometric surface area. This work also aims to address the issue of calculating exact EF by proposing a novel method in which electrochemical measurements are employed in-conjunction with Raman measurements to precisely correlate the signal intensity of SERS substrates built on screen printed electrodes directly to the surface areas evaluated electrochemically, thus avoiding the hurdle of estimating EFs for each of them.

Electrochemical techniques are also extremely sensitive and suitable for designing low cost detection devices. In addition, they can similarly be used for analyte quantification. [22] However, baseline drifts and sensitivity changes during the assay are common issues associated with electrochemical detection, requiring therefore repetitive recalibration to ensure reproducible quantification. [23] SERS and electrochemistry are both

sensitive and selective techniques that however suffer from an inability to provide reproducible quantitation. In this work, we are strategically combining these two techniques to perform a dual-modality measurement, so that they can work together to minimize their limitations. In addition to this integration we perform the measurements at multiple sites, where the diversity of the SERS substrate modulates both Raman intensity and electrochemical properties, allowing for more accurate calibration compared to a traditional single-site Raman measurement. This approach could be extremely useful for the low-cost fabrication of sensitive platforms for health/environmental monitoring, and bio-surveillance applications, with a high degree of device-to-device reproducibility. The order in which these techniques were performed within the experimental design was important: Electrochemical measurements were carried out prior to the SERS assay to gain the necessary surface area information. This approach eliminates the variation caused in the measurements during the assay, which could arise due to electrochemical activity of the analyte being tested. Randles-Sevcik and Cottrell equations were chosen for the area calculation. Our measurements revealed that coulometry is more sensitive to the surface changes in comparison to cyclic voltammetry. Furthermore, we observed that the maximum charge of the coulometric measurements has a strong correlation with the surface area on the electrode; hence, charge values were chosen for the analysis. This approach can be a useful aid in sensor design through reduction of data processing overhead associated with the sensing system as it involves extracting the peak value associated with coulometry curve. The concept of combining SERS with electrochemistry provided the dual modality element of the system.

A Dual Modality Multisite system was designed to increase precision in SERS quantification. The idea of a multisite system, brings a core principle used in communication systems, utilized to reduce the error through addition of diversity in the signal to be transmitted. The use of multiple simultaneous measurements and the introduction of diversity in measurement conditions is a well-established technique for maximizing signal to noise ratio and minimizing error rate in digital communications. [24] Here, this principle is applied to the induced diversity in Raman signal through substrate diversity. In this context, substrate diversity means variation in the surface area of the working

SPE electrodes. On keeping the other parameters, the same, the concentration or size of the nanoparticles used for working electrode functionalization introduced the variation in surface area. This diversity in turn modulated the Raman signal intensity in proportion to the surface area. Multi-site can be defined as multiple substrates bearing differences based on chosen parameters. For the present work we have chosen to work with four different concentrations of nanoparticles,this providing four different kinds of substrates in terms of surface area feature. These four substrates would comprise the multi-site feature of the system. The Raman peak intensity is thus normalized with respect to the substrate active surface area, which varies from device-to-device, allowing for a higher precision measurement.

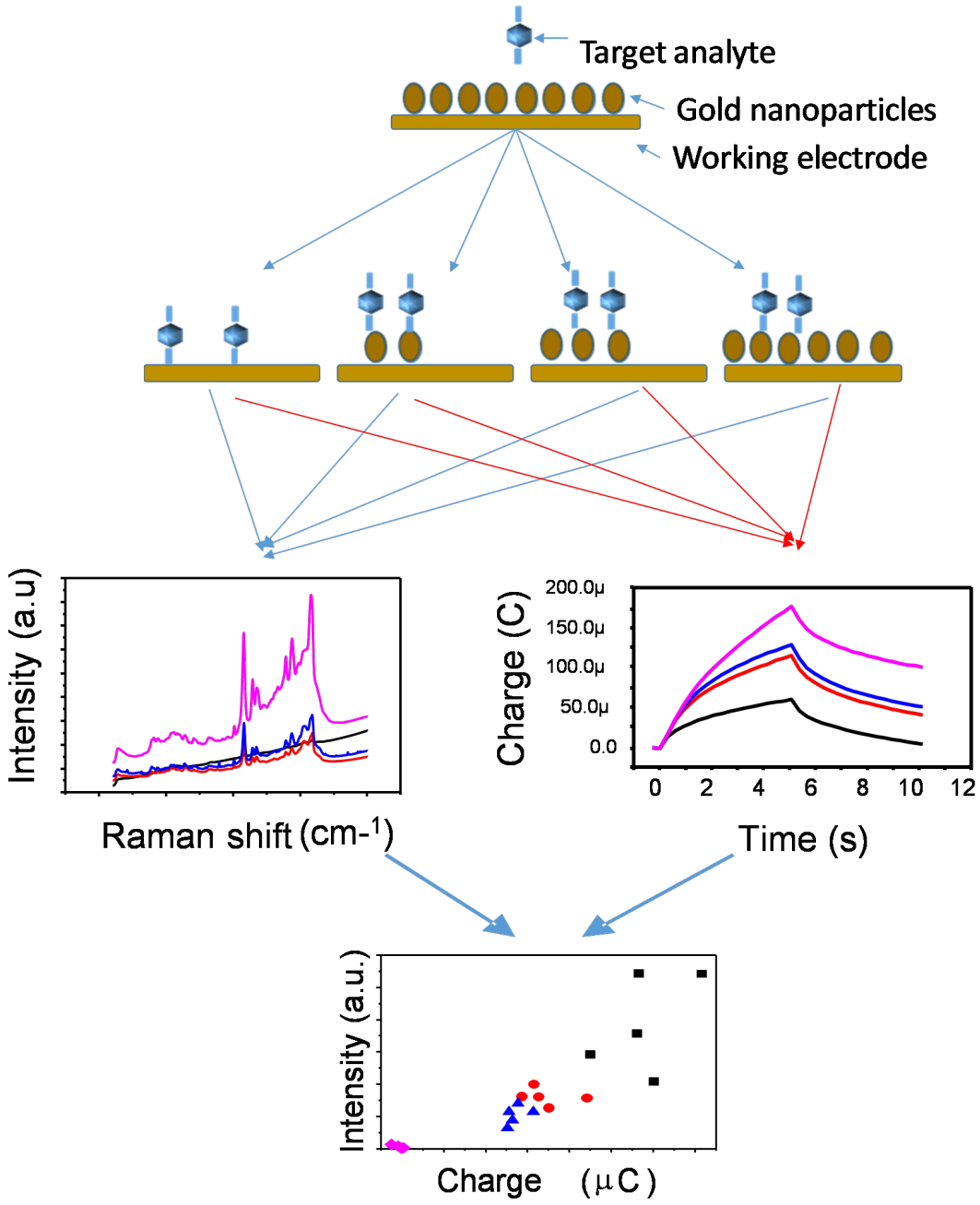

Figure 2.1: Dual Modality Multi-Site Sensing platform. The system comprises nanoparticles of different concentrations functionalized onto different working electrodes. This entails the multiple-site feature of the system. Dual modality is achieved by performing electrochemical measurements on the electrodes followed by Raman measurements on the electrodes incubated with an analyte. Combining dual modality with multi-site feature leads to emergence of positive correlation that can be utilized to improve analyte quantification.

2.2 Experimental Section

Materials and Instrumentation: Gold(III) chloride trihy-drate ($HAuCl_43H_2O$) and trisodium citrate dihydrate ($C_6H_5O_7Na2H_2O$) were purchased from Acros Organics. Cysteamine, potassium hexacyanoferrate(III) ($K_3Fe(CN)_6$), potassium hexacyanoferrate(II) trihydrate ($C_6FeK_4N_63HO$), and 4-aminothiophenol (4-ATP) were purchased from Sigma Al-drich. Ultrapure water (18.2 Mcm) was used for preparing the solutions. All glassware was aqua regia cleaned. The Raman spectra were obtained using a Renishaw InVia Raman microscope. A Gamry Reference 600 potentiostat was used for carrying out the electrochemical measurements. Dropsense DRP 220AT screen printed electrodes (SPEs) were purchased from Metrohm USA.

2.2.1 Nanosphere Synthesis

Gold stock solution (0.75 ml of a 0.025 M $HAuCl_43H_2O$ solution) was added to 149.25 ml of DI water. The solution was heated in an Erlenmeyer flask via a water bath. Once the temperature reached 98 C, 8.5 ml of 1% wt. aqueous solution of trisodium citrate dehydrate were added. The solution was allowed to boil for 35 minutes and then to cool to room temperature while stirring.

2.2.2 Preparation of SERS Substrates

SPE electrodes, having three electrodes, namely, working, reference and counter electrodes printed on the chip, were cleaned in 0.01 M $H_2SO_4$with cyclic voltammetry, sweeping the voltage between 0 and 1.2 V for 12 cycles at a scan rate of 100 mV/s. The number of cycles was chosen to be 12 as the voltammograms stabilized after 12 cycles.

2.2.3 Cysteamine Functionalization

10 l of 0.1 M cysteamine solution were drop casted on the working electrode (WE) and left in a humidified chamber. Thereafter, the SPEs were washed with water. Three different concentrations of nanospheres were chosen for immobilization on the working electrode of the SPEs. 10 l of any given nanosphere concentration were dropcasted on

the cysteamine-functionalized SPEs. These SPEs were then left in humidified chamber for functionalization. After incubation, the SPEs were washed twice with running water from a squeeze bottle, dried, and characterized using cyclic voltammetry (CV) and Coulometry.

2.2.4 Electrochemical Characterization

The electrodes were cycled in 9 ml of equimolar solution of$K_3Fe(CN)_6$ and $K4Fe(CN)6$ at 0.5 mM each in 50 mM KCl for two cycles. The voltage for cyclic voltammetry was swept from -0.2 V to 0.5 V at the scan rate of 20, 40, 60 ,80, and 100 mV/s with step size of 2 mV for each. Chronocoulometry was performed next. The two-step potential was from 800 mV to 0 mV for 5 seconds each. Thereafter, the EIS response was recorded for the frequency range of 0.1 to 1 MHz.

2.2.5 4-ATP Functionalization

After electrochemical characterization, the nanospheres deposited on the SPE were functional-ized with 4-ATP. Three different concentrations of 4-ATP were chosen for the functionalization. 4-ATP was prepared initially in 0.5 ml ethanol followed by dilution in DI water. 4-ATP was mixed with the equal amount of Clelands reagent to reduce any disulphide bonds. The solution was kept on a shaker for an hour and then was centrifuged at 10000 g for 5 minutes. The supernatant was removed and centrifuged again at the same speed and for the same time. 10 l of 4-ATP at any given concentration were then dropcasted on the nanoparticle-functionalized working electrode of the SPE. Incubation was carried out for 24 hours in a humidified chamber and then the SPEs were washed twice with DI water using the squeeze bottle. The SPEs were then dried.

2.2.6 Raman Characterization

Raman characterization of ATP-functionalized SPEs was carried out using 633 nm laser exci-tation, one accumulation, 10 s exposure, 50x objective, and 22W laser power with 1200 g/mm grating. An average of 1500 spectra at different points on a single SPE were taken to compare the Raman response of the different SPEs through maps. Control

substrates used for the experiment were SPEs with working electrodes functionalized with only 4-ATP or only nanospheres.

2.2.7 Capping nanostars with CTAB

In order to cap the nanostars with CTAB, 330 l of 0.2 M CTAB were added to 4 ml of gold nanostars synthesized using the protocol.

2.2.8 Preparation of Substrates for Studying the Effects of Electrochemical Measurements

Substrates were prepared by depositing a 2 nm layer of chromium followed by 100 nm gold on glass slides. The substrates were cut in 1cm x 0.5 cm size and incubated in 0.1 M cysteamine for four hours. The substrates were washed with water. Thereafter, they were incubated in the 500 l of nanospheres, surfactant free nanostars, CTAB-capped nanostars and Triton-x capped nanostar. SEM characterization was carried out for each of the substrates followed by electrochemical measurements and then SEM characterization again.

2.2.9 Electrochemical Characterization

The electrodes were cycled in 2 l of equimolar solution of $K_3Fe(CN)_6$ and $K_4Fe(CN)_6$ at 0.5 mM each in 50 mM KCl, dropcasted on the electrodes for two cycles. The voltage for cyclic voltammetry was swept from -0.2 V to 0.5 V at the scan rate of 20, 40, 60 ,80, and 100 mV/s with step size of 2 mV for each. Chronocoulometry was performed next. The two-step potential was from 800 mV to 0 mV for 5 seconds each. Thereafter, the EIS response was recorded for the frequency range of 0.1 to 1 MHz.

2.3 Results and Discussion

In this study, we used dual modality sensing with Raman spectroscopy and electrochemistry. Figure 2.1 shows the schematic of the working principle of the sensor. In our assay, diversity was introduced at each site to provide Raman signal modulation

capability to encode the signal in different amplitudes. The result of the dual-modality multi-site measurement for each analyte concentration is a two-dimensional array of data points that can be mapped to a line using linear regression. This data manipulation approach results in the decrease of mean-squared error variation compared to a standard Raman bioassay, where repeated measurements are performed on a single substrate in a single dimension. The sequence of steps followed to develop the system is described in the next sections.

2.3.1 Electrochemical Modality Design and Characterization

The electrochemical modality was designed for measurement of diversity induced on the SPEs by the addition of nanoparticles. The major steps in engineering the electrochemical modality were the functionalization of the working electrodes surface with a tether molecule, cysteamine, followed by nanoparticle immobilization via the thiol group. In order to modulate the surface area in this modality, we varied the concentration of the nanoparticles being functionalized. The variation in the surface area produced because of these processes were studied using electrochemical techniques of Cyclic Voltammetry and Chronocoulometry. In addition to these, imaging tools were used for studying the surface features of the working electrodes and the shape and size of the nanoparticles used. The working electrodes on the SPEs were characterized using scanning electron microscopy (SEM) (Figure 2.2 a). The synthesized nanospheres were characterized using TEM and UV-Vis spectrophotometry. Figure 2.2 b shows the TEM micrograph of the nanospheres used for the study. The average diameter was measured to be around 30 nm with a standard deviation of 5 nm, as shown in the distribution reported in Figure2.2 c. The nanospheres were further characterized with UV-Vis spectroscopy. Figure 2.2 d shows the UV-Vis data with the localized surface plasmon resonance (LSPR) peak around 522 nm.

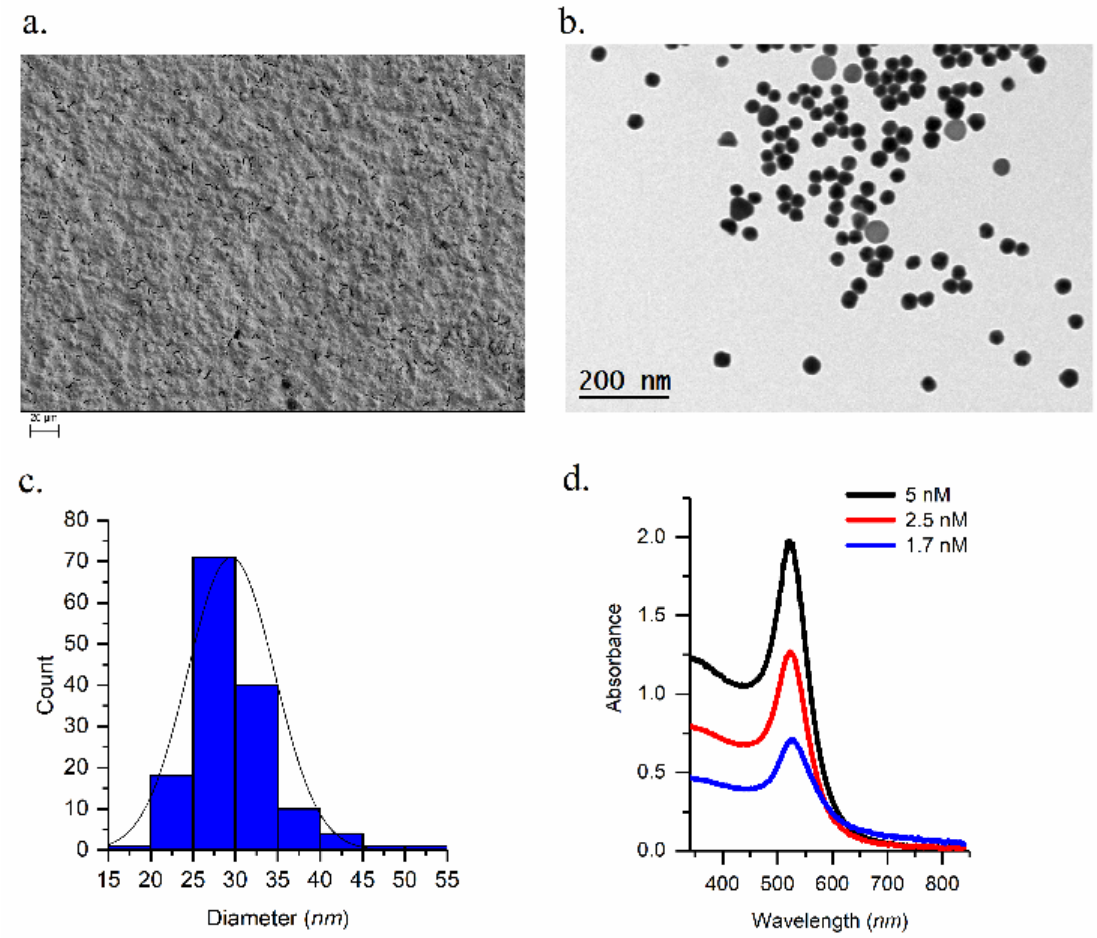

Figure 2.2: Characterization of SPEs and the nanoparticles used for developing the system. a) SEM of the working electrode. b) A TEM micrograph of the nanospheres used for functionalization. c) Distribution of nanoparticle diameters with average diameter of 30 5 nm. d) UV-vis spectra of different nanoparticle concentrations used for working electrode functionalization

. Three different concentrations of nanoparticles, 5.2 nM, 2.5 nM, and 1.7 nM, were used in the study. The concentration of the particles was calculated using the following equations. [25]

$$ln(\epsilon) = \kappa ln(D) + a \tag{2.2}$$

where is the extinction coefficient in M-1 cm^{-1}, D is the diameter of the nanoparticles, and the coefficients k and a are 3.3211 and 10.80505, respectively. The values of k and a were obtained from Liu et al. [25] Subsequently, the Beer-Lambert law was used for

the calculation of the concentration.

$$A = \epsilon bC \tag{2.3}$$

Where, A is the absorbance, b is the path length, and C is the concentration.The path length for the UV-Vis spectrophotometer used was 1 mm. The chronocoulometric response of the substrates was examined with $K_3Fe(CN)_6$ /$K_4Fe(CN)_6$ as the electrochemical probe. Coulometric measurements were performed for plain SPEs, after cysteamine functionalization, and then after nanoparticle functionalization. The maximum charge for the curves and the slopes increased after each functionalization step. Figure 2.3a shows this increment.

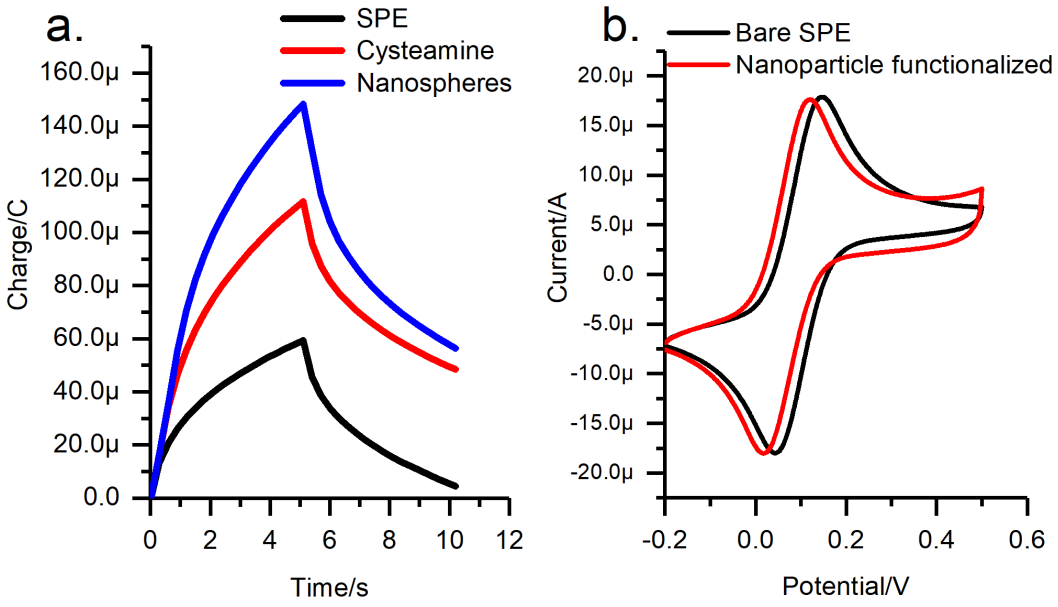

Figure 2.3: a)Coulometric characterization of working electrodes carried out for the bare electrode, electrodes functionalized with cysteamine, and electrodes functionalized with cysteamine and nanoparticles. b) Cyclic voltammetry characterization of working electrodes carried out for the bare electrode and for an electrode functionalized with nanoparticles.

The voltammetric response of the substrates was also examined with the redox couple $K_3Fe(CN)_6$ /$K_4Fe(CN)_6$ as the electrochemical probe. Well-defined reduction

and oxidation peaks were observed: The peaks were symmetric and had similar oxidation and reduction peak current values. On plot-ting the peak current vs the square root of the scan rates, a linear increase was observed. More information on this analysis is available in the supplementary information at the end of the chapter. Cyclic voltammograms for the SPE reveals that the ferri-ferrocyanide redox system that we are using is quasi-reversible as the difference in peak potential, ΔE_p , is > 59 mV. The quasi-reversible nature observed could be explained by the findings on the kinetics of ferri/ferro cyanide redox system, which has been shown to be influenced by the surface functionalities on the electrodes. [26]

E1/2 app, the half-wave potential of the system, can shift based on the surface charge of the electrode. A negative shift in the E1/2 app was observed after nanoparticle functionalization, which could be attributed to increase in surface negative charge due to the presence of citrate. [27, 28] Figure 2.3 b shows these variations after the nanoparticle functionalization. Apart from these characterization results, we also found that the coulometric response had a positive correlation with the concentration of nanoparticles functionalized on the substrates. Therefore, coulometry was chosen as the electrochemical modality to be incorporated with the data from the Raman sensing modality. The next section discusses the Ra-man sensing modality in more detail.

2.3.2 Raman Sensing Modality Design and Characterization

As mentioned earlier, the second modality chosen for the system was Raman spectroscopy. The Raman modality design shared the same platform as the electrochemical modality (nanoparticles functionalized on SPE) and could thus provide not only a correlation feature but also a way to circumvent the issue of calculating EFs for each substrate. In order to test the system, we chose 4-Aminothiophenol (4-ATP) as the target analyte. Apart from its significance in molecular electronics, 4-ATP is a well-studied probe molecule in SERS given its strong chemical interaction with noble metal surfaces, which results in strong signal enhancements with metals like gold and silver, and its large Raman cross section. [29] 4-ATP, despite having a simple molecular structure, exhibits a complex Raman-active vibrational fingerprint. Since the fundamental

SERS fingerprinting region for 4-ATP in SERS lies in the wavenumber range below 1650 cm^{-1}, we chose the range of 100 cm^{-1} to 2000 cm -1 for further analysis. [30] Table 2.1 1 shows the Raman vibrational assignments for the major peaks. The binding interaction be-tween 4-ATP and gold nanoparticles can result in vibrational frequency shifts due to changes of the electronic structures and the vibrational coupling. [30] The major peaks in the spectra for 4-ATP on the substrate were located around 1078, 1144, 1173, 1278, 1304, 1353, 1391, 1435, 1490, 1528, 1576, 1588, and 1642 cm^{-1}. More information on the spectral analysis of 4-ATP is provided in the supplementary information.

Figure 2.4 shows the Raman spectra for 4-ATP on the SPE functionalized with gold nanospheres (black curve). In addition to this, it reports three control spectra for SPEs with 4-ATP without nanoparticles, SPE with nanoparticles and no 4-ATP, and SPEs with nanoparticles and Clelands reagent without 4-ATP. Clelands reagent is used to cleave any disulphide bond that might form between two 4-ATP molecules, thus producing thiol groups amenable to interact with gold nanoparticles.

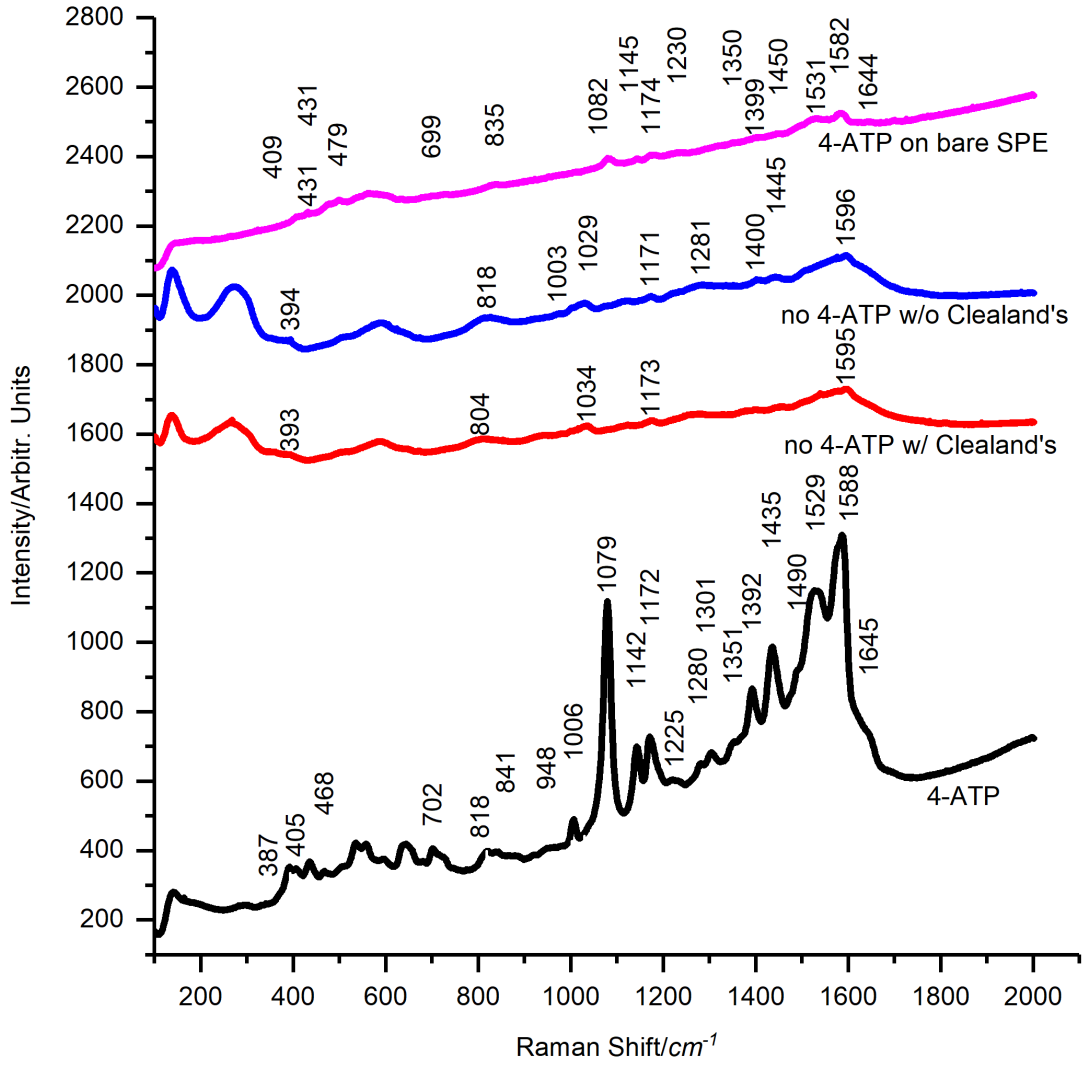

Figure 2.4: Raman spectrum for 4-ATP, the analyte used for testing the system, and the various controls. Analysis of spectra leads to using the 1079 cm^{-1} peak for demonstrating the concept of dual modality multi-site system. The purple spectrum is for a control experiment where the working electrode was incubated with 4-ATP without any nanoparticles. The blue spectrum is for the working electrode functionalized with nanoparticles. The red spectrum is for the control experiment where the working electrode functionalized with the nanoparticles was incubated with Clealands reagent without any 4-ATP. The black spectrum is for the electrode functionalized with nanoparticles and 4-ATP following the described protocol.

4-ATP on SPE with nanosphers	Nanospheres on SPE	Clealand's Reagent	4-ATP on SPE	Peak assignment
	266	274		δCN+δCS
392	390	392		τCC
407			406	τCC
468			478	γCCC
701				πCH+πCS+πCC
818	810	820		νCH+νCS+yCC+πCH
841			833	πCH
	941			πCH
1007	1002	1034		γCC+γCCC
1078			1082	νCS+νCC
	1121			δCH
1144			1146	δCH
1172	1174	1174	1173	δCH+νCN
1279		1283		νCH
1303				νCC+δCH
	1379			νCC+δCH
1392	1399	1403	1403	νCC+δCH+νNN+δCN
1435	1446	1444	1445	νNN+δCH
1490				νCC+δCH
1588	1599	1599	1584	δNH

Table 2.1: Raman Peak assignment for the substrates

a) ν-stretching, δ and γ- bending, π-wagging, τ-torsinal [31, 32]

It can be seen from Figure 2.4 that the characteristic Raman peaks for 4-ATP are much less intense than the SERS peaks collected in the presence of nanoparticles (purple curve). Spectra from the substrates having Clelands reagent on the nanoparticles reveal that there is not any significant contribution from this reagent to the peaks observed for 4-ATP (red curve). SERS spectra without 4-ATP or Clelands reagent shows only the contribution from the functionalized nanoparticles (blue curve). Based on the comparison between various curves in Figure 2.4 and the rationale derived from the literature, [31, 32] the peak around 1079 cm^{-1} was chosen for further analysis for the system.

As can be observed in the spectrum, there are high levels of background signal around 1500 cm^{-1} which could be indicative of amorphous carbon generation. Amorphous carbon can be generated as a result of damage to the substrate from high power laser excitation. We carried out a study to determine the appropriate laser power for the

measurements. Figure 2.5a shows the Raman spectra at various laser excitation powers. In this case, high background was observed even for a laser power as low as 22μW (figure 2.5 b), probably due to the in-tense electric field enhancement at the surface of nanoparticles. One drawback of using such low laser power was that the peak intensity also decreases drastically, thus impacting the sensitivity of the assay. Overall, we found 53 W laser power to be a good compromise to achieve low background and sufficient signal intensity, in comparison to the other values.

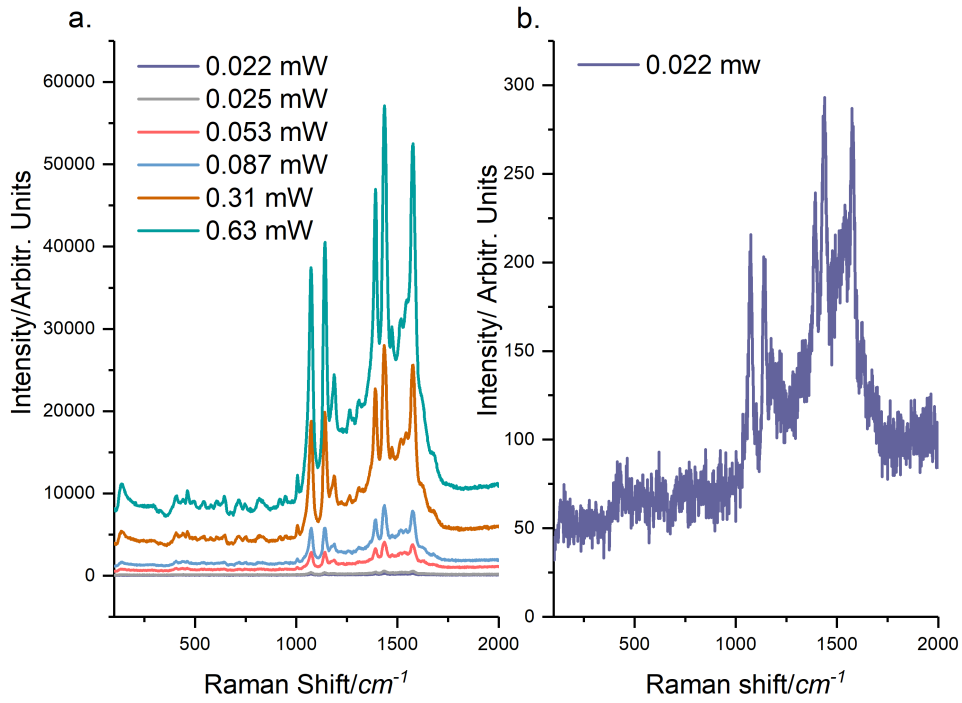

Figure 2.5: Power variation study to select the appropriate power level for carrying out Raman measurements. a) show the Raman spectra for 4-ATP at different laser powers. b) shows that the comparatively high background was still being observed for the low power, as low as 22 μW, indicating that the background could not be eliminated by laser power reduction without compromising the signal intensity. Laser power of 53 μW was therefore chosen as the best com-promised between background and signal intensity for the Raman mapping.

2.3.3 Induction of Diversity for Multi-Site by Varying Nanoparticle Concentration and Size

Diversity in the Raman and electrochemical measurements can be induced by parameters that would modify the surface area. We chose to test two such parameters, namely, size and concentration of nanoparticles. We functionalized the substrates with two different concentrations (5 nM and 2.5 nM) and two sizes (15 nm and 30 nm) of nanoparticles for a given concentration of 4-ATP. Figure 2.6 shows the modulation capability because of different sizes and concentrations of particles. These results show that it is feasible to modulate the Raman and electrochemical measurements through variation of nanoparticle size or concentration. After discovering this modulation capability, we decided to apply it for increasing the precision of the SERS quantification. In this study, we chose to use nanoparticle concentration to induce diversity.

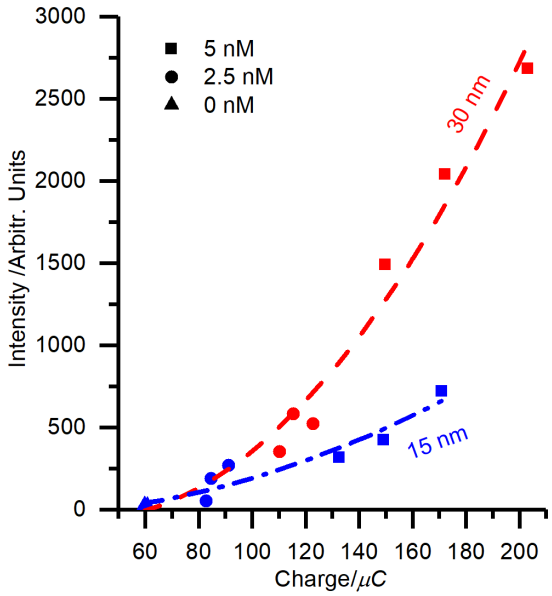

Figure 2.6: The blue and red curve show the modulation of the Raman intensity at 1079 cm^{-1} with increasing substrate charge using different nanoparticle concentrations for 30 and 15 nm nanospheres. This modulation capability was one of the major contributors in engineering the multi-site measurement capability for the system. In addition to the nanoparticle concentration, the Raman and coulometric measurements can be modulated using the different sized nanoparticles.

2.3.4 Application of Dual-Modality Multi-Site Sensing for Improved Precision for SERS Quantification

We set out to use this system for improving the precision of SERS quantification. As mentioned earlier, induction of diversity is a well-established technique in communication systems to minimize error-rates in data transmission. In Raman measurements, we applied a similar principle. We designed our experimental setup analogous to a communication system. Concentration of 4-ATP was the source of information, transduced through laser excitation and then modulated and encoded through the nanoparticles. The transmitted signal from the nanoparticle-functionalized substrates travels to the receiver, Raman microscope, through the aerial medium. In addition to this, a multiple input single output (MISO) scheme was applied to the data being transmitted- same data were transmitted by 4 different transmitters and received by the Raman microscope. Although we use only a single excitation laser and a single Raman detector at a time, we are mimicking a MISO communication system because we are carrying out multiple measurements. For this particular system, it is irrelevant whether the measurements are done in parallel (like a typical wireless communication system) or serially (like our system) since our measurement does not require the high data rates necessary for a communication system.

In our analysis of the Raman spectra of 4-ATP in various conditions including controls, we found that the peak around 1079 cm^{-1} can be a good candidate for an information source to be used for further analysis of the system. The spectrum collected through the Raman microscope was used for further processing. The mean baseline subtracted peak value for the 1079 cm^{-1} peak was extracted from the 1500 data points collected on each substrate through Raman maps.

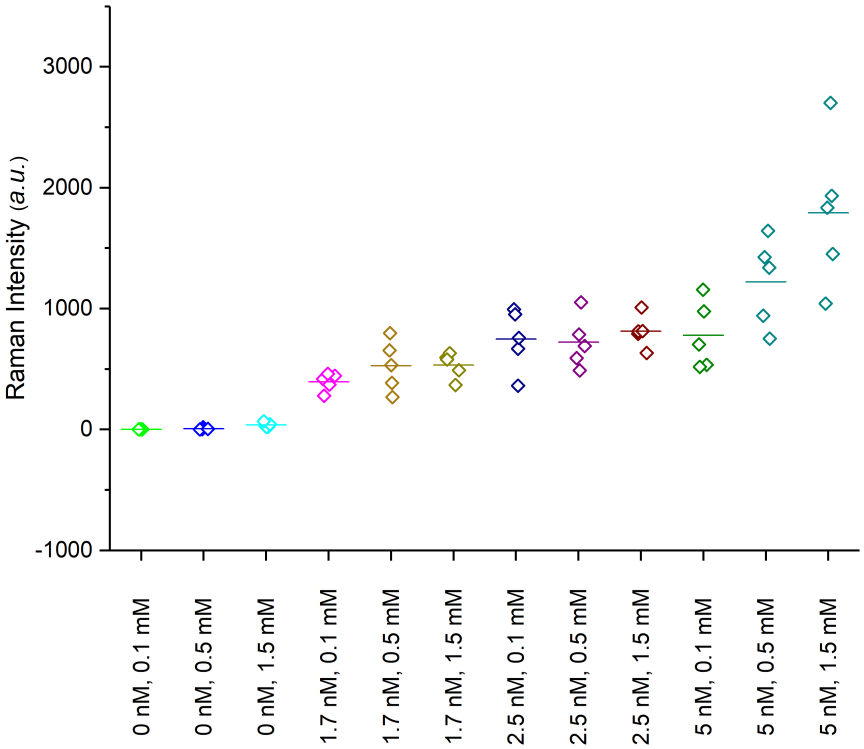

Figure 2.7: Mean baseline subtracted Raman Intensity of the 1079 cm^{-1} peak for different nanoparticle and 4-ATP concentrations for single site measurements. The intensity values have low deviation for lower nanoparticle concentrations, at the cost however of reduced peak intensity. For higher nanoparticle concentrations, the signal intensity improves at the cost of standard deviation. This trade-off inspired us to come up with a technique to off-set these drawbacks.

Figure 7, shows the distribution of the mean baseline-subtracted Raman intensity for all the different concentrations of nanoparticles and 4-ATP. It can be deduced from Figure 8, that these measurements allow us to find a range of expected Raman intensity for a given nanoparticle and 4-ATP concentration. Even though the intensity variation is very low for lower concentrations of nanoparticles, which provides higher precision, it comes at the cost of reduced sensitivity. Figure 2.8 summarizes the trade-off between the sensitivity and precision. In an ideal scenario, we would always obtain a very narrow intensity distribution at identical surface functionalization. Even though we

were not able to achieve this ideal result, we were able to observe a positive correlation be-tween the peak charge measured electrochemically for the substrate and the Raman signal intensity. Therefore, even if the variations in functionalization were induced by uncontrollable parameters, the measured charge provided a correction factor for intensity normalization at each given concentration. Baseline-subtracted mean Raman intensity data were plotted against the peak charge value measured using coulometry.

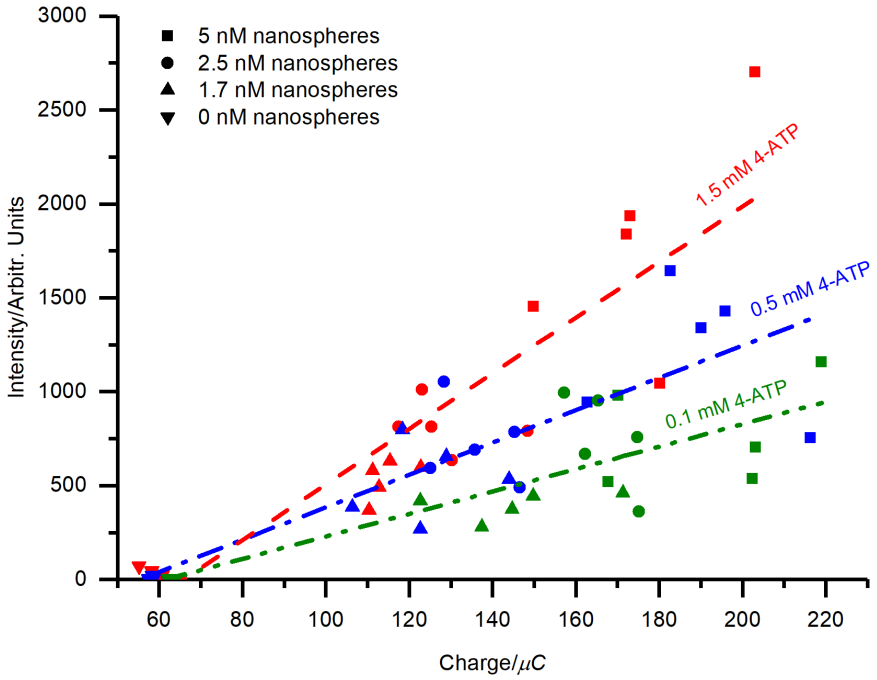

Figure 2.8: Variation of the mean baseline-subtracted intensity of the 1079 cm^{-1} Raman peak plotted against the coulometric charge measured for multi-site measurements. Linear trends emerge with introduction of multi-site measurements with decreasing slopes for lower analyte concentration.

Figure 2.8 shows the trends observed for such a dual modality multi-site sensing system. Linear regression analysis was carried out for the system and the dotted lines represent the curve fit for different 4-ATP concentrations. In analogy to a communication system, these linear regression curves can represent the information being received at the receiver and could be further processed for deduction of the information that

was transmitted.

In addition to the correction capability provided by the dual-modality multi-site approach, an additional improvement that we observed was that by carrying out measurements on substrates with different nanoparticle concentrations, we observed a tighter root mean squared error variation as can be seen in Figure 2.9. It shows the root mean squared errors of the fits calculated for the different combination of nanoparticle concentrations used for the multi-site set up. The root mean squared error (RMSE) variation has higher spread for the single site. When we used two sites, there was reduction in the RMSE even for the worst (the highest error) combination in comparison to the single site. As we increased the number of sites, we observed a progressive decrease in this spread with the increase in the number of sites. Similar trends were observed for different 4-ATP concentrations. This reduction in RMSE provides proof for improvement in predictability of measurements with increase in measurement diversity.

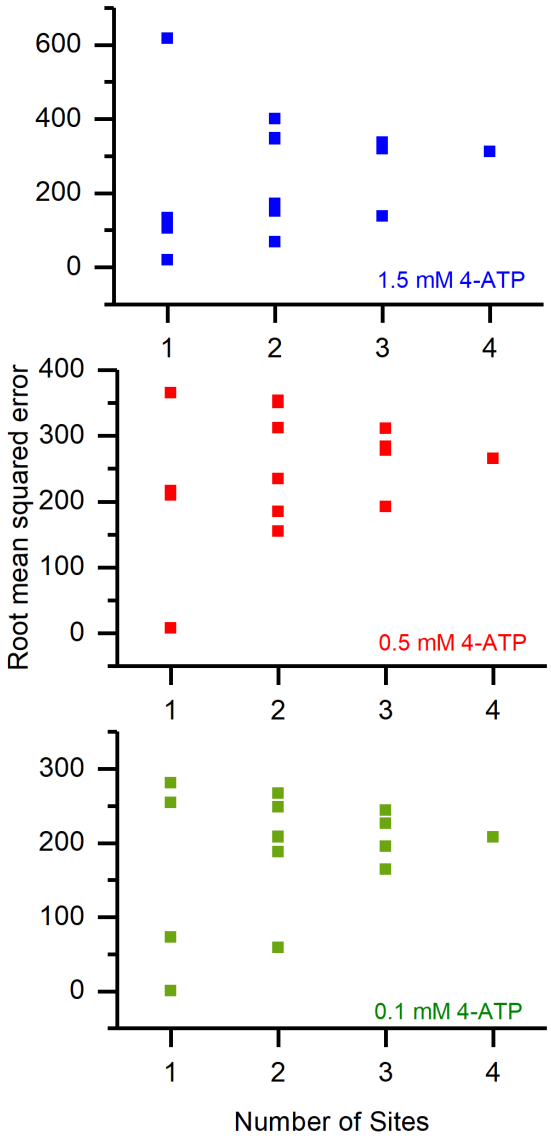

Figure 2.9: The variation in the root mean squared error decreased with the number of simultaneous measurements. The standard error in the root mean squared errors decreased by at least 2.8-fold from single site to 3-site measurements.

2.3.4.1 Studies to Improve Dual-Modality Multi-Site

Effects of electrochemical measurements on the functionalization of different kinds of nanoparticles on the substrates was studied. Figure 2.10, 2.11,2.12,2.13 shows the SEM of the substrates before and after the electrochemical measurements. On comparing the SEM images, it was found that electrochemical measurement affected the morphology of the gold nanostars. Thus, it was decided to use electrochemical modifications after the Raman measurements are already performed.

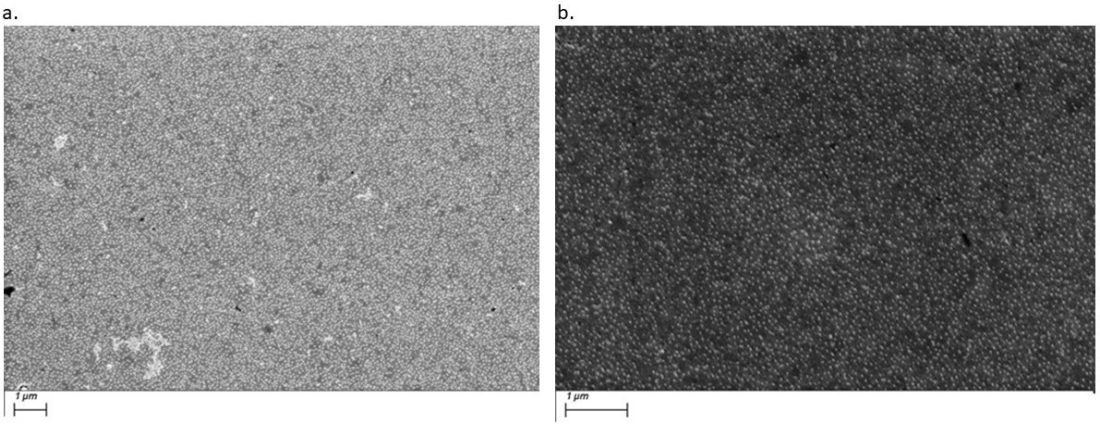

Figure 2.10: a. SEM image of nanospheres functionalized on the glass slides coated with gold film. b. SEM of the substrates after running the electrochemical measurements

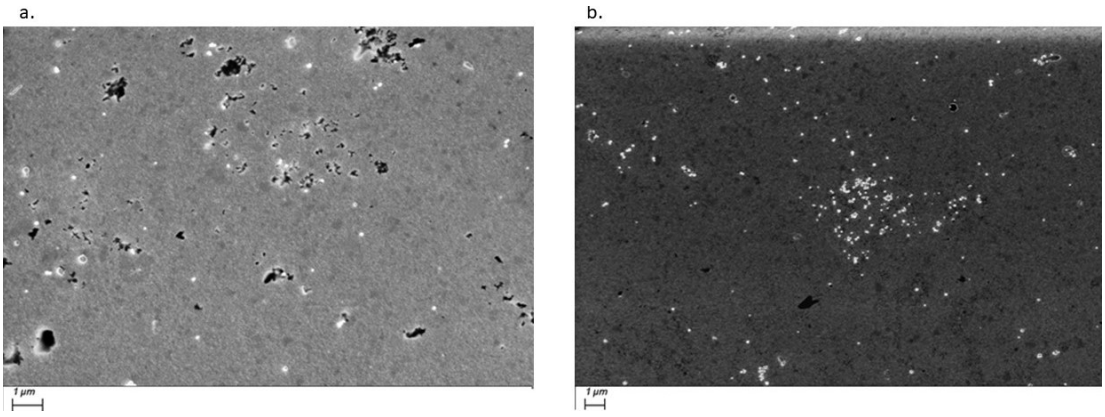

Figure 2.11: a. SEM image of CTAB coated gold nanostars functionalized on the glass slides coated with gold film. b. SEM of the substrates after running the electrochemical measurements

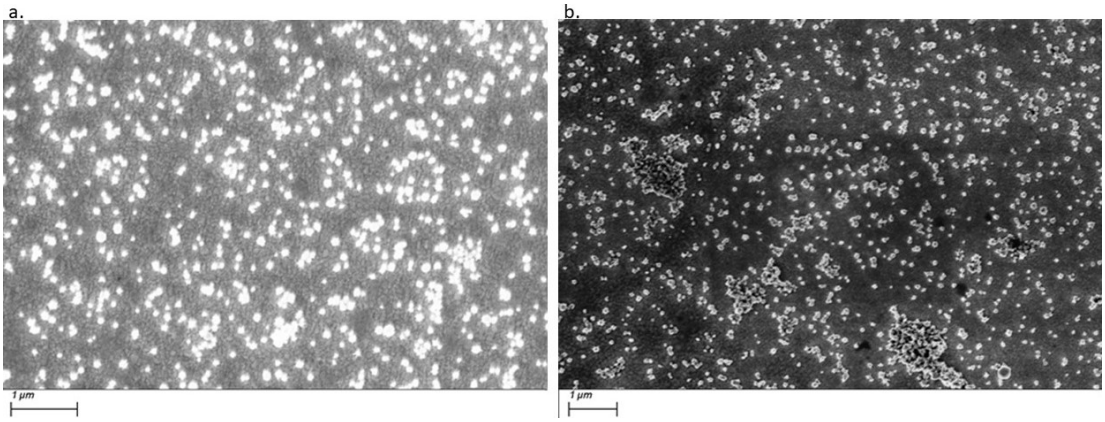

Figure 2.12: a. SEM image of surfactant free gold nanostars functionalized on the glass slides coated with gold film . b. SEM of the substrates after running the electrochemical measurements

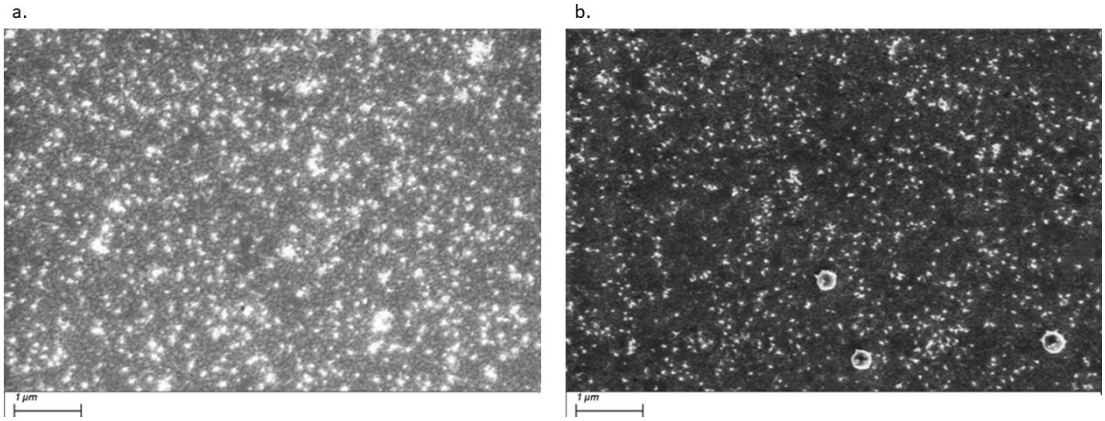

Figure 2.13: a. SEM image of TritonX coated gold nanostars functionalized on the glass slides coated with gold. b. SEM of the substrates after running the electrochemical measurements

2.3.5 Conclusion

In conclusion, we introduced a novel substrate-independent technique to improve the precision of SERS quantification through a multi-site dual-modality sensing system. The over-all reduction in the root mean squared error allows for better predictability in the determination of analyte concentration and has the potential to be used for quantification of important biomarkers, especially in point-of-care, low-cost as-says.

Devices or techniques with fast response and low cost are required for rapid and accurate diagnosis. Further improved versions of our approach could represent solutions for such requirements. Another important finding of this study is that this system is analogous to existing communications systems. We showed that the Raman signal can be modulated in intensity by varying nanoparticle concentration and size. These findings can provide foundations for fundamental research in development of novel communications schemes at the molecular or nanoscale regimes, which could be a major step in enabling molecular communication systems. [33]

In addition, this study provides means and motivation to explore some fundamental questions related to the determination of the Raman-active surface area of a SERS substrate using electrochemical techniques.

Based on the improvement studies, we concluded that electrochemical measurements should better be performed after the Raman measurement for certain kinds of nanoparticles used. the future work would include using this system for detection of analyte of interest.

2.3.6 Supplementary Information

2.3.6.1 4-ATP Raman

4-ATP Raman Spectra In the Raman spectra of 4-ARP 27 in-plane and 12 out-of-plane vibrations are present. [34] Wu et al. classified the vibrational modes into three wavenumber regions. (a) Seven high frequency fundamentals within the range of 2000-3500 cm^{-1}. (b) Thirteen fundamentals in the range of 1000-1650 cm^{-1} ,fundamentals of high interest in SERS spectra.(c) Nineteen in the wavenumber region lower than 1000 cm^{-1}. The peak around 917 cm^{-1} on the spectrum was assigned to the bending vibrations of the SH bond. The absence of this peak indicates that the 4-ATP is bound to the working electrode via a Au-S bond. [35] The peaks around 1078 and 1588 cm -1 correspond to the CS and CC stretching for the a1 mode. [34, 36–43] The CS stretching mode around 1078 cm^{-1} is believed to be enhanced mainly by the

EM mechanism. [36, 43] There are several reports of 4-ATP transformation into 4,4-dimercaptoazobenzene (DMAB) during the spectroscopic measurements. [43–45] Peaks near 1500, 1460 and 1407 cm^{-1} and a doublet near 1150 cm^{-1} are attributed to the azodibenzoate. [43, 44] Huang et al. have demonstrated that the b2 mode band originates from 4,4-dimercaptoazobenzne (DMAB) which is produced during the SERS measurements. However, the functional group in the *para* position of benzenethiol has only a negligible influence on the binding interaction of benzenethiol with the metal surface, as the metalsulfur bond is electronically decoupled from the benzene ring, therefore, one should not expect a dependence on the bonding interaction for different derivatives on different surfaces of identical composition. [43] Also, DMAB can give peaks at similar positions to those of a1 modes of 4-ATP (1075 and 1594 cm^{-1}) with comparable signal intensity but with a slight shift in frequency. [45] Based on these factors, it seems like a good approximation that the number of molecules bound to the surface can be correlated with the peak intensity around 1077 cm^{-1} wavenumber. Raman maps of 1500 points were taken on each sample and then the peak intensity at 1077 cm^{-1} was used for further processing. Figure2.14 shows the spectra from one of the sample sets used in the analysis.

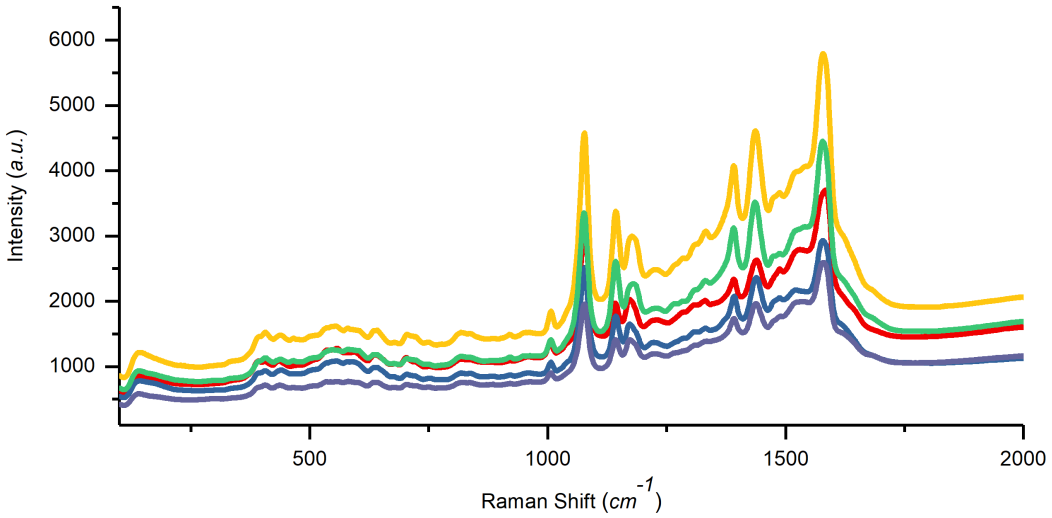

Figure 2.14: Mean Raman spectra for 1500 different points taken on five different samples functionalized using 5 nM nanosphere concentration.

2.3.6.2 Correlation Between the Electrochemical Measurement and Concentration of Nanoparticles

Charge measured for the SPE was used to calculate the mean values of the charge associated with a given concentration of nanoparticles. We found that there is a positive correlation between the concentration of nanoparticles used for functionalizing the substrates and the charge measured using the electrochemical measurements. The objective of changing nanoparticle concentration was to modulate the surface area. This in turn would modulate the electrochemical measurement and hence, charge measured during the electrochemical measurements would give information about the available surface area indirectly. Thus, as the nanoparticle concentration increases, surface area also increases. Increased surface area leads to increased charge measurement for electrochemical measurements. This could be seen in figure 2.15.

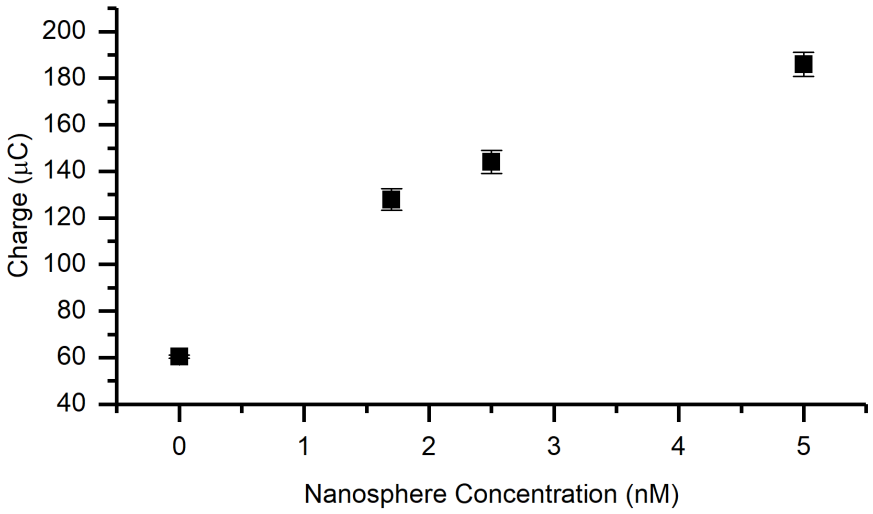

Figure 2.15: The graph shows the variation of charge measured with the concentration of nanoparticles used for making the substrates. The plot gives information on how modulation of nanosphere concentration could enable modulation of charge measurements.

2.3.6.3 Calibration Curve for Dual-Modality Multi-Site

Multi-site measurements provide the correction factor. When these measurements for a given concentration of analyte are used in the regression analysis, we can obtain a slope associated with each concentration. The curves provided above show the relationship between the slope of the regression line and the concentration of analyte. Therefore, when estimating the concentration of an analyte, one would first carry out the multi-site measurement, then find the slope of the regression line, and finally use the calibration curve as above to determine the analyte concentration. Figure 2.16 shows the calibration curve for the 4-ATP concentration.

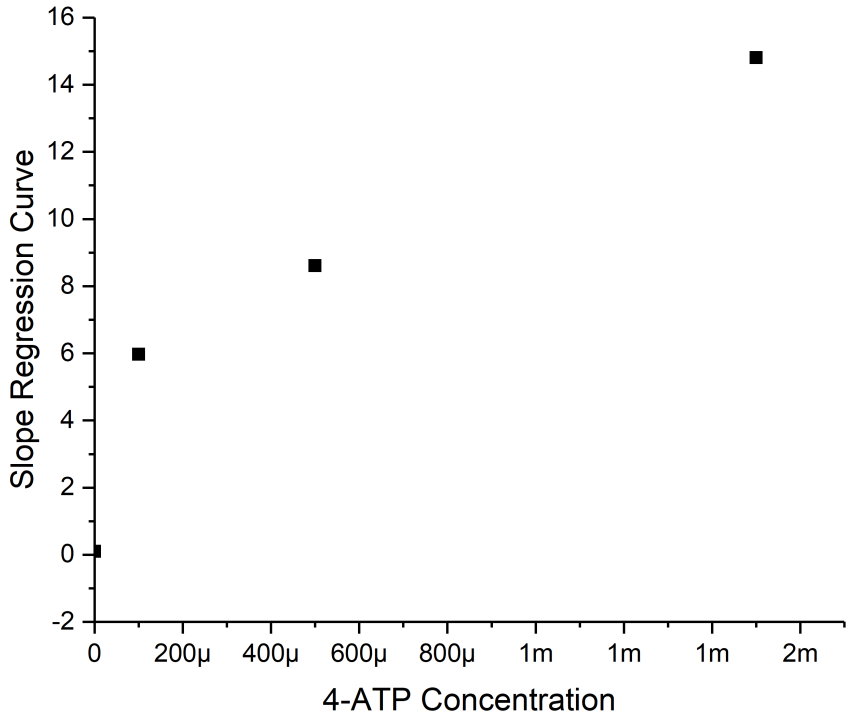

Figure 2.16: Calibration curve for a dual-modality multi-site sensing scheme .

2.3.6.4 Comparing 633 nm and 514 Laser for the Substrate Response

In order to carry out the Raman measurements 633 nm laser was chosen. Although the absorption peak of the gold nano-spheres is around 520 nm, we chose the 633 nm laser

excitation based on the preliminary results collected in our initial feasibility study. We found that the Raman response was significantly stronger when using the 633 nm laser compared to the 514 nm laser that we used for our substrate measurements.Figure 2.17 shows the response on the substrate for 4-ATP using 514 and 633 nm laser.

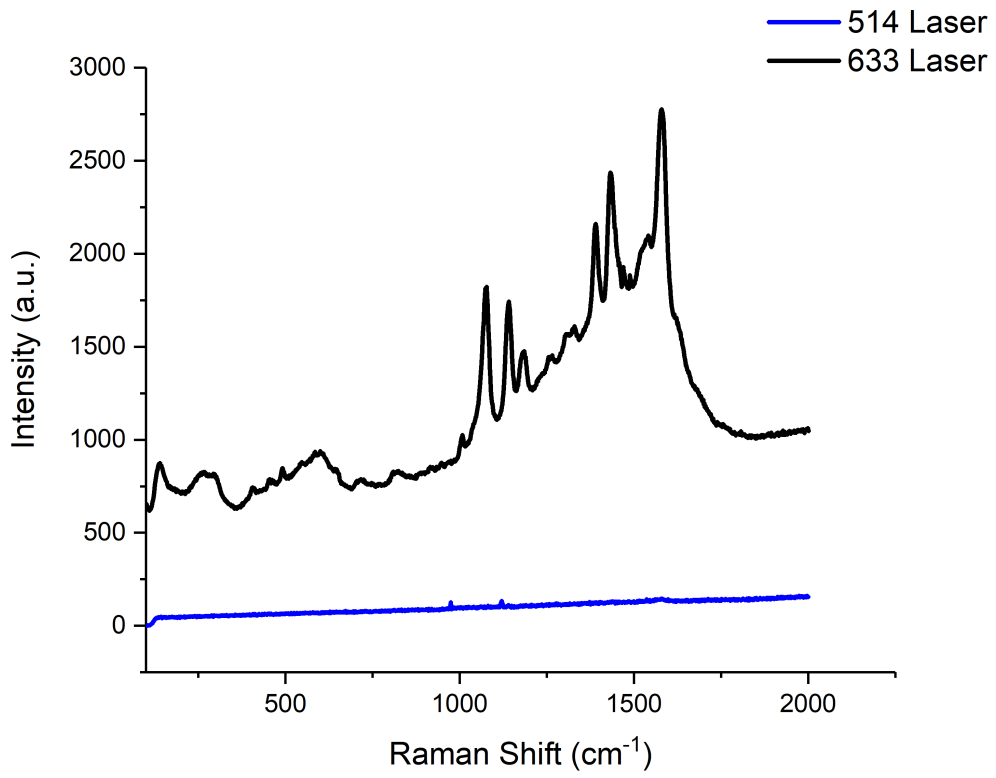

Figure 2.17: Comparison of response of substrate to 633 and 514 nm lasers.

Note: Reprinted (adapted) with permission from Sakshi Sardar, Laura Fabris, and Mehdi Javanmard. Improved precision in surface-enhanced raman scattering quantification of analyte through dual-modality multi-site sensing.Analytical Chemistry, 91(7):43234330, 2019. PMID: 30561991. Copyright (2019) American Chemical Society. [46]

Chapter 3

Development of Sensor for Phenylalanine

3.1 Introduction

Phenylketonuria (PKU) is an autosomal recessive inborn error of the phenylalanine metabolism. [14, 47] This disease is usually characterized by mutations in the phenylalanine hydroxylase (PAH) gene. PAH along with cofactor tetra hydrobiopterin (BH4) is essential for converting phenylalanine into tyrosine . The deficiency in this hepatic-based enzyme (PAH) leads to increase in the blood concentration levels of phenylalanine. There are several mechanisms through which the high levels of blood phenylalanine levels can have harmful effects on the brain development and function. One of the mechanisms, proposes that the high blood concentration of phenylalanine (Phe) eventually allows the molecule to cross the blood brain barrier leading an excessive accumulation in the brain and decrease in the concentration of other large neutral amino acids. [11, 47] L-amino acid transporter 1 (LAT1), which mediates the entry of large amino acids into the brain, can subsequently inhibit entry of other large amino acid in presence of high Phe concentrations. Large amino acids include tyrosin and tryptophan. These are precursors for dopamine and norepinephrine, and serotonin, respectively. Their deficiency can lead to neurotransmitter dysfunction or issues with protein synthesis. [13] There are couple of more mechanisms reported by Blau et al. that can be harmful for brain functions. As a result of complications arising from the high concentration of Phe, PKU can cause intellectual disability, microcephaly, sever mental retardation, motor deficits, eczematous rash, autism, difficulty swallowing, seizures/convulsions, developmental problems, aberrant behavior, dystonias, dyskinesias, hyperreflexia, or spasticity, and psychiatric symptoms. [11–13]

For diagnosis, newborns are screened for Phe levels in blood. Phe is a primary

marker for PKU and requires robust measurements for directing treatments. Common methods for detection of phenylalanine include, high performance chromatography, amino acid analyzers and tandem mass spectrometry. [13,47] According to Wegber et al. as per European guidelines on PKU the treatment should start as early possible to minimize its impact on the well-being in later years of patients. Studies have shown that every 4 weeks delay can decrease the IQ by 4 points. In addition, the treatment must be continued for life for best results. Stopping the treatment during childhood or pre-adolescence could be harmful. [14] PKU management mainly involves dietary restrictions on the amount of Phe being ingested. [13]. In addition, frequent Phe sampling is required to ensure that the levels are within the acceptable range. The frequency of sampling depends upon the age group of the patient. It is recommended for children of less than one year of age to undergo weekly testing; kids between the age of 1 and 12 should undergo fortnightly testing, adolescents and adults should undergo monthly testing, and pregnant women should undergo twice a week testing for blood Phe levels. [14, 14]

Based on these issues, there is a need for rapid detection of Phe levels in new born and older patients. Motivated by the relevance of this disease, and the limited available methods for Phe Testing, we wanted to develop a sensor that could provide rapid detection of Phe, possibly in urine for minimal invasiveness for the patients. In order to develop the sensing system, we decided to manufacture the sensing substrates as gold thin film-coated glass slides. For sensing we chose SWCNT and Nanostars for creating the nano-scale surface features, as both have been shown to be effective SERS enhancing materials.

Carbon nanotubes are 1D nanostructures that have unique physiochemical properties. [48] They also have high mechanical and chemical stability. [49–51] In addition to this, they have superior thermal and electrical properties [50–52](2,3,7). As a result, they can find application in numerous areas ranging from additives for polymers and catalysts, transistors , microelectronic devices composite materials, high frequency nanoelectronics, field emission sensors and supercapacitors. [48, 50, 52, 53] The high

surface area associated with CNT along with their very sensitive electronic properties make them a good choice as the sensing platform. [48, 53] CNT can broadly be divided into single walled carbon nanotubes (SWCNT)and multi walled carbon nanotubes(MWCNT). SWCNT are created by rolling the graphene sheet once. [49,53]they are generally chemically inert and therefore physisorption or non-covalent interaction are the more likely mechanisms of binding with analyte for sensors. Although, functional groups could be covalently bonded to the tubes to induce covalent with analyte, this is rather cumbersome and time synthetically challenging [53] Given to their area and properties, CNT perform well as gas-based sensors, even though they suffer of the issue of limited selectivity. [51] For biosensing purposes their ability to undergo functionalization with targeting moieties renders them amenable to selective sensing.For instance, Zhou et al. showed that DNA-decorated CNT could assist in the detection of circulating tumor cells. [54] There have also been great efforts towards increasing the signal to noise ratio and the possible miniaturization of sensors through the use of these nanostructures. [51]

Apart from being used in the above mentioned areas, CNTs have also been used employed in Raman-based sensing . In particular,they have been employed to create 3D sensing substrates. These substrates, functionalized with a high density of upright CNTs provide a high density of hot spots in 3D. [55] Not only this, but SWCNT can be decorated with nanoparticles or DNA to create composite materials for sensing. Wang et al. used such composites for selectively labelling cancer cells and identifying them through Raman spectroscopy. [56] There have also been reports of colloidal probes functionalized with SWCNT and nanoparticle aggregates to study the intracellular trafficking and surface presentation of small peptide-MHC1 class complexes by decoding their Raman peak pattern. [57] The use of SWCNTs for SERS-based sensing has also become a promising field of study. With this thought in mind, we created SWCNT-functionalized substrates, by combining the bottom-up substrate functionalization approach described in Chapter 2 to detect Phe, the main biomarker for PKU. The sensing scheme is shown in Figure 3.1 and 3.2

In addition to SWCNT, we are also interested in using gold nanostars for sensing

Phe levels. Nanoparticles are usually materials with at least one dimension smaller than 100 nm. The small size of nanoparticles is usually associated with high surface to volume ratio, thus providing large numbers of interaction sites for the analyte sought. Physical properties of nanoparticles can readily be altered by chemical modification that could involve the composition or morphology. [58] The field of nanotechnology has come long way in terms of control over the shape, size, morphology, and functionalization of nanoparticles. [58, 59] As a result of this development, nanoparticles have recently found substantial application in biomedicine. There are different kinds of metallic nanoparticles, but gold nanoparticles have garnered special interest from the scientific community. This could mainly be attributed to their ease of synthesis and manipulatin, strong binding affinity to thiols, disulfides and amines, and tunable optical, electronic and physicochemical properties. [59] In particular, the optical response, which in the noble metal nanoparticles is uniquely defined by the surface plasmon resonances,can be readily altered by changing the shape, size, morphology, and the surrounding environment of these nanoparticles, including the generated functionalization steps. All these properties enable the user to design transduction mechanisms that can find numerous applications based on the design scope. [58] For instance, these nanoparticles find application in the field of sensing, targeted drug delivery, imaging, photothermal and photodynamic therapy, therapeutics, detection and diagnostics and biolabeling. [59] Not only the material makes a difference but also the shape. According to Elahi et al. anisotropy in the structure and size of nanoparticle induce changes in structural, optical, electronic, magnetic, and catalytic properties and can be usually have better performance than the spherical gold nanoparticles. [59] Currently, there are well established protocols for the synthesis of gold nanospheres, nanostars, nanorods. [60–63] Not only this, the protocols have been extensively studied for the effect of different parameters on the size and morphology results for a particular synthesis. Thus, these aspects can be readily modulated. [61–63]

According to Nathaniel et al. the size of the nanostructures is highly advantageous as it provides means to transduce the physical and chemical signals that might otherwise go unnoticed in bulk materials. [58] As a result, nanostructure are a very useful tool for

developing sensing assays. The nanoparticles cab be conjugated with antibodies and aptamers to provide high selectivity. Apart from labeled detection schemes, there have been a lot of work being done on label-free assay. Zheng et al. have discussed in details the label free SERS in details. [64]

3.1.1 Sensing Modality Design

Multiple sensing modalities were developed for Phe detection. We found that it was difficult to detect Phe with nanostars in neutral pH. However, due to the structure of CNT, Phe readily adsorbed on the sensor, giving response. However, we were able to detect Phe with nanostar-based substrates at extreme pH values.

The sensing modality for neutral to slightly basic pH conditions was engineered using SWCNT. SWCNT have a large surface area that is available for $\pi - \pi$ interactions with Phe. [65] The system was designed as shown in the figure 3.1 and 3.2. First, the thin-film-gold substrates were functionalized with cysteamine. Thereafter, SWCNT were functionalized on the resulting substrate. Zhang et al. have reported the functionalization of SWCNT through interaction between COOH group on SWCNT and NH_2 group from cysteamine. [66] This sensing modality provide peaks for two different pH values (5.6 and 9.3) that overlaps with certain Phe peaks.

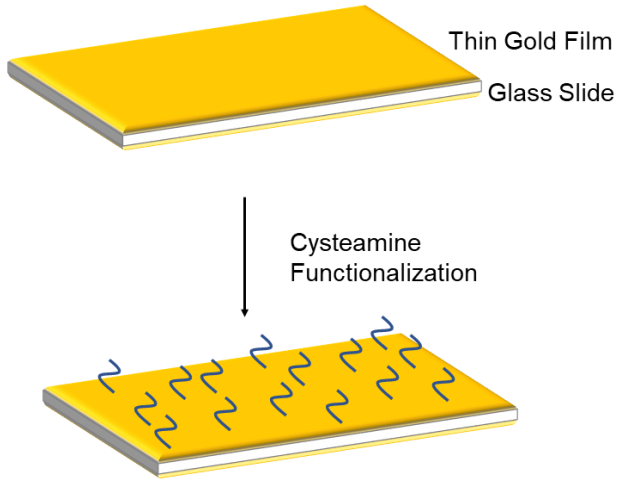

Figure 3.1: Scheme showing the functionalization of thin-flim-gold substrates with cysteamine. This process is common for all the substrates prepared in this study

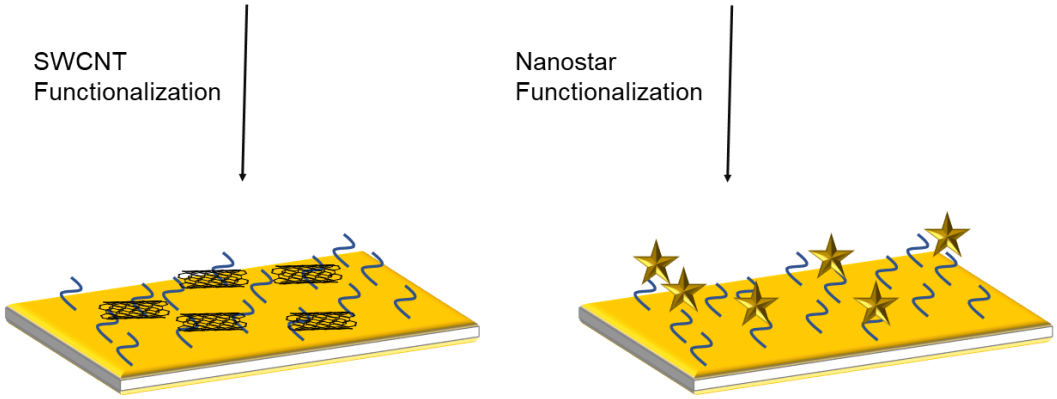

Figure 3.2: Functionalization of SWCNT and nanostars for the SWCNT-based sensors and nanostar-based sensors, respectively on cysteamine-functionalized substrates

For the second scheme, nanostars were functionalized on gold-thin-film substrate. Figure 3.1 and figure 3.2 schematically describes the functionalization scheme, which

leverages, for recognition, the interaction of Phe with gold via amino and carboxy moieties. The pH for this scheme was 12.8 and 0.05 as the nature of amino and carboxy group would be different at these two pH values. This schemes were chosen to get a different response from the same analyte. Through this approach we found that the interaction is different depending on the pH of the solution, with almost negligible interaction at neutral pH.

For the third scheme, we functionalized the thin-gold-film substrates with gold nanostars, followed by the thiolated- β-cyclodextrine-ferrocene complex. This modification is required to achieve a detectable signal transduction in conditions at which Phe does not effectively interact with metallic nanoparticles. [67] In order to do that, we functionalized the nanoparticle surface with cyclodextrins, which are naturally occurring macrocyclic glucose polymers containing a minimum of six D(+)-glucopyranose units. [68](1) For our study purposes, we used thiolated-β-cyclodextrine (β-CD) consisting of seven glucopyranose units. β-CD is shown to from inclusion complexes with ferrocene (figure 3.3). [68–70] (1,2,3).

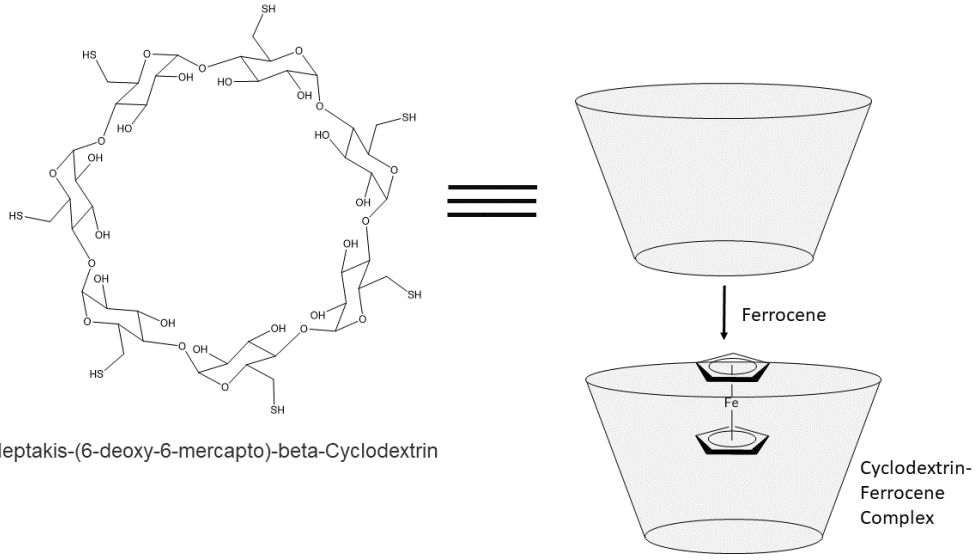

Figure 3.3: Structure of the thiolated-β-cyclodextrine used for creating cages that can host ferrocene. thiolated-β-cyclodextrine will be equivalently represented as a cage for simplicity in the scheme for the rest of the figures.

The reasoning behind this approach was to alter the Raman response as Phe interactes with the substrate. When the substrate is exposed to Phe, which has higher affinity for cyclodextrine in comparison to ferrocene, ferrocene is replaced by Phe, leading to a modification in the Raman peak pattern. [69] This design would detect Phe concentration through decrease in the intensity of signal of the substrate itself, rendering it an ON/OFF sensor. Figure 3.3 shows the thiolated-β-cyclodextrine used as a cage for Phe capture. Figure 3.4 shows the addition of these cages to the nano-structured surfaces and figure 3.5 shows the replacement of ferrocene by Phe.

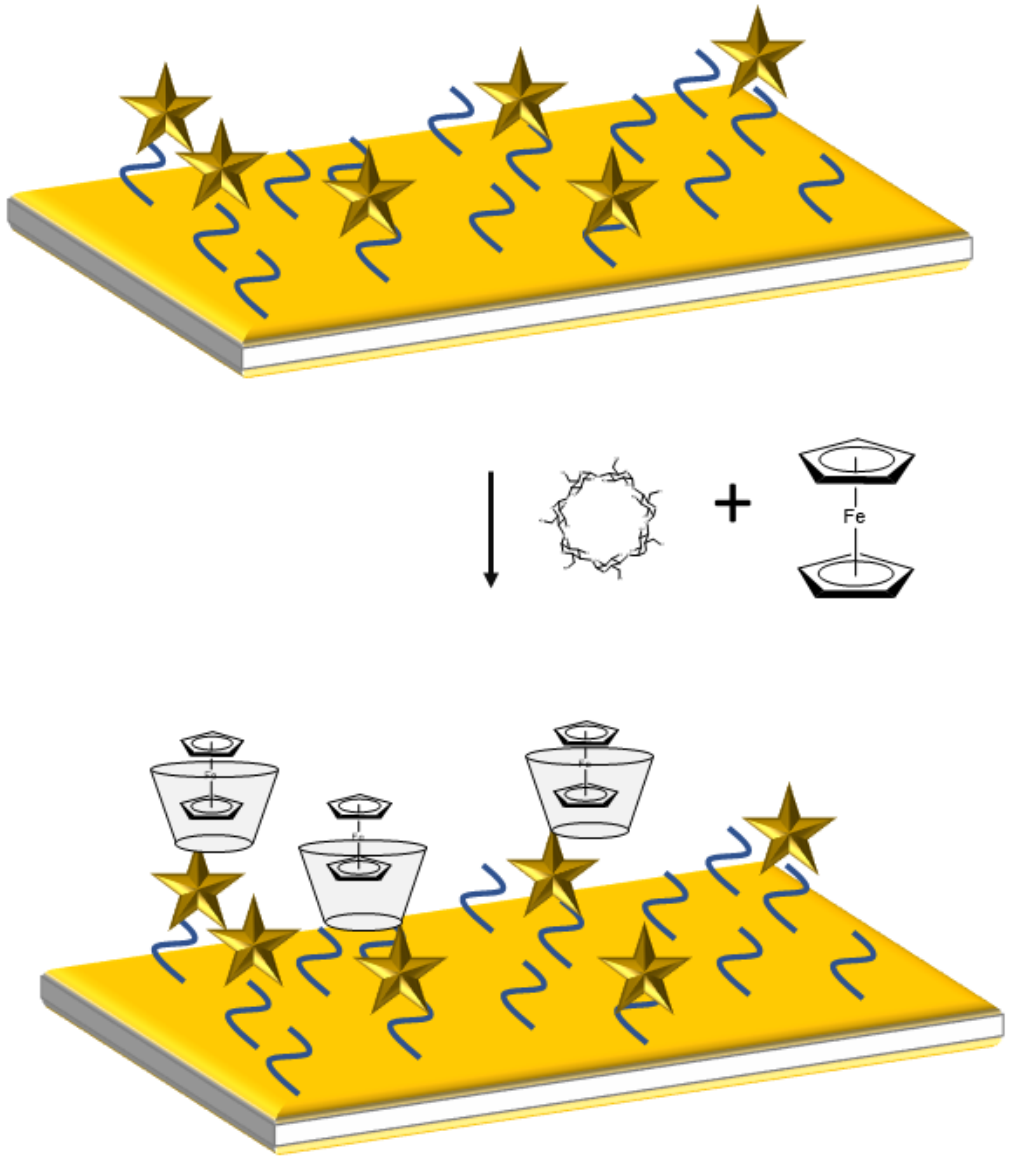

Figure 3.4: Schematic representation of the process flow to functionalize the substrate with the thiolated-β-cyclodextrine-Ferrocene complex. Gold nanostar-coated slides are incubated with thiolated-β-cyclodextrine and Ferrocene. Thiol groups will have affinity for gold and allow for binding the cuclodextrine to the substrate, while ferrocene is known to form complexes with β-cyclodextrines, as host-guest complex.

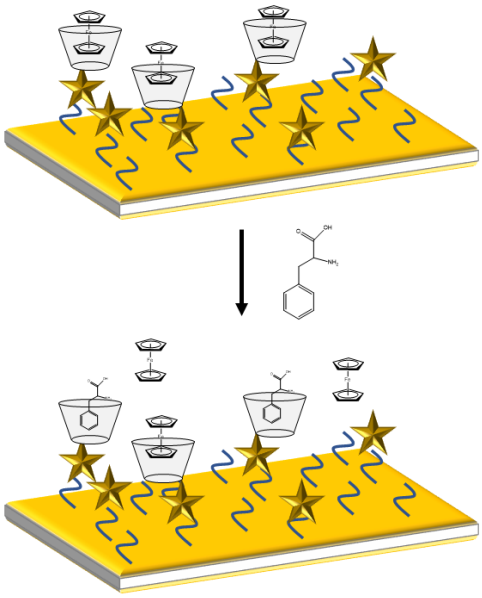

Figure 3.5: Representation of the sensing mechanism for the host-guest configuration.Thiolated-β-cyclodextrine-Ferrocene functionalized on the substrate are characterized by the Raman response of ferrocene. However, Phe is shown to have higher affinity for β-cyclodextrine thereby replacing the ferrocene from the cages. The removal of ferrocene from the cages causes a decrease in the Raman signal intensity from ferrocene and hence can be used to indirectly detect Phe.

Though the first two schemes ideal for Phe detection without labels, the ability of these sensors to detect Phe in complex matrices can be difficult due to contribution of similar peaks from other molecules. For instance, there could be peaks for Phe that might overlap with vibrations from the other similar molecular vibrations from other molecules present in biological fluids. As mentioned earlier, nanostructures provide an effective means to for signal transduction. By changing the morphology and composition of the material,we are changing the transduction mechanism and hence the response. Taking this approach can open up opportunity for label-free detection of analytes based on the alteration in the interaction environment around the analyte. In order to achieve specificity through this mechanism, a multi-site approach similar to the one we followed for the Dual Modality Multi-site sensing was taken. In order to detect the Phe we varied the pH of the system. Multi-site in this case was achieved by using different

nanostructure displaying different interactions with Phe, leading to different response for it. In addition, we chose distinct values of pH for these nanostructured based substrates. Value of pH have bearing on the interaction of Phe with these substrates. The aim of this diversity is to pave path for label-free robust detection of Phe.

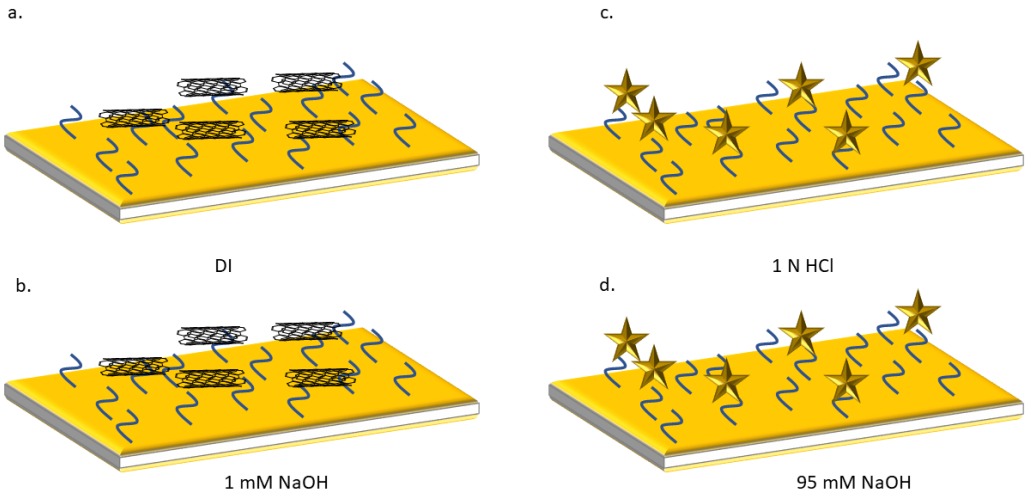

Figure 3.6: Multi-site sensing paradigm for label-free detection of Phe withimproved selectivity without labels. Multi-site conditions are created by inducing diversity in the sensing substrates and sensing environment. (a) and (b) are the substrates made using SWCNT and, (c) and (d) are the substrates made using nanostars. The sensing environment of sample (a) is at a neutral pH, for (b) the sensing environment contains 1 mM NaOH making making pH slightly basic (9.8), for (c) sensing environment is highly acidic(1 N HCl,pH close to 1) and for (d) the sensing environment is highly basic (95 mM NaOH, close to 13)

In the current project,we developed multiple sensing modalities for Phe. In order to carryout the multi-site measurements, the scheme shown in figure 3.6 was followed. The measurements for the system were carried out for four different site, each giving a different response. When carrying-out a multi-site measurement the cost-benefit ratio should be high enough and therefore, we followed a low-cost bottom-up design approach. The detection scheme would involve four substrates, two made with SWCNT and two

made with nanostars.

3.2 Materials and methods

3.2.1 Materials and Instrumentation

Gold(III) chloride trihy-drate ($HAuCl_4 3H_2O$) was purchased from Acros Organics. Trisodium citrate dihydrate ($C_6H_5O_7Na 2H_2O$) was purchased from Acros Organics Cysteamine, 4-aminothiophenol (4-ATP) and single-walled carbon nanotubes, conductive aqueous ink were purchased from Sigma Aldrich. Ultrapure water (18.2 Mcm) was used for preparing the solutions. All glassware was aqua regia cleaned. The Raman spectra were obtained using a Renishaw InVia Raman microscope. Dropsense DRP 220AT screen printed electrodes (SPEs) were purchased from Metrohm USA. Sodium Hydroxide (NaOH) and Hydrochloric acid (HCl) were purchased from Fisher Scientific.

3.2.2 SWCNT-based substrate preparation

Gold-coated glass slides were incubated in 0.1 M aqueous cysteamine overnight and washed with DI water after incubation. Next, 300 ul of 0.033mg/ml of SWCNT were used to incubate the substrates, which were then washed with deionized (DI) water after incubation.

3.2.3 Effect of pH on the Raman Signal from SWCNT-based Phe Sensors

1 N HCl, 95 mM NaOH, and 1mM NaOH aqueous solutions were prepared and employed to dissolve Phe to a concentration of 1mM. A control solution in pure DI water was also prepared . 2 ul of 1mM Phe in DI, 1mM NaOH, 95 mM NaOH, and 1 N HCl were dropcasted on the substrates and left in a humidified chamber for 30 minutes. For control studies, 2 uL of DI, NaOH, 95 mM NaOH and 1 N HCl were dropcasted on the substrates. The solution was wicked with kimwipe before Raman measurements. Raman measurements were carried out on the samples using a Renishaw InVia Raman

microspectrophotometer employing 633 nm laser excitation, 1 accumulation, 3 s exposure, 10 % laser power. A 50x objective was used to acquire the 36 static points map on each substrates. The spectra were baseline subtracted followed by averaging to obtain the final spectrum.

3.2.4 Surfactant-Free Nanostar Synthesis

Gold stock solution (2 ml of a 0.025 M HAuCl43H2O solution) was added to 48 ml DI water while stirring. 200 l of 1 N HCl were added to the solution, followed by 70 l of 15 nm gold nanospheres having absorbance of 1. Path length of the measurement was 1 mm. Thereafter, 2 ml of 3 mM $AgNO_3$ and 1 ml of 100 mM ascorbic acid were added, simultaneously. The synthesis was stirred for additional 7 minutes.

3.2.5 Nanostars-Based Substrate Preparation

Gold-coated glass slides were incubated in 0.1 M aqueous cysteamine overnight and then washed with DI water. Next,300μl surfactant free gold nanostars with absorbamce value of 0.2 in a 1mm path length measurement were used for functionalization on this slide through incubation for two hours. The slides were then washed with DI.

3.2.6 Cyclodextrin Ferrocene Complex-Based Substrate Preparation

0.6 mM each of cyclodextrin and ferrocene in ethanol were added to nanostar functionalized substrates and left overnight for incubation. Later, the substrates were washed with ethanol. Raman measurements were carried out on the substrates following dropcasting the sample solutions on the prepared substrates. Details of different measurement are added in the results and discussion section for ease of reference.

3.3 Results and Discussions

3.3.1 SWCNT-Based Phenylalaine Detection Scheme

SWCNT provide high surface area for interaction with analytes. The possibility of interaction increases when the analyte being tested has an aromatic structure that can

interact with SWCNT through $\pi - \pi$ stacking. With this rationale, we designed the substrates functionalized with SWCNT. Figure 3.2 shows the schematic of the sensor used. We then tested the sensor for detection of Phe aqueous solution . Figure 3.7 shows the sensor response in presence and absence of Phe. The extended Raman scan measurements were carried out at 633 nm laser.

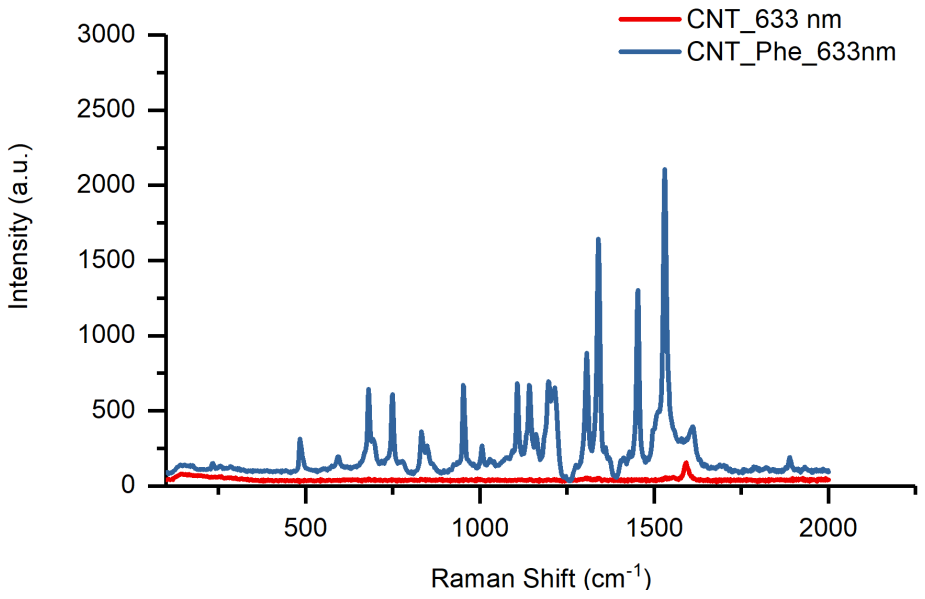

Figure 3.7: Response of SWCNT-based sensors for 1 mM Phe in DI water. The high response can be attributed to $\pi - \pi$ interactions between the Phe and SWCNT

The selectivity of the system was tested by employing glycine and alanine. Raman spectra for 25 point maps were collected for 2 μl of 1mM of phenylalanine, alanine and glycine on the SWCNT- based substrates. As can be seen the figure 3.8, there are detectable Raman peaks for phenylalanine but not for alanine and glycine. As the amino acid group is same in all the three analytes, we believe that the detection mechanism has a little contribution from capture of these molecules through amino or carboxy group on aliphatic molecules. Thus, the major interaction for capture can be due to $\pi - \pi$ electron interaction from the phenylalanine ring and the SWCNT walls. There has been a systematic study carried out by Piao et al. elucidating the interaction between SWCNT and Phe in great detail. [65]

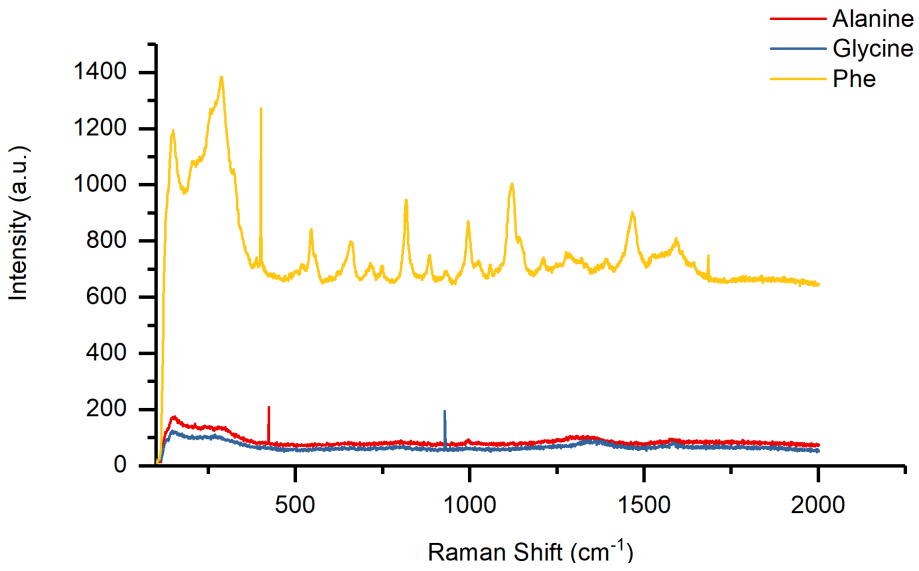

Figure 3.8: Averaged Raman spectra from the maps collected on the substrate for alanine(red), glycine(blue) and phenylalanine (yellow). The spectra show that the interaction between Phe and SWCNT gives good response in comparison to alanine and glycine, suggesting that the interaction is mainly driven by $\pi - \pi$ stacking interactions.

SWCNT functionalization was also carried out on the screen printed electrodes (SPEs) reported in Chapter 2. This approach, however, led to very intense Raman signature from SWCNT, leading to an inability to distinguish the Phe peaks from the Raman pattern, as shown in 3.9. Thus, there is further need of optimization of this process if these measurements are to be carried on the SPE.

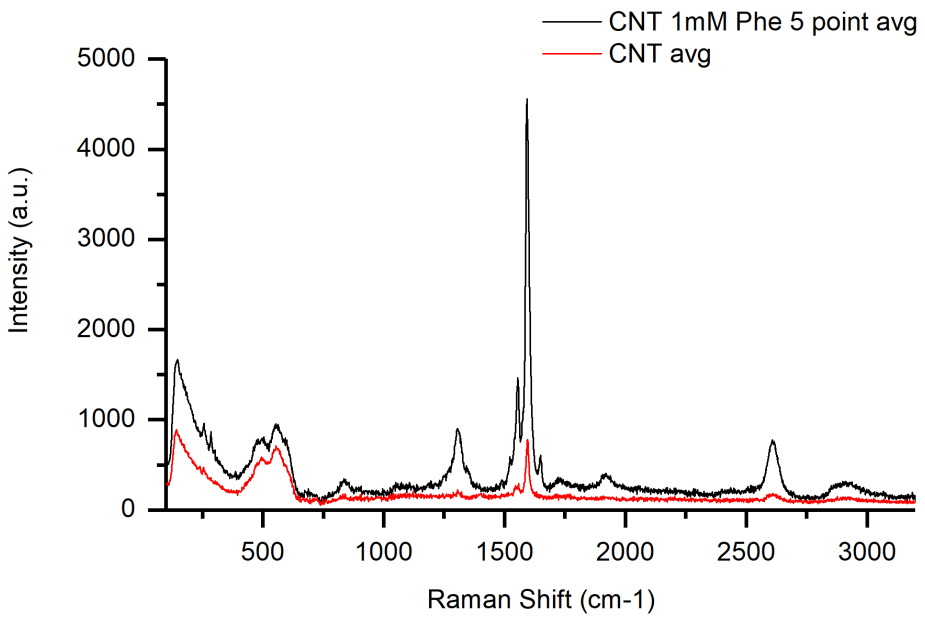

Figure 3.9: Average of 5 Raman spectra for 1mM Phe dropcasted on SPE functionalized with CNT. The spectral difference between the control and 1 mM Phe cannot be observed.

3.3.2 Cyclodextrine- Ferrocene Complex-Based Phenylalanine Detection Scheme

Another set of substrates were prepared by functionalizing nanostars on the thin-film-gold coated slides. Thereafter, a β-CD and ferrocene (Fc) mixture was added to functionalize β-CD and Fc complex . According to Alvarez-Puebla et al [71], CD has a very small Raman cross-section making its contribution to the overall Raman signature very small. Fc has a very characteristic Raman signature. The samples were then tested to identify the unique Raman signature. Once the tests were done, 1mM Phe was dropcasted on the substrate and the Raman measurements were taken again. As can be seen in figure 3.13, there are peaks from the nanostar based substrates and some additional peaks from the CD and Fc functionalized on the substrates.

We compared the response from nanostar-β-CD-Fc functionalized substrate,nanostar-β-CD and Fc spectra. Figure 3.10, 3.11 and 3.12. The highlighted regions show the

peaks in the nanostar-CD-Fc response which are distinct from the Nanostar-CD response but clearly assignable to Fc. 831, 845, 1108,1190 and 1355 $cm^{-}1$ are the main peaks identified. 845 $cm^{-}1$ can be assigned to A_1g CH bending ($\perp$), 1108 $cm^{-}1$ to E_1g CH bending ($\parallel$), 1190 $cm^{-}1$ to CH bending ($\parallel$) and 1355 to CC stretch. [72, 73] Normalization of spectra was carried out to compare the peaks. High peak intensity at 1108 $cm^{-}1$ leads to a difficulty in analyzing smaller peaks in the spectra. Therefore, for figures 3.11 and 3.12, normalization of spectra was carried in the range 500 to 1000 $cm^{-}1$ and 1100 to 1960 $cm^{-}1$.

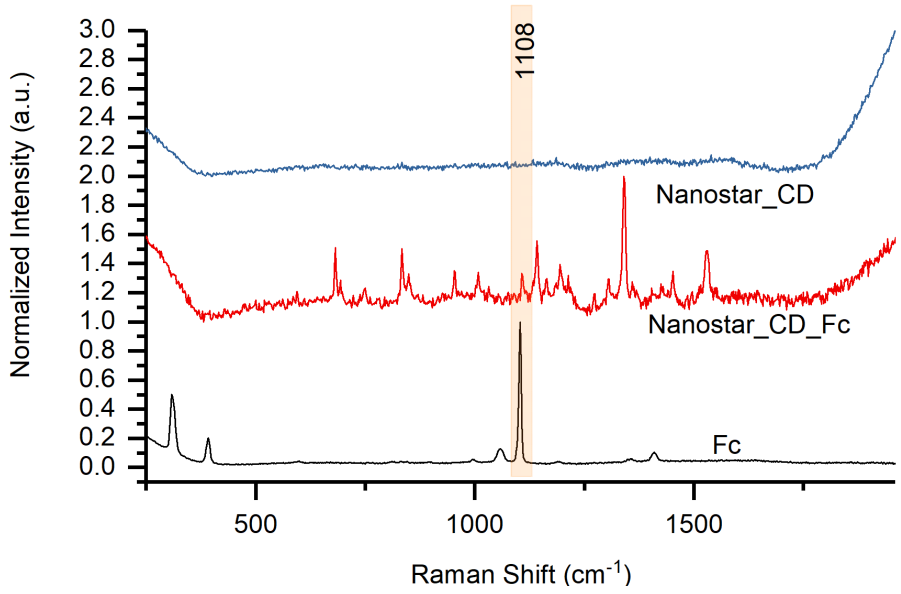

Figure 3.10: Figure shows the SERS response for the nanostar-based substrate functionalized with thiolated-β-CD (blue), nanostar-based substrate functionalized with thiolated-β-CD-ferrocene complex and ferrocene. The spectra were normalized for ease of peak comparison. Peaks common only between Fc and thiolated-β-CD-ferrocene complex substrates are highlighted

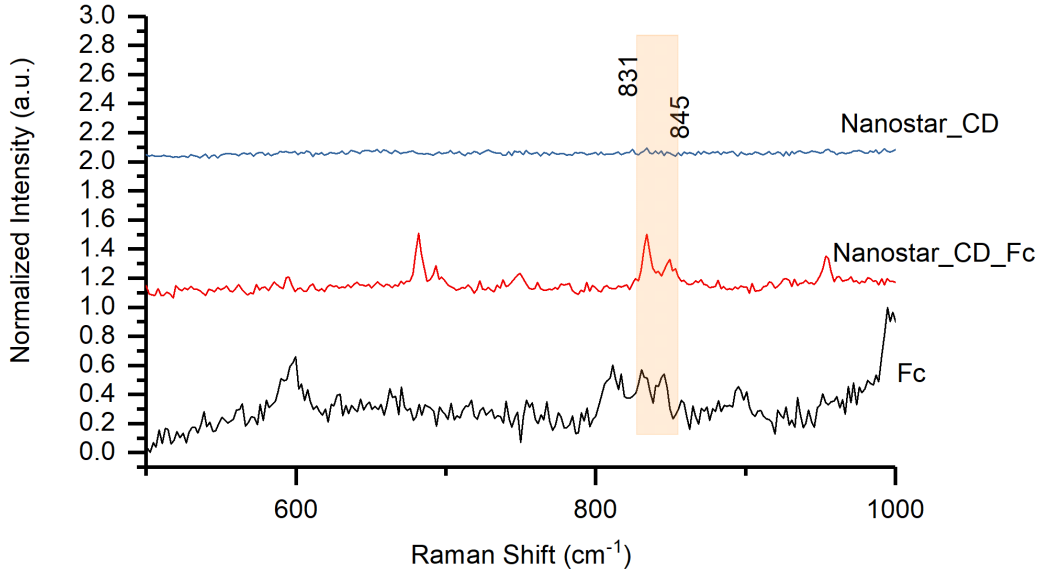

Figure 3.11: Normalized spectra in the range 500 to 1000 $cm^{-}1$ to have better visualization of smaller intensity peaks of Fc. Characteristic peaks of Fc evident in thiolated-β-CD-ferrocene complex substrates are highlighted

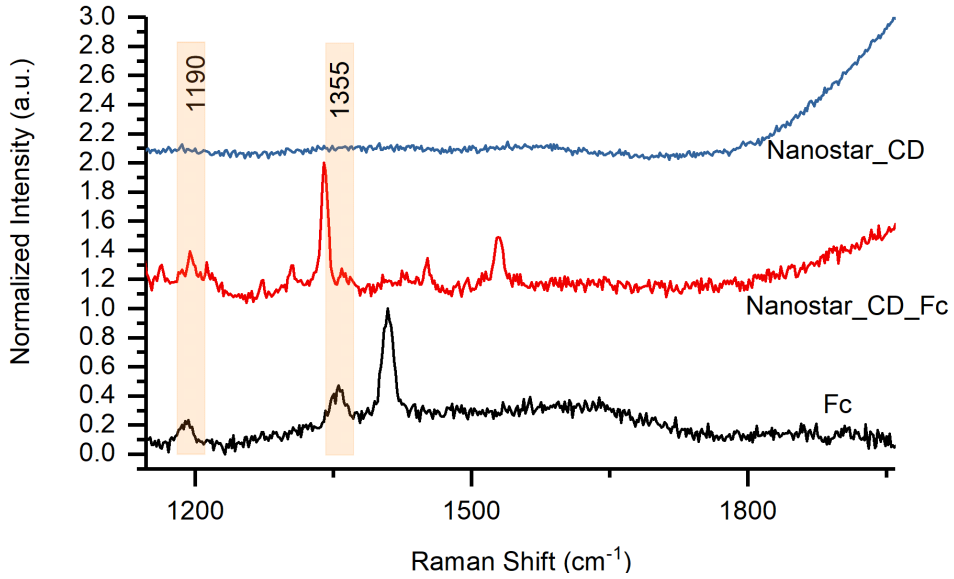

Figure 3.12: Normalized spectra in the range 1100 to 1960 $cm^{-}1$ to have better visualization of smaller intensity peaks of Fc. Characteristic peaks of Fc evident in thiolated-β-CD-ferrocene complex substrates are highlighted

Upon incubation with Phe, the samples show reduction in the Fc peaks, as expected. Phe is shown to have higher affinity towards CD than Fc leading to the replacement of Fc from CD-Fc complex. [69] This system acts by measuring the reduction in signal from Fc for detection of Phe. There are several SERS detection systems which rely on decrease in signal intensity from a probe molecule to carry out detection, especially for molecules with small Raman Cross sections.

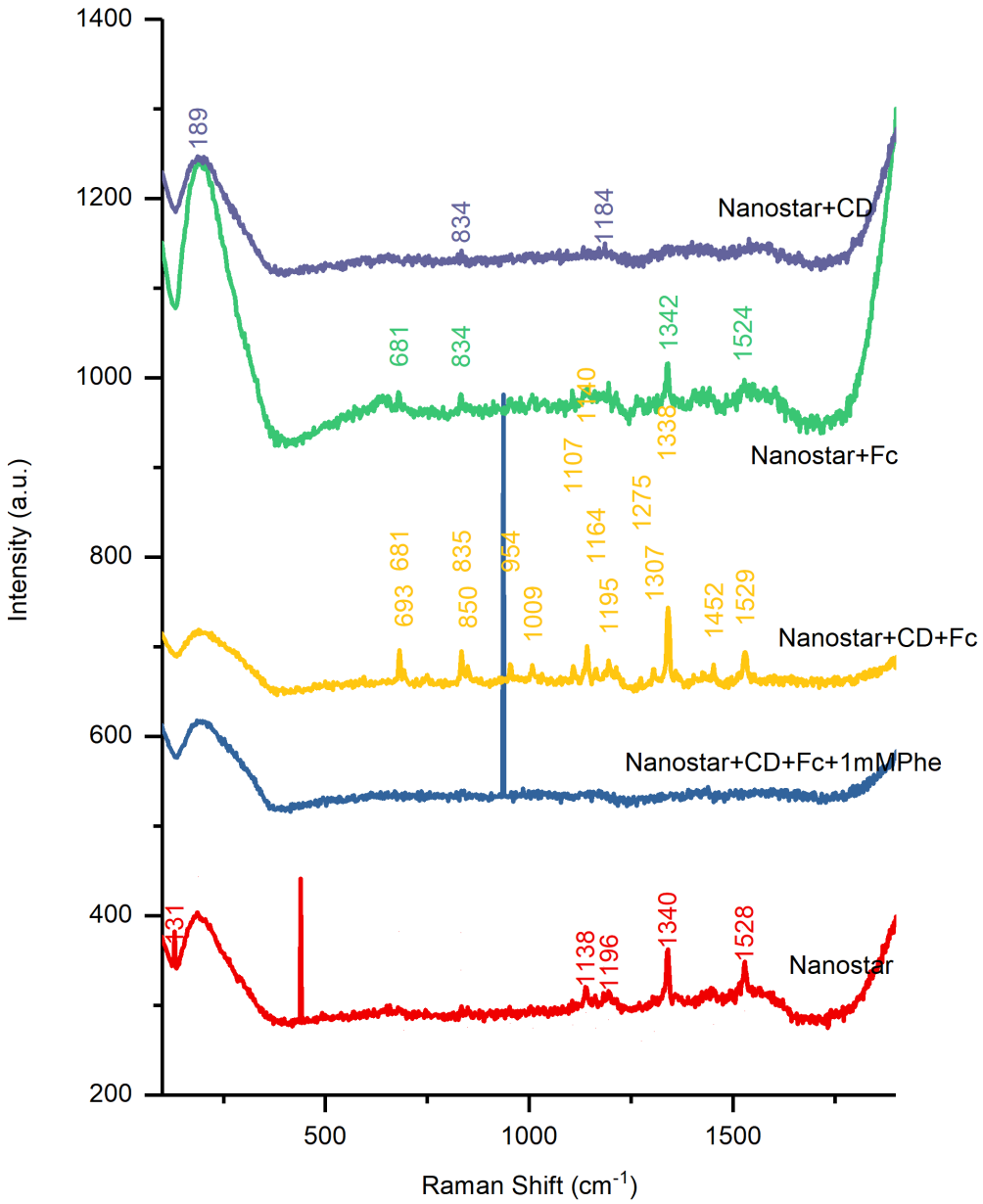

Figure 3.13: Average Raman spectra for nanostars, nanostars functionalized with CD-Fc complex and thereafter incubated with 1mM Phe, nanostars substrate functionalized with Cd-Fc complex, nanostars incubated with Fc and nanostars substrates incubated with CD. The figure shows that there is Raman signature from FC in the CD-Fc complex functionalized on the substrates. This signal reduces in strength after incubation of 1 mM Phe on this substrate

3.3.3 SWCNT-Based Phenylalanine Sensors

Dependence of peak intensity on molecular adhesion was studied by varying the pH of the solution. NaOH and HCl were used to set the pH of the solutions. 1mM Phe solution was prepared using 1 mM and 95 mM NaOH aqueous solution to have basic solutions and 1 mM Phe in HCl was used to make the acidic solution. These concentrations of NaOH and HCL were chosen given to pKa values of Phe(pKa_1 1.83 and pKa_2 9.13).

Figure 3.14 shows the baseline subtracted averaged spectrum for 1 mM Phe in different pH solutions. The response is good for the DI and 1 mM NaOH being used for making the solutions.

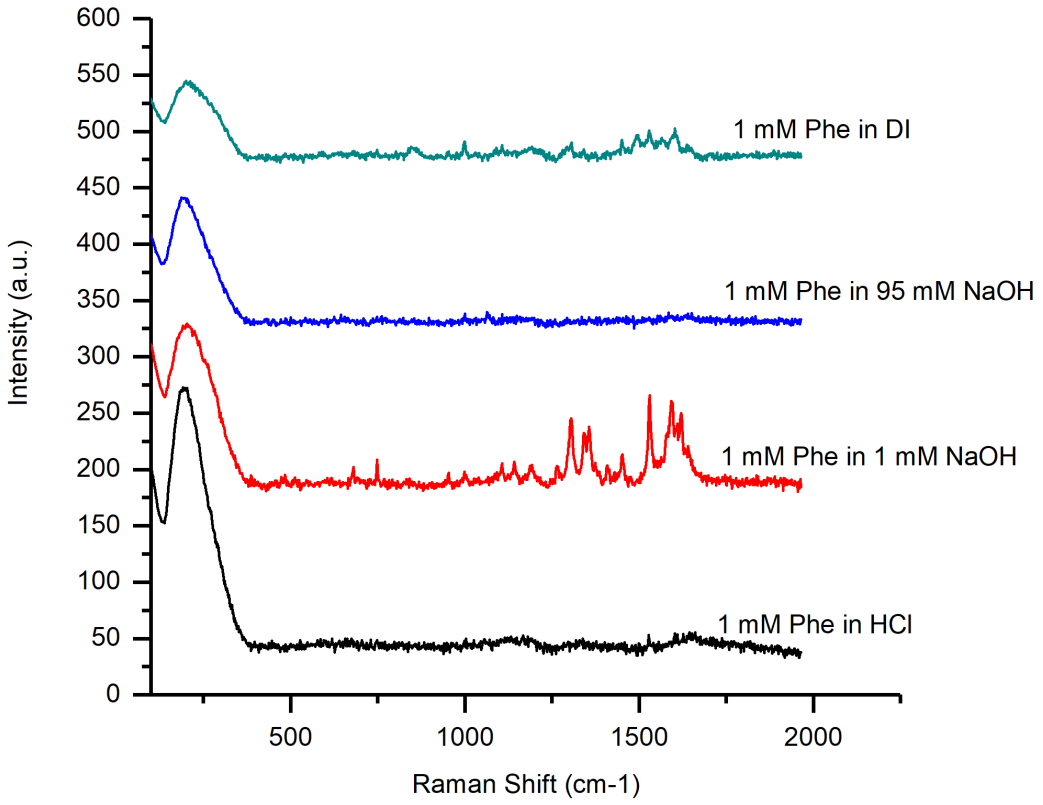

Figure 3.14: Average Raman spectra for 1 mM Phe in DI, 1mM NaOH, 95 mM NaOH and 1 N HCl for SWCNT-based substrates. As can be seen the figure the peak intensities are highest for 1mM Phe which is at the pH of 9.3. pH of 5.6 also provides detectable response.

1 mM Phe in 1mM NaOH (pH 9.8) has the highest peak intensities. These findings are similar to the pH dependence study reported by Jha et al. [74]. The height of the peaks increases with increase in pH. Figure 3.15 shows the comparison for 1mM Phe in 1 mM NaOH against a 1 mM NaOH control, both on SWCNT based substrates. It is also compared with the pure Raman spectrum of Phe. The highlighted bands show the Phe peaks, which are present only for the positive control. The peaks at 914, 1412 ad 1587 $cm^{-}1$ are the peaks that are unique to Phe. The peak at 914 cm-1 can be assigned to C-C stretch, the peak at 1412 could be attributed to COO- stretching

or ring stretching/CH bending, [75] While the peak at 1587 $cm^{-}1$ can be assigned to in-plane ring stretching. [75].

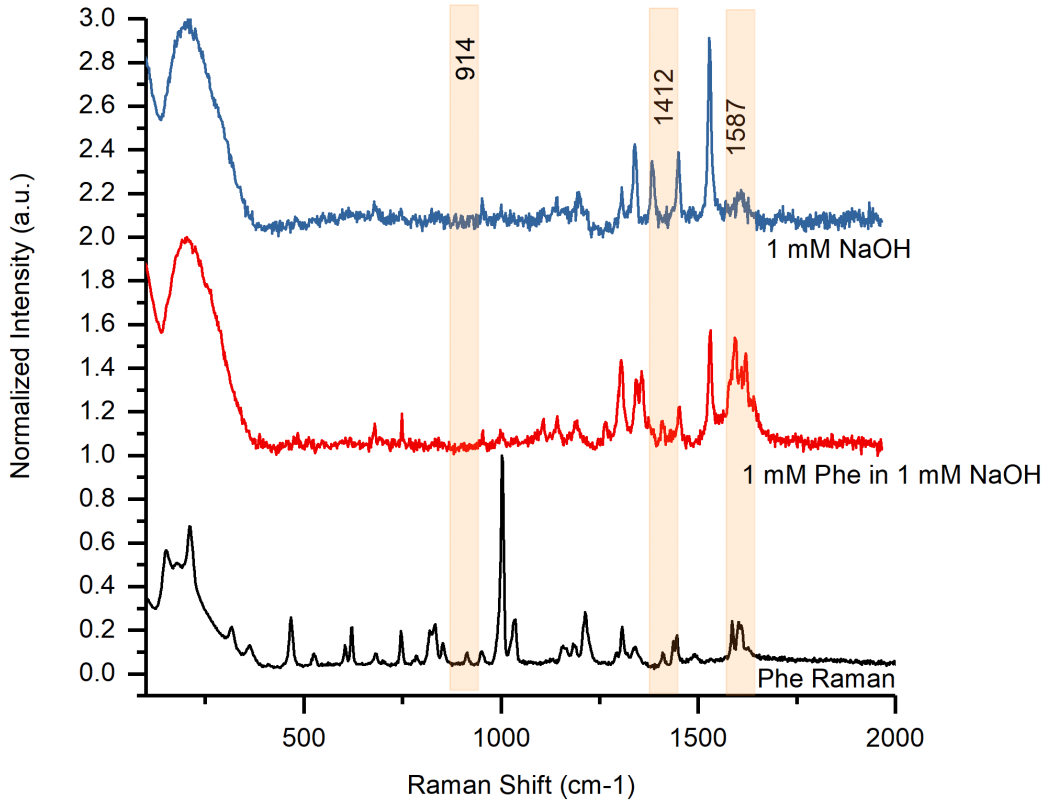

Figure 3.15: Average Raman spectra for 1 mM Phe in 1mM NaOH, for only 1 mM NaOH control and for pure Phe. Phe characteristic peaks detected only in the positive control are highlighted.

We also looked into the response of the same system at 95 mM NaOH instead of 1 mM NaOH. Upon this change, we do not see any peaks from the Phe. This could be inferred as the molecule does not have interactions with SWCNT at this pH that could give rise to SERS. Figure 3.16 shows the response for this system. At a very high pH the molecule will have a negative charge which might be the reason for reduced interaction with SWCNT.

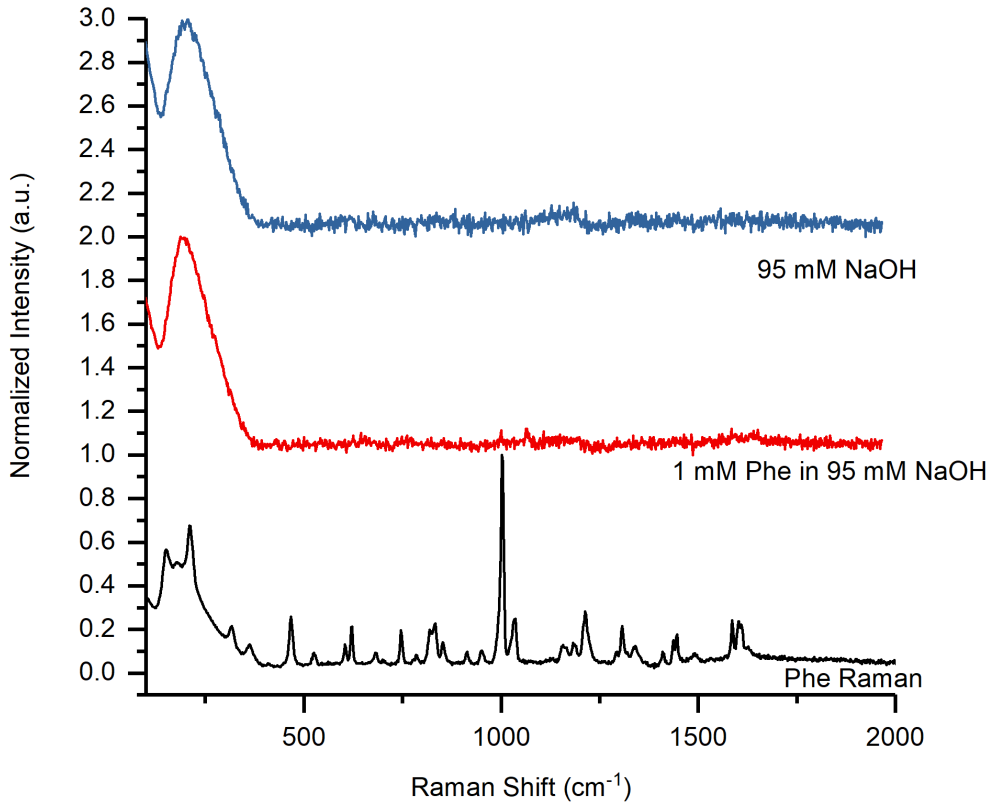

Figure 3.16: Comparison of spectra from 1 mM Phe in 95 mM NaOH and just 95 mM NaOH on the SWCNT-based substrates with pure Phe. There was no response from Phe in such highly basic solution for SWCNT-based substrates

A similar study was carried out at 1 N HCl with a very low pH to get information on the interaction, which shows that the SERS response of Phe is again very low. At a very low pH, Phe molecule will posses an overall positive charge that can again could be the reason for reduced interaction with CNT.

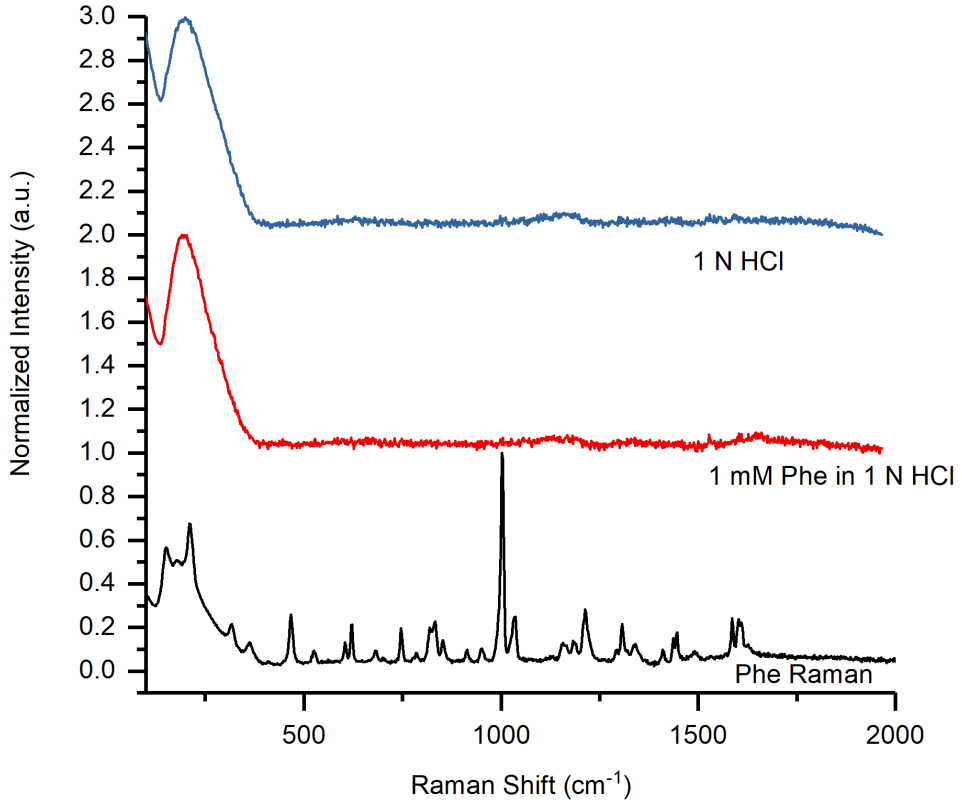

Figure 3.17: Response of 1 mm Phe in 1 N HCl and just 1 NHCl on the SWCNT-based substrates compared with pure Phe Raman. There was no response from Phe at highly acidic pH

We did similar studies using DI water for the solution preparation and the results are shown in figure 3.18. The peaks that are present only for the positive control are highlighted. The peaks at 950 cm^1 can be assigned to CH out of plane bending mode, [76] peak at 1038 cm^-1 can be assigned to in plane CH bending. The peaks at 1308 cm^1 can be assigned to CH2 wag and ring stretching.

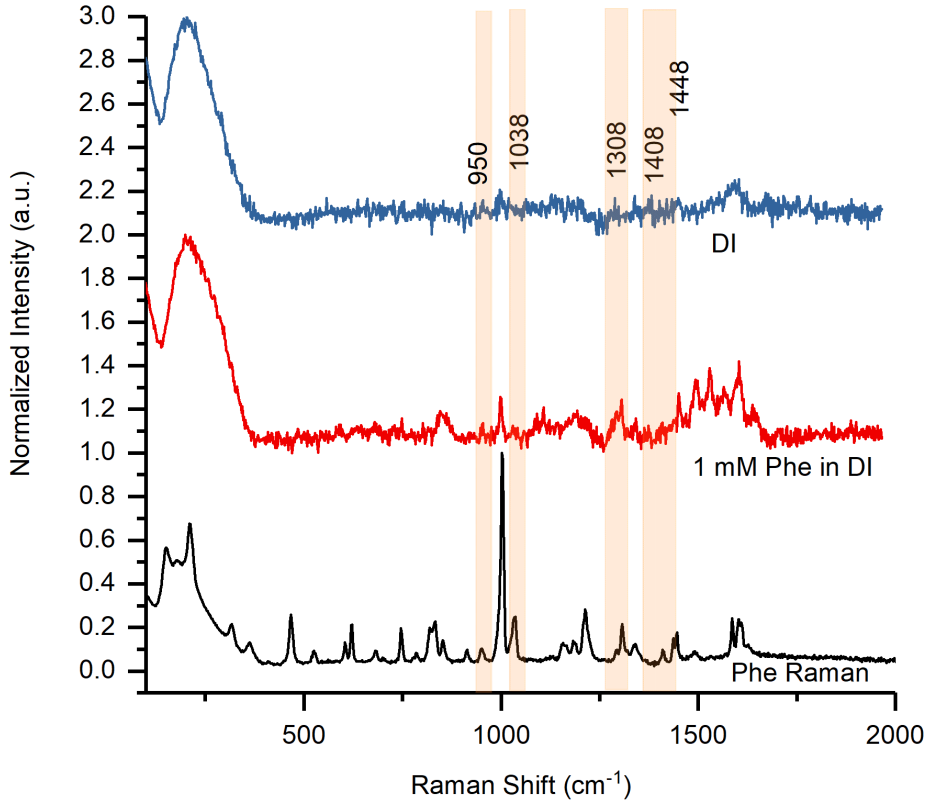

Figure 3.18: Response of 1 mM Phe in DI and just DI on the SWCNT-based substrates compared with pure Phe Raman. There are a number of characteristic peaks of Phe identified that were present only in the positive controls

3.3.4 Nanostar-Based Phenylalanine Sensors

Next we tested the nanostar-based sensor for 1 mM Phe prepared in 1 mM NaOH solution. The unique peaks are highlighted in the plot. Peaks at 468,608, 624, 1587 and 1697 cm^1 were found to be present in the positive control only, which belong to Phe characteristic vibrations. The Peak at 1587 cm-1 can be assigned to in-plan ring stretching, [75,77,78] that at 624 cm^1 can be assigned to one of the phenyl ring breathing vibrations and COO^-1 wag, [79] while the peak at 1697 cm^1 very close to 1710 cm^1 has also been assigned to the NH_3^+ asymmetric band according to Hernandez et al.

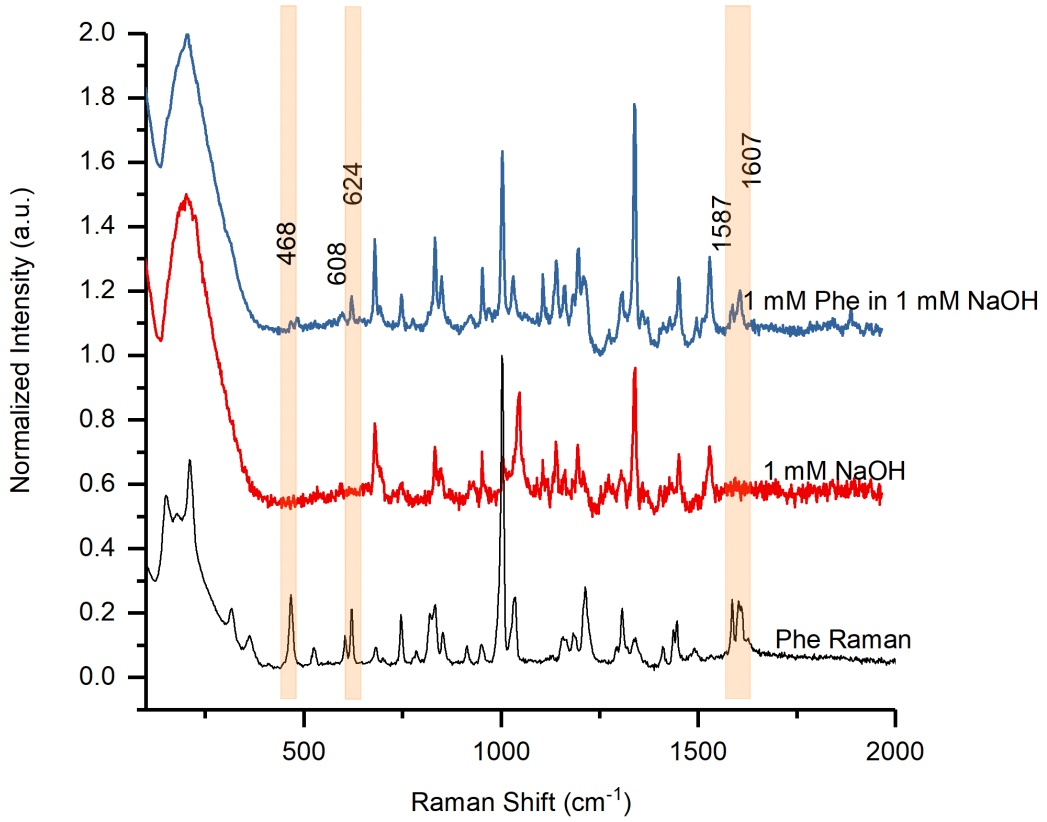

Figure 3.19: Response of 1 mm Phe in 1 mM NaOH and just 1 mM NaOH on the nanostar-based substrates compared with pure Phe. The characteristic peaks of Phe present only in the positive control are highlighted.

The sensor was also tested in 95 mM NaOH similar to SWCNT-based substrate, but the response for it was much better giving 840, 850, 914, 1002, 1042, 1280, 1487, 1583 and 1611 cm^1 distinct peaks in the positive control in comparison to the negative control. The peaks at 840 and 850 cm^1 could be assigned to Fermi resonance between ring breathing and out of plane ring bend overtone. [75]. The peak at 914 cm^1 can be assigned to CC stretching, while the peaks at 1002 and 1042 cm^1 to the symmetric CC stretching and in-plan CH bending, respectively. The peaks at 1583 and 1611 cm^1 have both been associated to the in-plane ring stretching. [75].

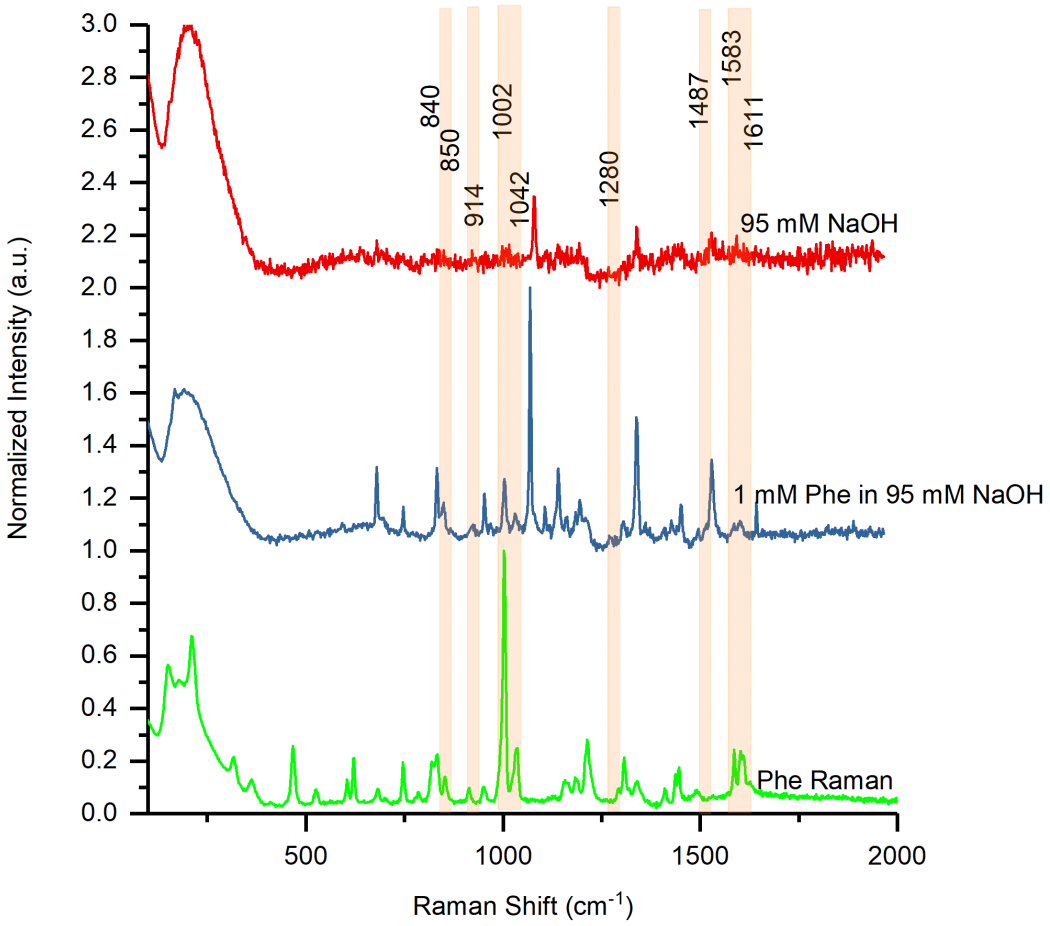

Figure 3.20: Response of 1 mM Phe in 95 mM NaOH and just 95 mM NaOH on the nanostar-based substrates compared with pure Phe. The characteristic peaks of Phe present only in the positive control are highlighted.

We tested the response for the nanostars-based sensors with control solution of Phe in pure DI water. Figure 3.21 shows the response for the sensors. We did not find any unique peak in the positive control when compared with the negative control that might correspond to the vibrations present in the Phe.

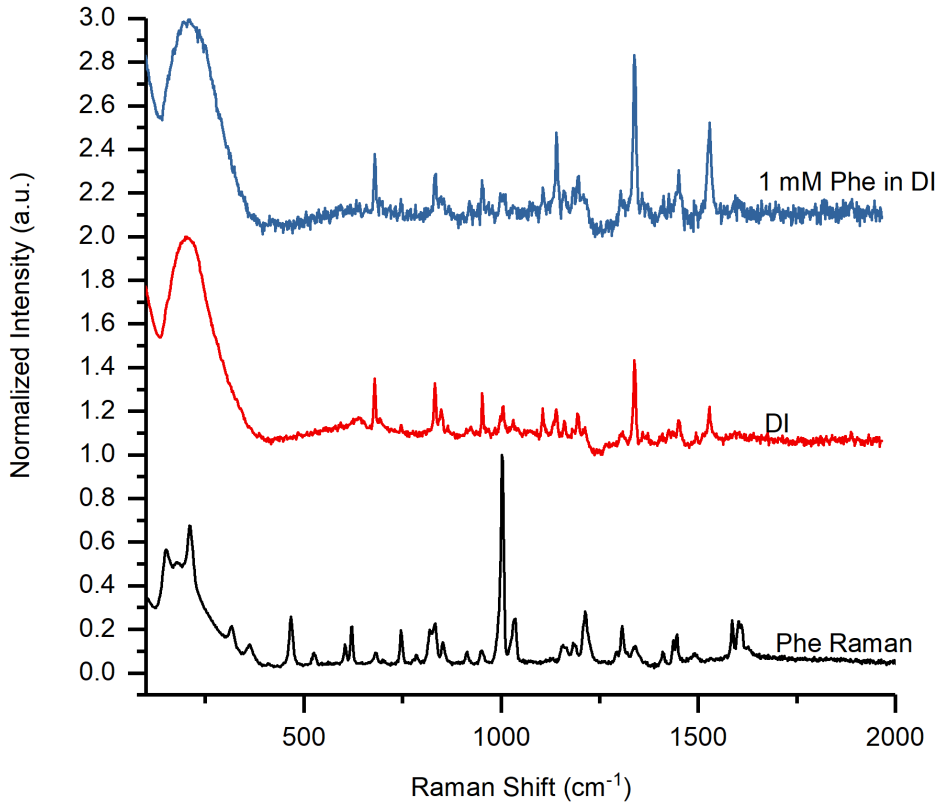

Figure 3.21: Figure shows the response of 1 mm Phe in DI and just DI on the nanostar-based substrates compared with pure Phe Raman. The are no characteristic peaks of Phe present only in the positive control.

Testing nanostar-based substrates with 1N HCl gave a good response with 689, 750,832,850,1031,1211,1308 and 1606 cm^1 as distinct peaks present only in the spectrum for the positive control in comparison to the negative control. The peak at 750 cm^1 can be assigned to the phenyl ring breathing mode. [79]. The peaks at 832 and 850 cm^1 could be assigned to Fermi resonance between ring breathing and out of plane ring bend overtone. [75], while the peak at 1031 cm^1 can be assigned to the ring breathing vibrations.The peak at 1211 cm^1 can be assigned to phenyl-C stretching and the peak at 1308 cm^1 can be assigned to CH_2 wag or ring stretch. The peak at 1606 cm^1 was assigned to in-plane ring stretch. [80]

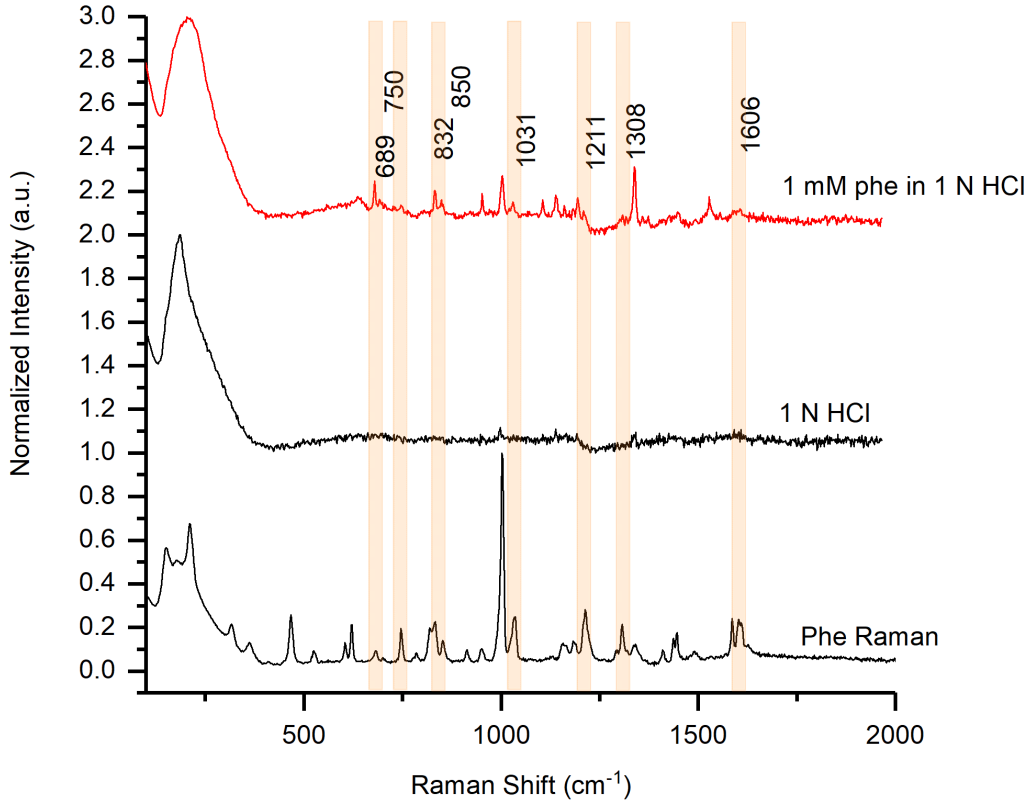

Figure 3.22: Response of 1 mM Phe in 1 N HCl and just 1 N HCl on the nanostar-based substrates compared with pure Phe. The characteristic peaks of Phe present only in the positive control are highlighted

3.3.5 Multi-Site Measurements for Phenylalanine Detection

In order to detect phenylalanine, we aimed to employ the multi-site measurement approach similar to the one we applied for the Dual-Modality Multi-Site sensing, as described in Chapter 2. For Dual-Modality Multi-Site sensing, we were using the concentration of analyte as the main parameter for inducing diversity. In the present work, we introduced diversity through the substrate material and pH. As shown in the previous section, the response for the sensor with CNT is good for 1mM NaOH and DI based solutions while the response for nanostars-based substrates are good for 1 N HCl and 95

mM NaOH based solutions. Responses from such configuration of sensors when combined can provide opportunities to develop ways of detecting the Phe with specificity without need of any labeling entity.

3.4 Conclusions

We developed multiple methods for the detection of Phe. Detection response is highly dependent on the nanomaterials used for the substrate preparation and the pH of the system, as shown in the results sections. Depending upon the response from the combination of pH and substrate multi-site feature definition was chosen. Finalized multi-site features included SWCNT-based sensing sites for 5.6 pH to slightly basic solution pH(9.8) and nanostar-based sensing sites for highly acidic and highly basic solutions. The combined response from the multi-site can be used to pave way for detection of Phe in a robust fashion. Future directions would involve testing the system out in the sample matrix like urine to assess the system performance.

Chapter 4

Quantification of SERS using Machine Learning

4.1 Introduction

Production cost for SERS substrates could be lowered by using bottom-up approaches that rely mainly on self-assembly processes. Colloidal nanoparticles are often used for producing such substrates. As the control over the spatial distribution of nanoparticle is low, such substrates suffer however from reproducibility issues, which lead to variation in SERS intensities not only among different substrates but also within the same substrate at different locations. The surface selection rules, orientation and location of nanoparticle also plays an important role in the resulting intensities. [81] There is a need to develop robust methodologies that can address unexpected enhancements issue commonly encountered for low-cost substrates when trying to quantify the analyte concentrations using SERS intensities. There can different approaches that could be taken to address it. One can be the better control over the self assembly process and the molecular interactions. This approach can be difficult to achieve as it would require optimization for different analyte and nanostructure combinations. Another approach can be analyzing the existing variation in the system and coming up with a process to map the variation pattern with the analyte concentration. In chapter 2 and 3 we addressed this need by using a multi-site measurement approach. In this chapter, we use machine learning on measurements from SERS substrates to develop methods that can provide robust quantification processes. There are studies that suggest that the orientation of molecules can be determined using the SERS. [82, 83] Therefore, the relative intensities can provide information about the orientation. In other words, there would be a specific intensity associated with certain orientation and concentration of the molecule. When working with SERS substrates made from the colloidal gold, we usually consider certain

peak information from multiple places on the substrate. Thereafter, an average is taken to provide a representative quantity for a concentration of analyte when building a calibration curve. Therefore, the process of averaging is to overcome the point to point variation arising from surface features, molecular orientation, and location. Herein, we aim to implement an approach to correlate the spectral signature to the concentration using supervised machine learning and eventually use it for concentration prediction purposes. We decided to use machine learning for the classification of data into different concentration classes. Currently, there are only few data driven studies available for quantification of analyte concentration through Raman. Though literature in analyte classification using data driven approaches is comparatively more prevalent. Ellis et al. showed that Raman spectroscopy along with Fourier-transform infrared spectroscopy in combination with appropriate machine learning strategies could differentiate between closely related foods. [84] Madden et al. used Neural Networks and k-Nearest Neighbours for estimating the concentration of cocaine in solid mixtures. [85] Lopez-Diez et al. used multivariate and evolutionary computational-based methods to test the ability of Raman spectroscopy to discriminate between chemically very closely related oils and quantified hazelnut oils used to adulterate extra virgin olive oil using partial least squares and genetic programming. (3) Alharbi et al. combined surface-enhanced Raman scattering (SERS) with artificial neural networks to quantify caffeine and its two major metabolites theobromine and paraxanthine. [86] Muhamadali et al. combined chemometrics for detection and quantification of novel psychoactive substances. [87] These are some of the examples of studies that show the importance of combining the SERS with data driven approaches. In the present chapter, we try to achieve quantification capability using machine learning. We used the data sets generated from the SERS sensors to carry our supervised machine learning classification using support vector machine with quadratic kernel function to train the models. The data were generated using the sensor scheme shown in figure 4.1. As can be seen, the sensor was fabricated by functionalizing cysteamine linker molecule followed by gold nanostars. We fabricated 5 such sensors for each concentration to be tested. Three sensors were used for training purposes, while the remaining two were used for testing.

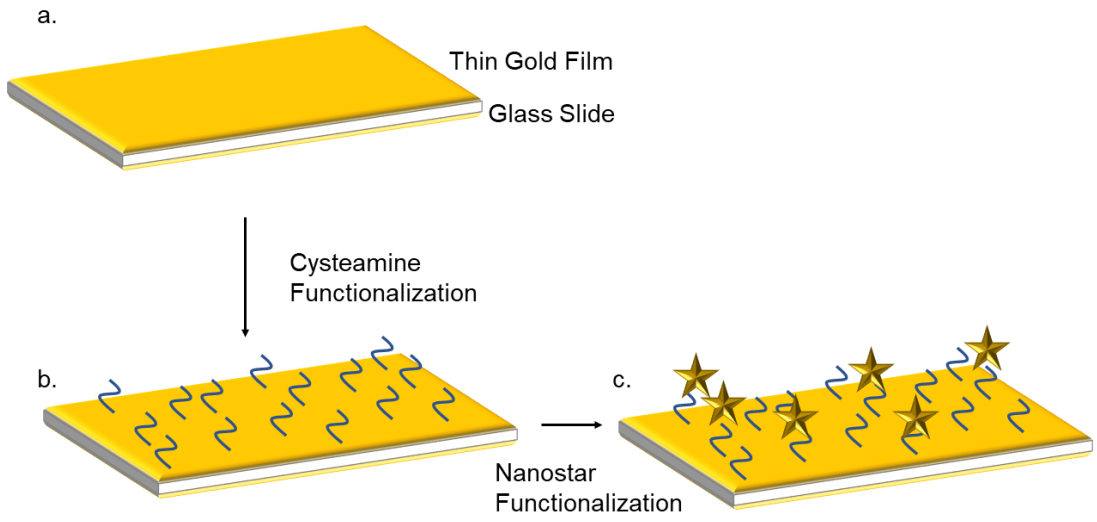

Figure 4.1: Sensor preparatio scheme. We first functionalize the thin-film- gold coated glass slides with cysteamine. Thereafter, the sensors are functionalized with nanostars to create a surface features that can provide high SERS enhancement.

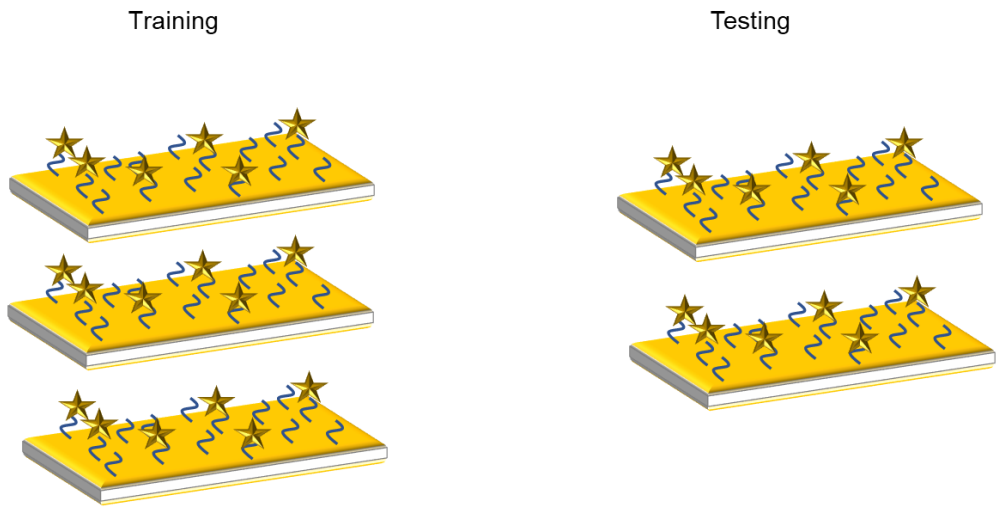

Figure 4.2: Data from three sensors were used to train the models and then the data from two sensors were used to test the models.

4.2 Materials and Methods

4.2.1 Materials and Instrumentation

Gold(III) chloride trihy-drate ($HAuCl_4.3H_2O$) was purchased from Acros Organics. Trisodium citrate dihydrate ($C_6H_5O_7Na.2H_2O$) was purchased from Acros Organics. Cysteamine and 4-aminothiophenol (4-ATP) were purchased from Sigma Aldrich. Ultrapure water (18.2 Mcm) was used for preparing the solutions. All glassware was aqua regia cleaned. The Raman spectra were obtained using a Renishaw InVia Raman microscope.

4.2.1.1 Surfactant free nanostar synthesis

Gold stock solution (2 ml of a 0.025 M $HAuCl_4.3H_2O$ solution) was added to 48 ml DI water being stirred. 200 μl of 1 N HCl was added to the solution, followed by 70 l of 15 nm gold nanospheres having 1 abs absorbance. Thereafter, 2 ml of 3 mM $AgNO_3$ and 1 ml of 100 mM ascorbic acid were added, simultaneously. The synthesis was stirred for additional 7 minutes.

4.2.1.2 Nanostars-based substrate preparation

Gold coated glass slides were incubated in 0.1 M aqueous cysteamine overnight and then washed with DI water. Next, 300μl of surfactant free gold nanostars with 0.2 absorbance for path length of 1 mm measurement were used for functionalization on this slide through incubation for two hours. The slides were then washed with DI water.

4.2.1.3 Sample preparation

Five sensors were prepared for each concentration of 4-ATP (0 nM, 1 nM, 10 nM, 100 nM, 1 uM, 10 uM, 100uM, 1 mM and 10 mM). Three sensors from the system were used for training purposes and the two remaining sensors were kept for testing purposes.

4.2.2 Datasets

In order to acquire the data, Raman mapping was carried out. Two maps in total with following specifications were taken on each sample: 80 μm x 80 μm with 20 μm step size.Figure 4.3 shows the map acquisition information of a sensor. In total 50 point measurements were collected on each sensor. The 50x 0.75NA objective lens was used for doing the measurements. 785 nm laser at 119.7μW laser power, 10 s exposure and 1 accumulation were used for the acquisition purposes.

Mathematically, the data collection process can be described as following. The data was acquired on nine different concentrations of analyte represented by C_i ,where i=$\{$*0 nM, 1 nM, 10 nM, 100 nM, 1 μM , 10 μM, 100 μM, 1mM, 10 mM*$\}$. For each of the concentrations, C_i, five sensors were fabricated denoted by $A_{i,j}$, where j=$\{$*1, 2, 3, 4, 5*$\}$. These sensors are assumed to be statistically independent. On each of these sensors,$A_{i,j}$, two maps were used that were collected at randomly chosen sites on the sensing substrate. These two sites are represented by $B_{i,j,k}$, where k=$\{$*1, 2*$\}$. The Raman map for each site consists of 25 point maps. Each point are statistically assumed to be independent of each other. The Raman point on a given map is denoted by $D_{i,j,k,l}$, where l=$\{$*1, 2, 3,....., 25*$\}$.

The spectra are individually baseline-subtracted using the msbackadj Matlab function. Figure 4.4 shows a generic spectrum before and after baseline subtraction. Subsequently, the highest intensity peaks from the following ranges: 1076 to 1084, 1579 to 1584, 1478 to 1488, 1170 to 1180 and 1000 to 1003 cm^{-1}, were extracted as these are some of the prominent characteristic peaks for Phe. In addition to this, the peak spectral locations was also extracted.

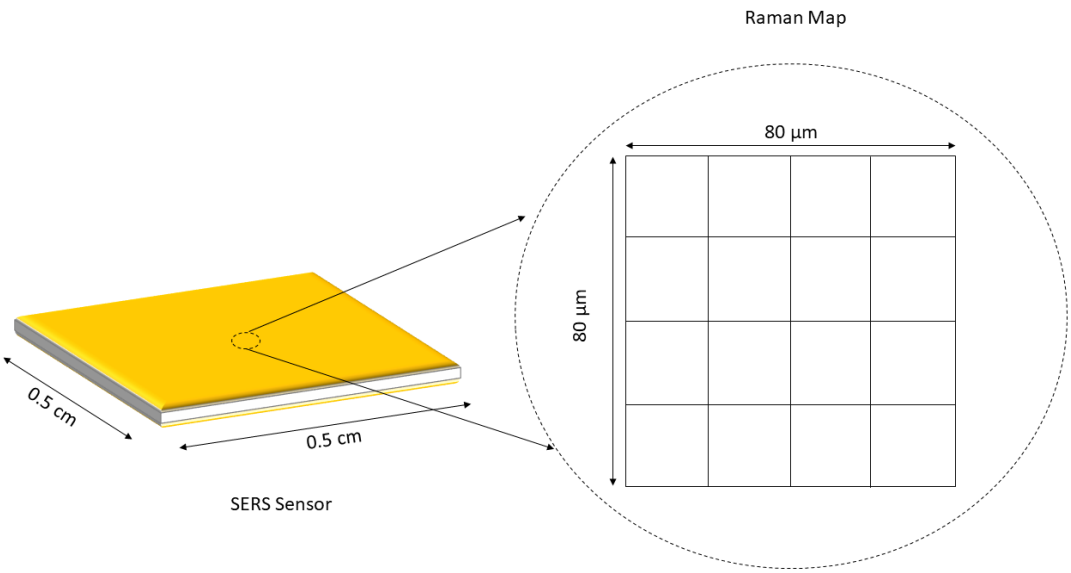

Figure 4.3: Raw spectrum collected for a point on the sensor. There is usually a background associated with these measurements. We carried out background subtraction using an built-in Matlab function. Blue plot shows the same spectrum after baseline subtraction.

4.3 Results and Discussions

In order to extract meaningful information from the spectrum for training purposes, we subtracted baseline form individual spectrum. Figure 4.4 shows the raw spectrum in red and baseline subtracted spectrum in blue. In order to do the analysis, we first worked with the Raman peak intensity at 1079 $cm^{-1}$and build calibration curve for it. We then discuss the shortcomings of this approach and quantification issues for concentration below certain range. Thereafter, in order to improve the quantification capability, we take the ratio of baseline subtracted Raman peak intensity to baseline. It gives us better quantification capability. Based on these comparison we chose 1079 cm^{-1}peak to be compared with the multiple peaks for supervised classification. Classification accuracy was first compared for 1 nM, 1μM and 1 mM 4-ATP for baseline-subtracted Raman peak intensities, scaled baseline subtracted peak intensities and log transformed peak intensities. Scaling was done based on the baseline variation in the spectrum. Based on

the best accuracy, the scaling and log transformation technique was chosen for the rest of the analysis. Next, performance of classifier using one the feature from 1079 cm^{-1} and features from multiple peak intensities we compared.

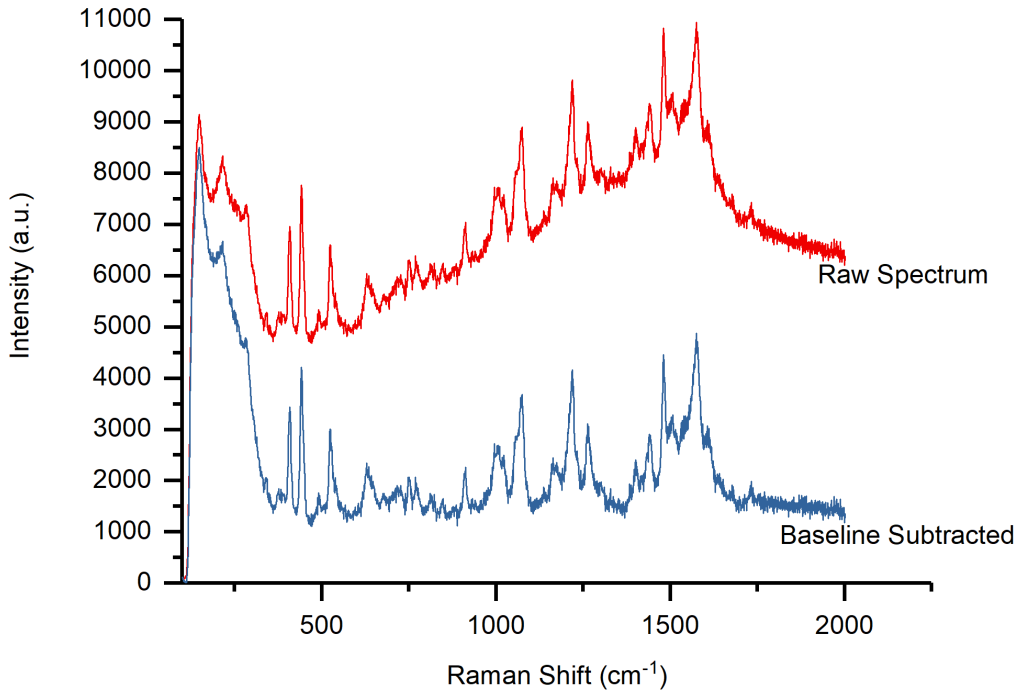

Figure 4.4: Raw spectrum collected for a point on the sensor. There is usually a background associated with these measurements. We carried out background subtraction using an built-in Matlab function. Blue plot shows the same spectrum after baseline subtraction.

In concentration dependent studies, characteristic peak from the spectrum is chosen that shows variation with concentration and hence, could be used for making the calibration curve. We chose to work with 4-ATP which is one of the most extensively studied Raman active molecule.The highest peak around 1079 cm^{-1} was extracted for each of the spectra and plotted against the concentration. Figure 4.5 shows the variation of peak intensity with concentration. Error bars show the standard error associated with each measurement.

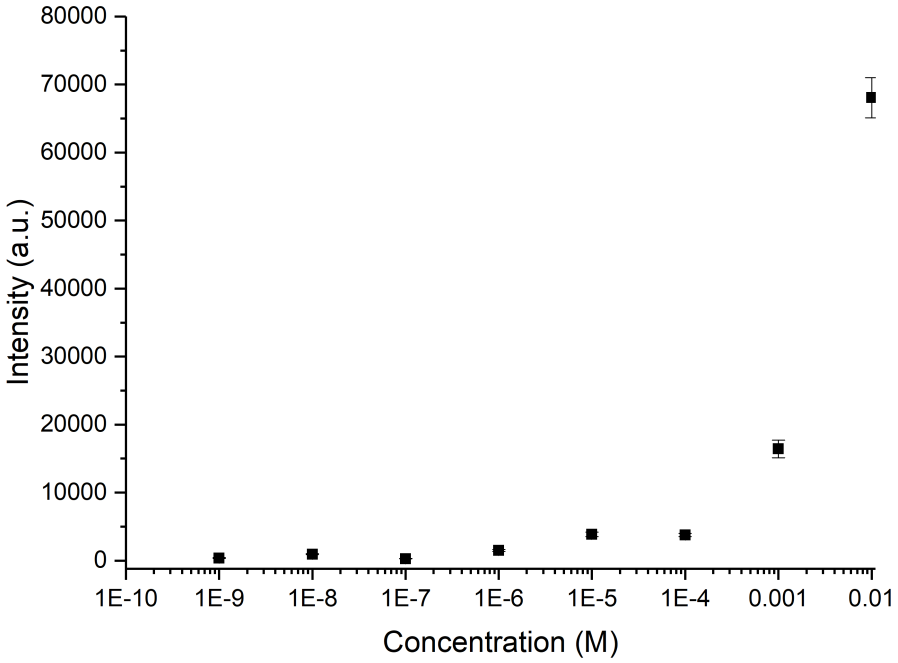

Figure 4.5: Variation of average Raman peak intensities with concentration for 1079 cm^{-1} peak location. Error bars show the standard error associated with measurements.

In order to improve the quantification capability, baseline-subtracted Raman intensity to baseline ratios were calculated for the data extracted. These values were plotted in figure 4.6 for peaks at 1003, 1180, 1488, and 1579 cm^{-1}. As can be seen different peaks follow different models for concentration to ratio of intensity to baseline . The average response decreases for 10 mM concentration for all the peaks except for the 1079 cm^{-1} peak. The peak at 10079 cm^{-1} shows better differentiation capability in than other peaks shown in the figure. The individual plots are plotted along with the error bars for ease of visualization.

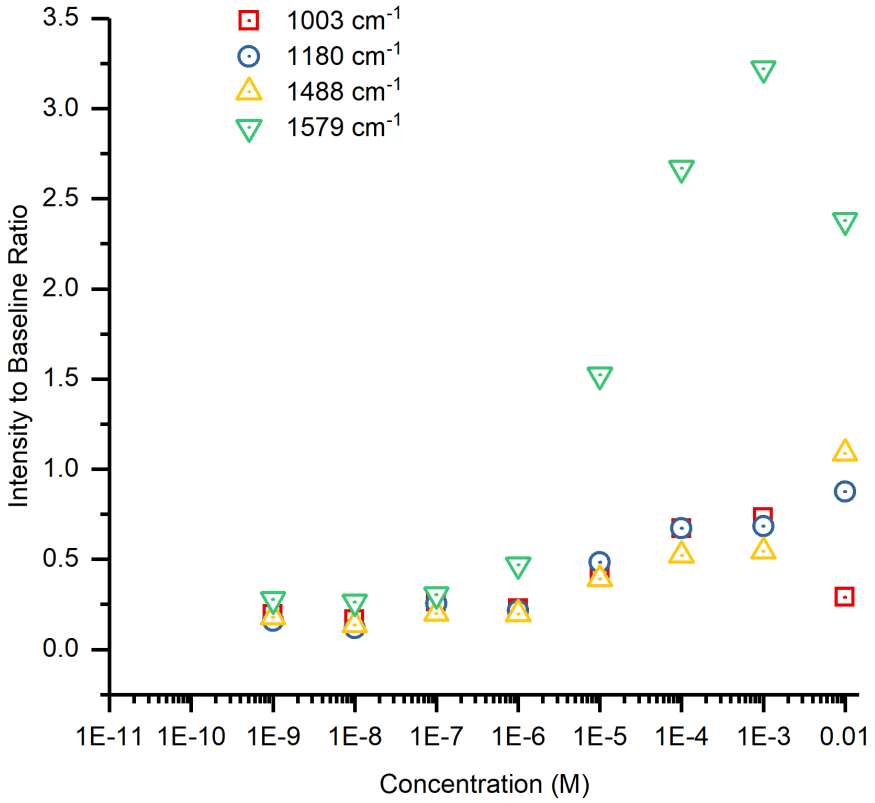

Figure 4.6: Variation of baseline subtracted Raman intensity to baseline ratio for peaks around 1003, 1180, 1488 and 1579 cm^{-1}

.

Figure 4.7, 4.8, and 4.9 shows the calibration curve for different ratios of baseline subtracted Raman intensity to baseline associated with different concentrations of analyte, for 1003, 1079, 1180, 1488 and 1579 cm^{-1} peaks. Figure 4.7 shows the calibration curves for 1003 and 1079 cm^{-1} peaks. There are high variations associated with 10 mM concentration for both the peaks. The error bars show standard deviation associated with each measurement from each concentration for three sensors. Both the calibration curves follow different models. We could not find good models that could assist in high precision quantification when considering the standard deviation associated.The 1079 cm^{-1} peak is one of the peaks which can provide good differentiation capability

between 1 μM, 10 μM and 100μM.

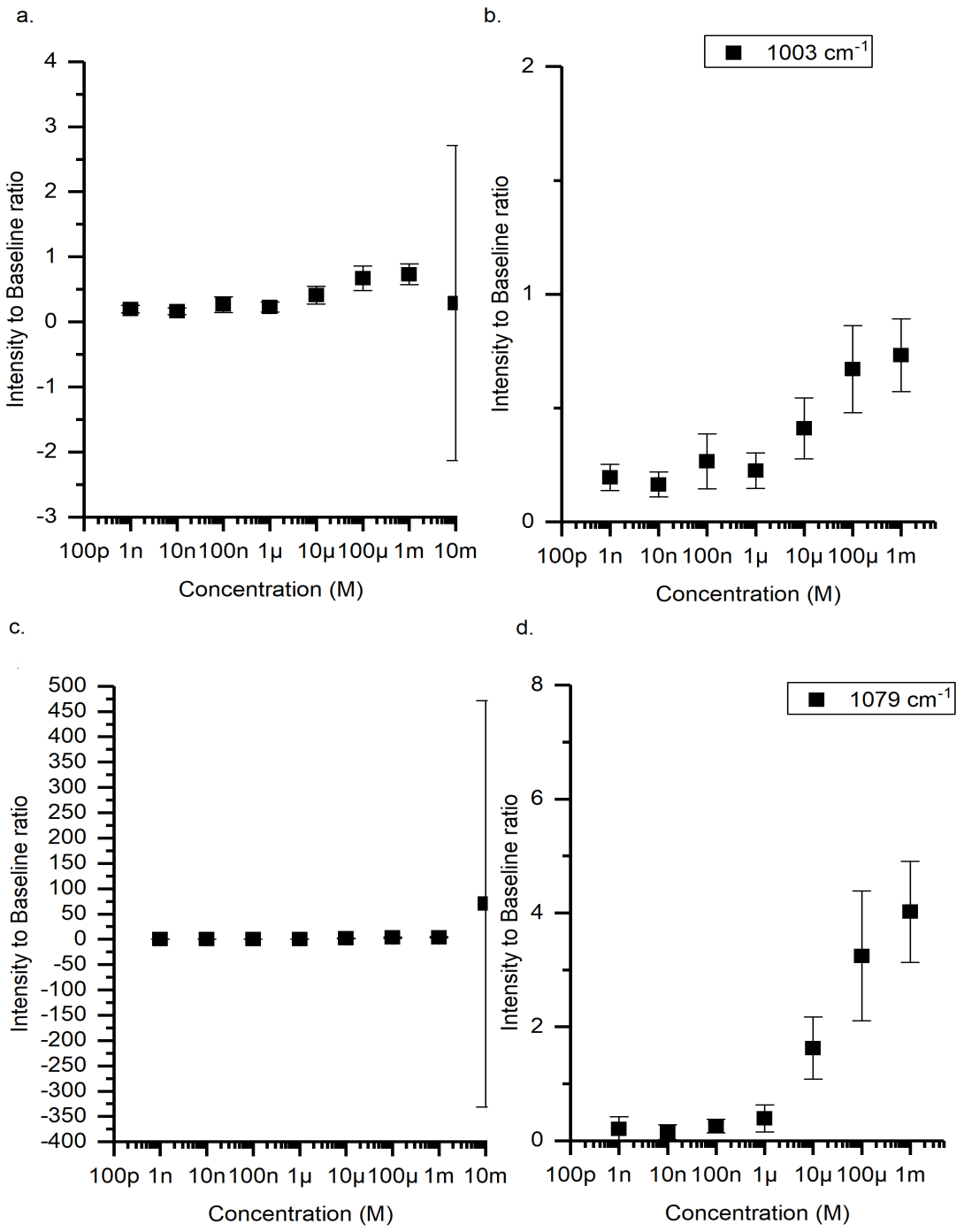

Figure 4.7: Calibration curve for baseline-subtracted Raman intensity to baseline ratio for peaks and their standard deviation for peaks around 1003(a and b) and 1079 (c and d)cm^{-1}. b. and c. are zoomed in versions to visualize the variation better.

.

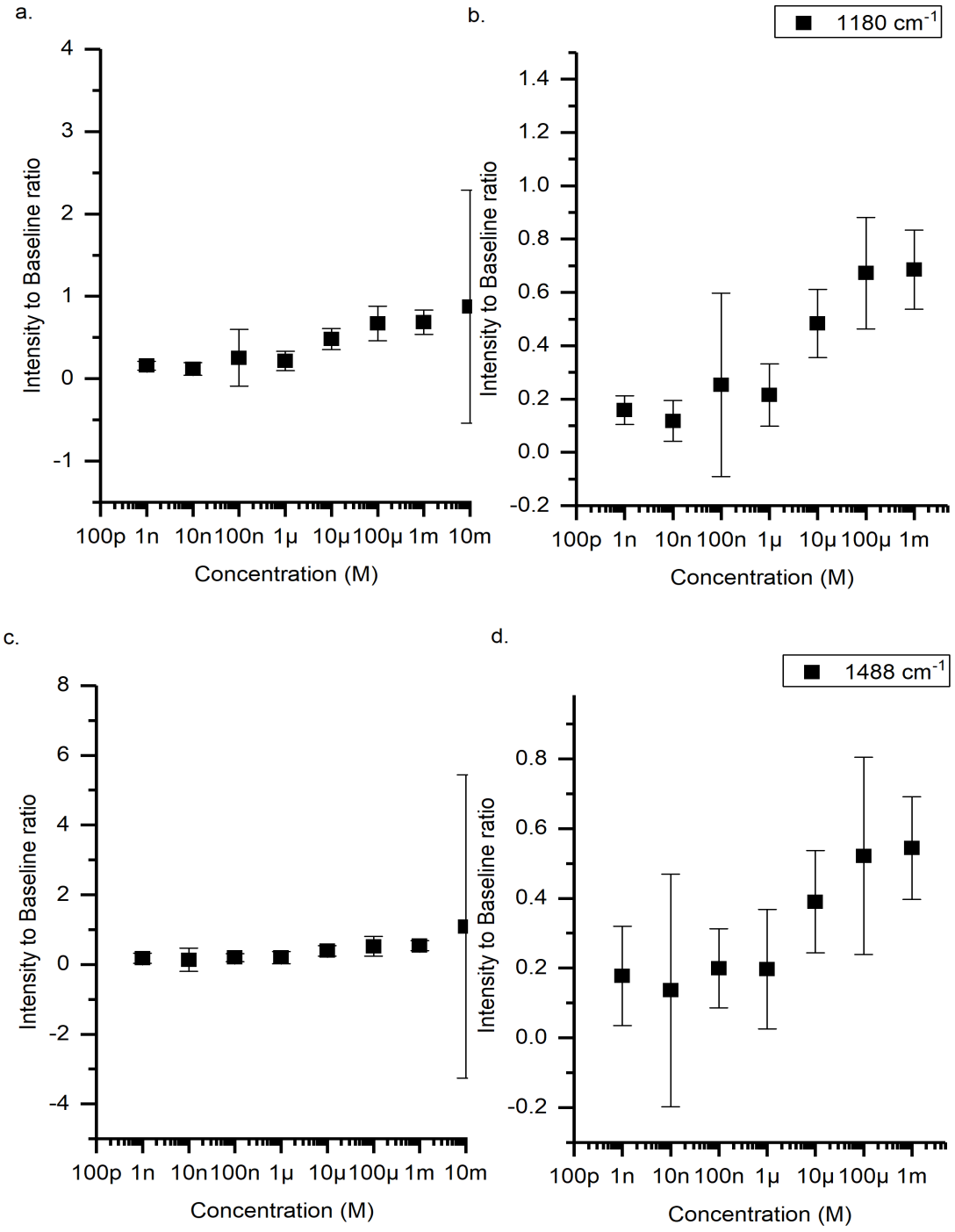

Figure 4.8: Calibration curve for baseline-subtracted Raman intensity to baseline ratio for peaks around 1180 (a and b) and 1488 (c and d)cm^{-1}. Error bars represent the standard deviation associated with the measurements.

.

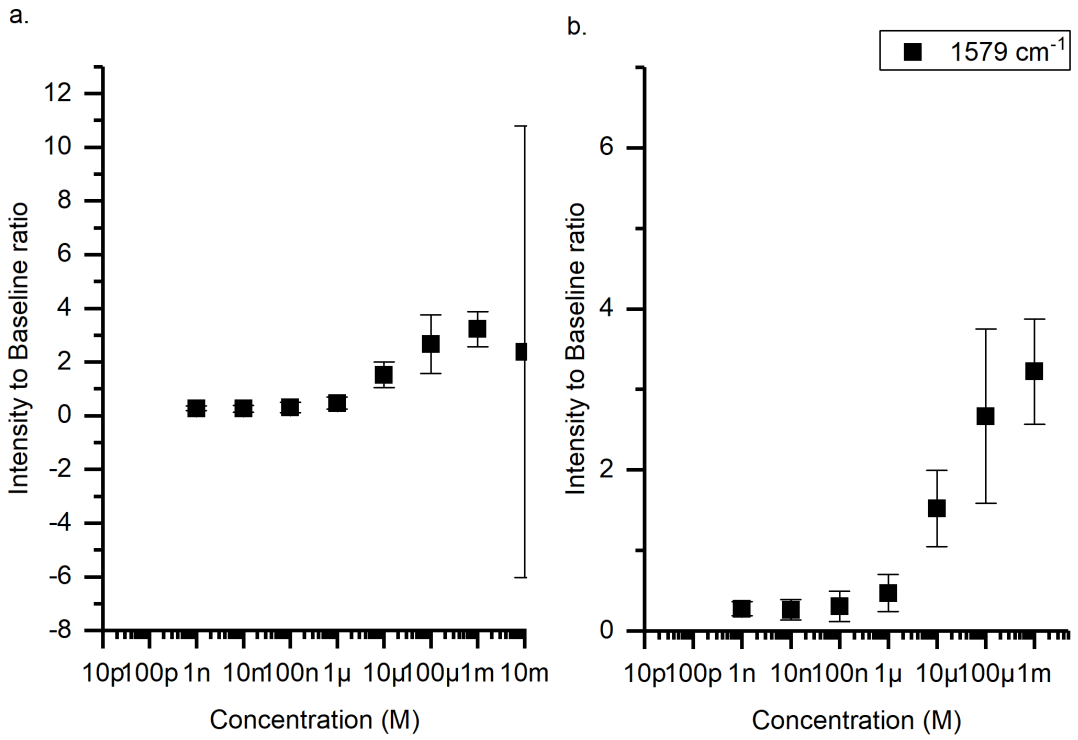

Figure 4.9: Calibration curve for baseline-subtracted Raman intensity to baseline ratio for peaks around 1579 cm^{-1}. Error bars represent the standard deviation associated with the measurement. Figure (a) shows the calibration for the entire range of concentration while (b) shows the zoomed-in version of calibration.

.

As can be seen from these calibration curves, quantification of the analyte is still a difficult task from a single point measurement. In the presented work we show that by combining the peak features from different peaks, we can predict 1000x and 100x increments in the test data with higher accuracy in comparison to using a single peak measurement. In order to achieve this,we carried out supervised machine learning for the training datasets taken from 3 sensors. Support vector machine (SVM) were used to understand the performance of the system. SVM is classifying the data using quadratic kernels. Intensity follows enhancements in fourth the power and therefore, the quadratic kernel was chosen. 5-fold validation was performed to prevent over-fitting during data training. We first trained the system with only the baseline subtracted peaks abstracted

from the system to understand the contribution from the peak intensities. Figure 4.10 shows the confusion matrix for the test data classified using the quadratic SVM model. The accuracy of the system was 89.8% for using 5-fold cross validation for training the data.

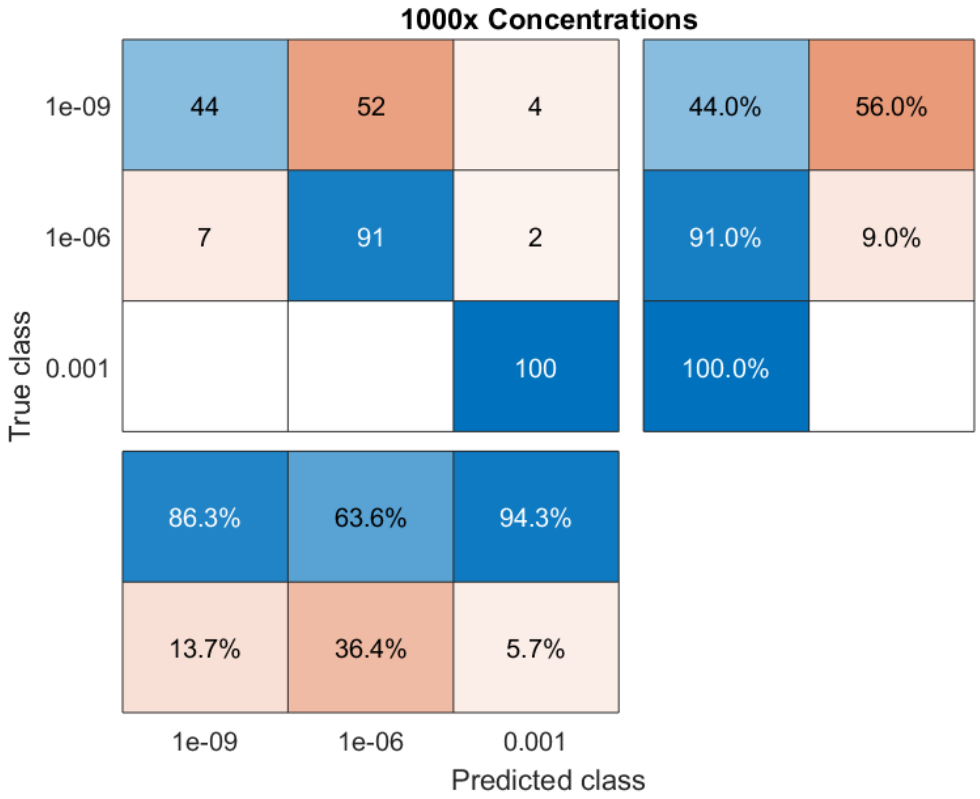

Figure 4.10: Confusion matrix for test data when the features used for training were the selected peaks after baseline subtraction. The concentrations have 1000x increments(1nM, 1 μM and 1 mM). The accuracy for classification for this SVM-based model was low, especially for nM and μM

.

As the classification accuracy was low, we scaled the data to improve the performance of the classifier. In order to scale the data, we chose baseline value at the Raman shift position of the highest peak intensity in the decided range and then scaled the intensities with that. When we trained the SVM models with scaled features, the accuracy increased to 92.2% for the 5-fold cross validated trained data. Figure 4.11 shows

the confusion matrix for the data tested from two different sensors.

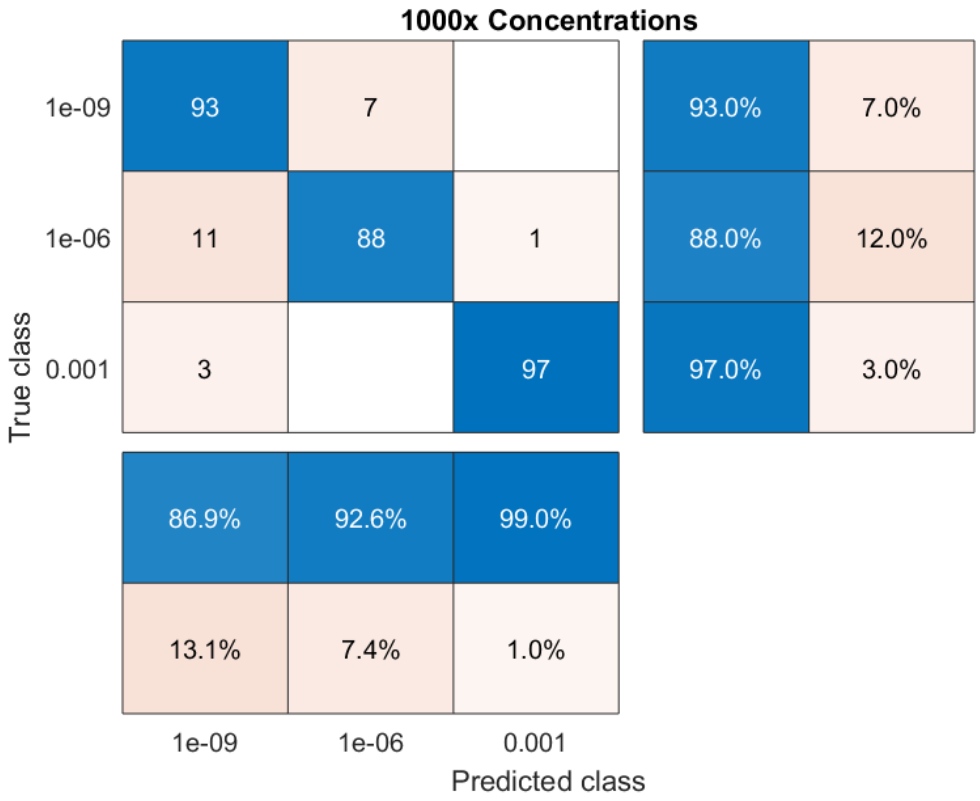

Figure 4.11: Confusion matrix for test data when the features used for training were the ratio of selected peaks after baseline subtraction to baseline. By taking the ratio, we are scaling the features through information present in the spectrum to improve the classification accuracy. The accuracy for classification for this SVM-based model increases for nM and μM concentration.

We further tried to increase the accuracy of the model being trained by log transforming the scaled data. We took the logarithm of the baseline-subtracted peak to baseline ratio and used these features for training the SVM model. As a result of this manipulation, the accuracy further increased to 96.7% for the 5-fold cross-validated trained data. Figure 4.12 shows the confusion matrix for the test data classified using the trained model. As can be seen, this model can classify analyte the concentrations from single point measurements without the need for data averaging.

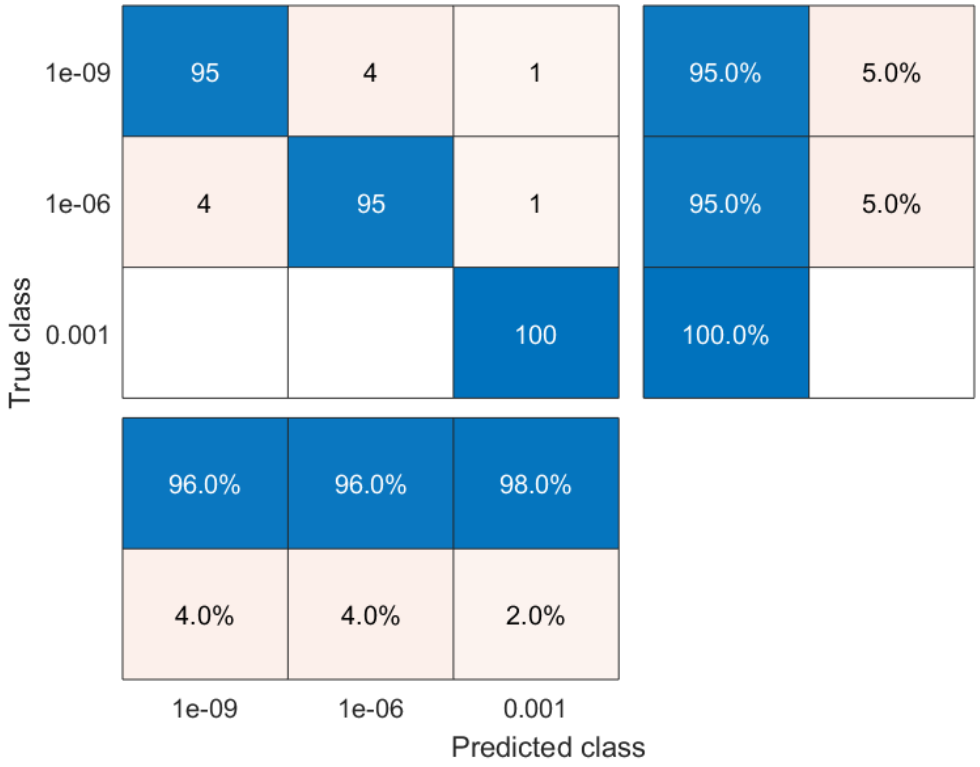

Figure 4.12: Confusion matrix for test data when the features used for training were the logarithm of the ratio of selected peaks after baseline subtraction to baseline. Log transformation of features was carried out by taking the logarithm of the ratio of peak intensity to baseline. As a result of log transformation, the accuracy for classification for this SVM-based model increases.

We also compared the performance of a multiple-peak model with the similar models created for the peak at 1079 cm^{-1}. The accuracy of this model for classification of 1nM, 1uM and 1mM concentrations was 94%. Figure 4.13 shows the prediction capability of the model from the single point measurements on the test sensor data.

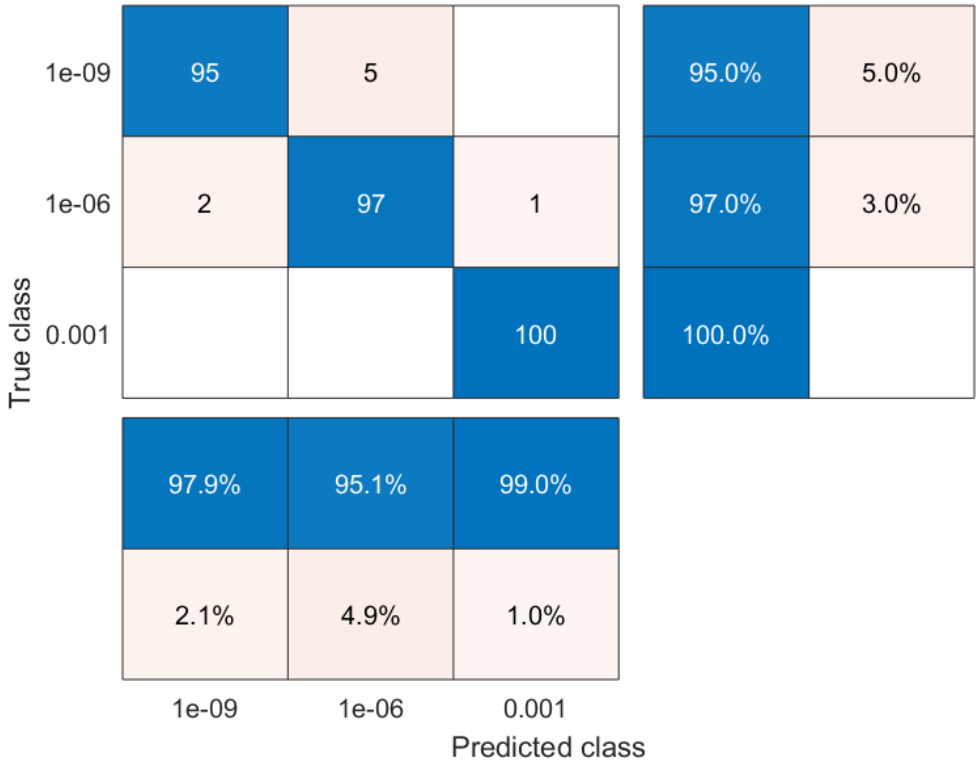

Figure 4.13: Confusion matrix for test data for classification at 1000x concentration increments (1 nM, 1μM and 1 mM) when the features taken from 1079 cm^{-1} using quadratic SVM model .

We find that the performance of the machine learning model using the logarithm of the baseline-subtracted Raman peak intensity to baseline ratio much better than what could be achieved using baseline-subtract Raman peak intensity to the baseline ratio. Next, we carried out the scaling and log transformation for classifying 100x concentration increments. Data from 0 nM, 10 nM, 1 μM and 100 μM were used for training quadratic SVM model. We found that the accuracy was 84.7 % for the 5-fold cross validated data trained for SVM. Figure 4.14 shows the confusion matrix for the classification carried out for test data.

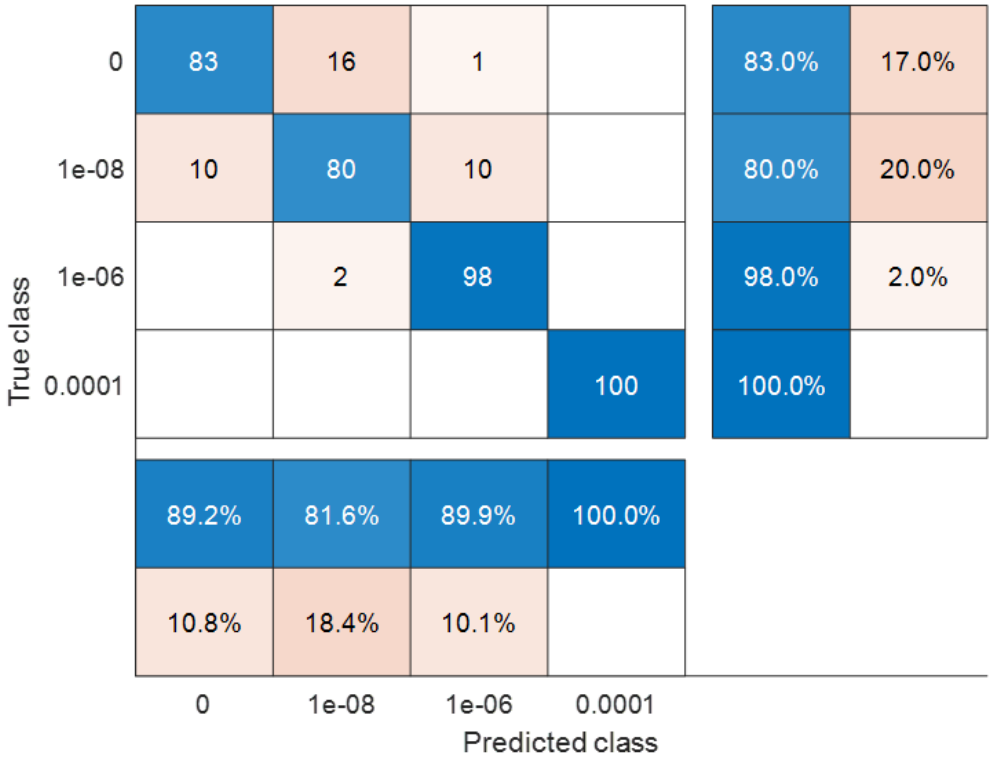

Figure 4.14: Confusion matrix for test data for classification of 100x (0 nM, 10nM, 1μM and 100μM)concentration increments when multiple scaled and Log transformed peaks (1003, 1079, 1180, 1488 and 1579 cm^{-1}) features were used for classification.

We compared this model for 100x concentration increments with the results obtained for the 1079 cm^{-1} peak model, which showed accuracy of 79.8% for 5-fold cross validated data trained. Figure 4.15 shows the prediction capability for the models using single point measurements from test sensors data.

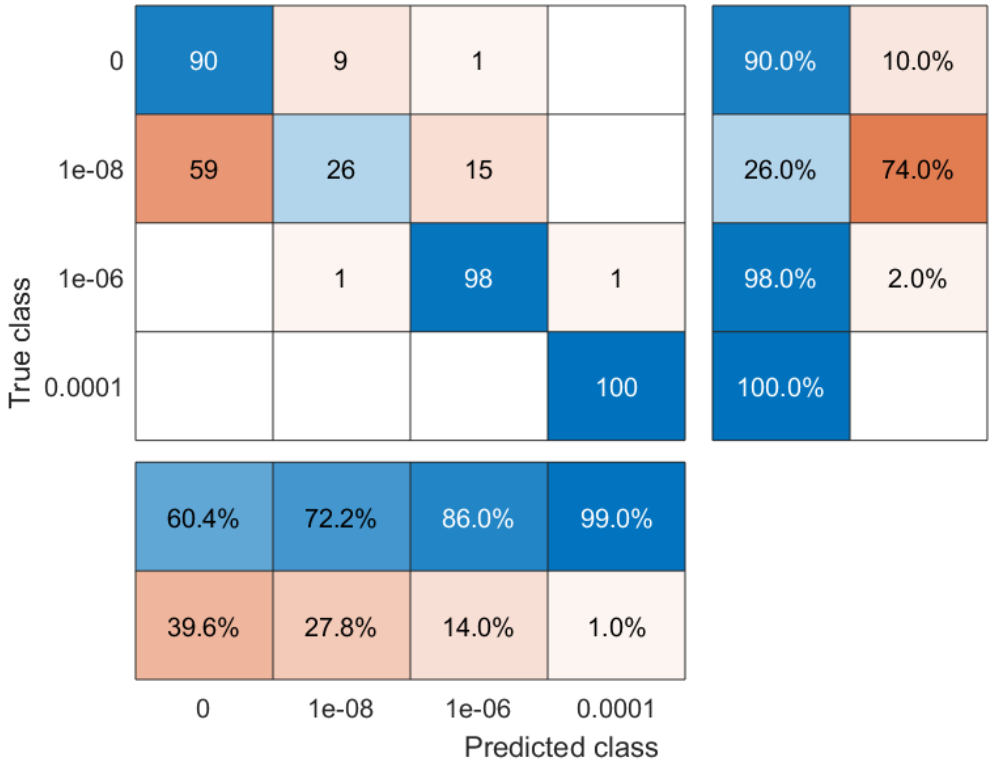

Figure 4.15: Confusion matrix for test data for classification of 100x (0 nM, 10nM, 1μM and 100μM)concentration increments when 1079 cm^{-1} scaled and Log transformed peak feature was used for classification.

Next, 100x increment model was also trained for 1 nM, 100nM, 10 μM and 1 mM concentrations for multiple peaks and for single 1079 cm^{-1} peak. The accuracy for multiple peak quadratic SVM model was 82.8% while that of the 1079 cm^{-1} was 76.2 %. Figure 4.16 and 4.17 shows the confusion matrix for the test data using multiple peaks and 1079 cm^{-1} peak model.

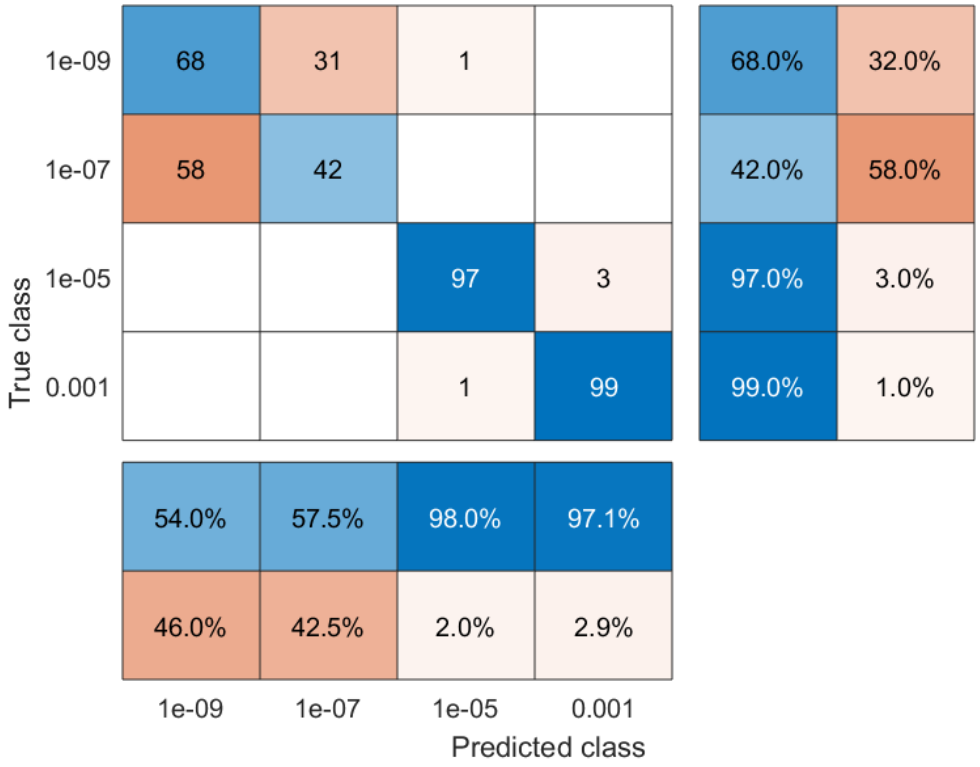

Figure 4.16: Confusion matrix for test data for classification at 100x (1 nM, 100nM, 10μM and 100mM)concentration increments when multiple scaled and Log transformed peaks features ((1003, 1079, 1180, 1488 and 1579 cm^{-1})were used for classification.

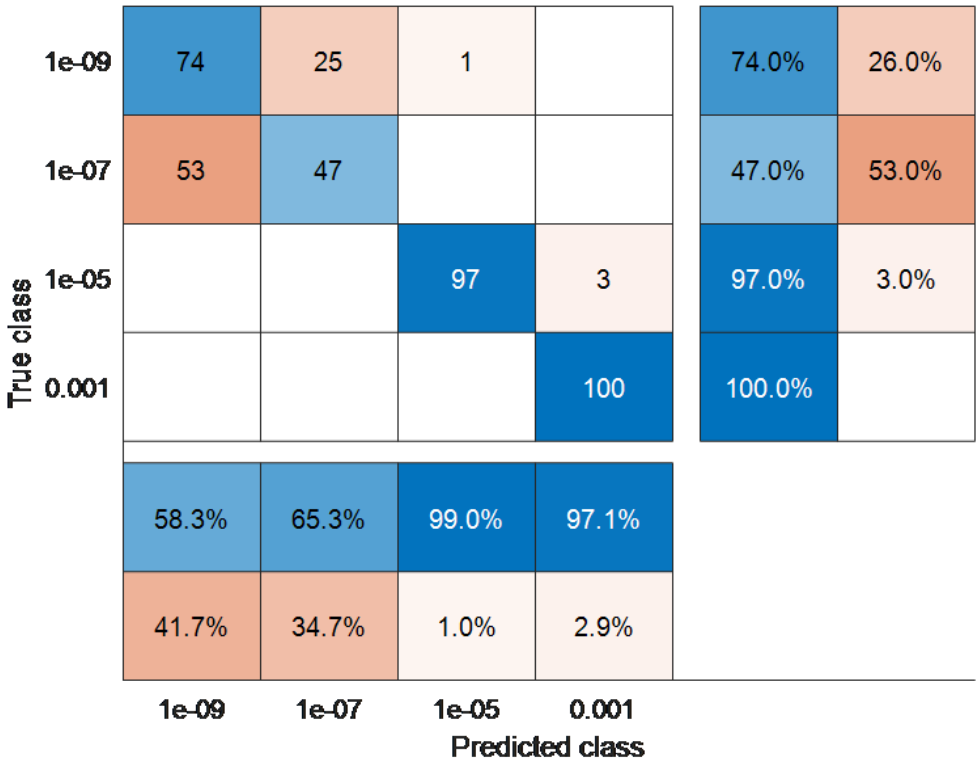

Figure 4.17: Confusion matrix for test data for classification at 100x (1 nM, 100nM, 10μM and 100mM)concentration increments when 1079 cm^{-1} scaled and Log transformed peak feature was used for classification.

A similar process for 10x increments for multiple peaks was carried out. The accuracy was calculated to be 72.6% for the 5-fold cross validated data trained for SVM. Figure 4.18 shows the confusion matrix for the classification done by the model for test data.

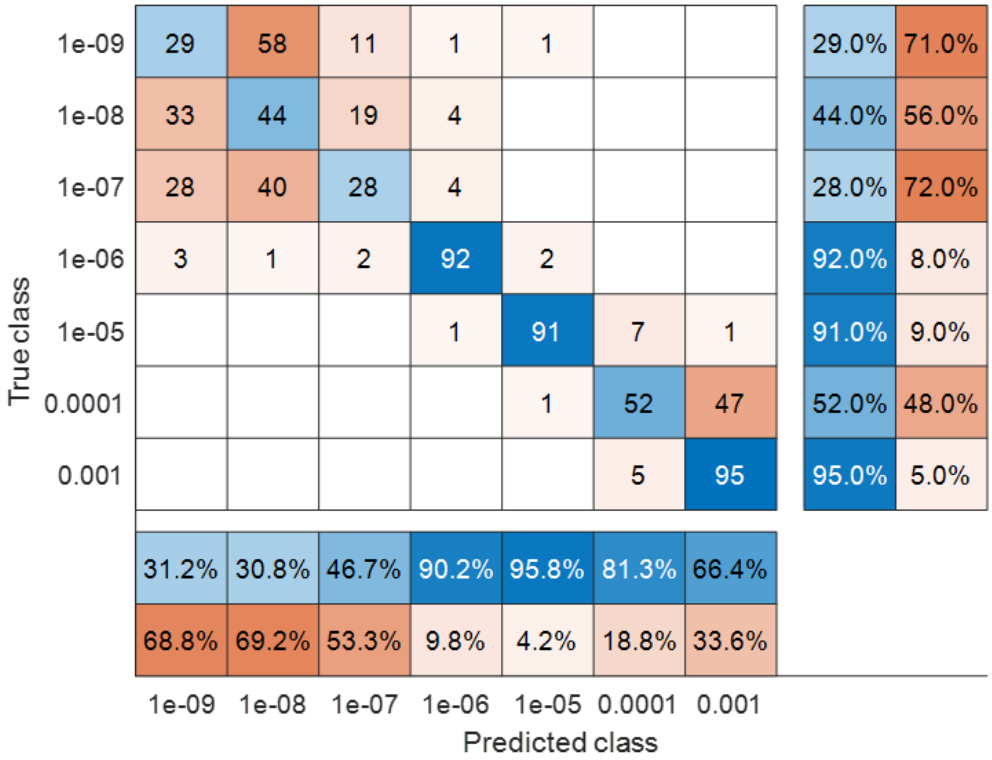

Figure 4.18: Confusion matrix for test data for classification at 10x concentration increments when the multiple peaks features (1003, 1079, 1180, 1488 and 1579 cm^{-1})were scaled and Log transformed.

Classification accuracy for 10x increments using 1079 cm^{-1} peak features was 51.9%. When comparing the prediction capabilities, models using multiple peaks feature perform better than the ones using features from only one peak (in our case 1079 cm^{-1}). Table 4.1 shows the summary of accuracies obtained with different models. We find that the performance of model increases as we scale the peak intensity data based on the baseline for each peak and also through log transformation. In addition, having multiple peaks performs better then single peak feature model.

S.No.	Model Trained	Peaks used	Accuracy
1.	1 nM, 1μM and 1 mM	Raman peak intensities at 1079, 1003, 1180,1488 and 1579 cm^{-1}	89.8%
2.	1 nM, 1μM and 1 mM	Scaled Raman peak intensities at 1079, 1003, 1180,1488 and 1579 cm^{-1}	92.2%
3.	1 nM, 1μM and 1 mM	Log transformed and scaled Raman peak intensities at 1079 cm^{-1}	94%
4.	1 nM, 1μM and 1 mM	Log transformed and scaled Raman peak intensities at 1079, 1003, 1180,1488 and 1579 cm^{-1}	96.6%
5.	0 nM, 10 nM, 1μM and 100μM	Log transformed and scaled Raman peak intensities at 1079 cm^{-1}	79.8%
6.	0 nM, 10 nM, 1μM and 100μM	Log transformed and scaled Raman peak intensities at 1079, 1003, 1180,1488 and 1579 cm^{-1}	84.7%
7.	1 nM, 100 nM, 10μM and 1 mM	Log transformed and scaled Raman peak intensities at 1079 cm^{-1}	76.2%
8.	1 nM, 100 nM, 10μM and 1 mM	Log transformed and scaled Raman peak intensities at 1079, 1003, 1180,1488 and 1579 cm^{-1}	82.8%
9.	10x concentration increments	Log transformed and scaled Raman peak intensities at 1079 cm^{-1}	51.9%
10.	10x concentration increments	Log transformed and scaled Raman peak intensities at 1079, 1003, 1180,1488 and 1579 cm^{-1}	72.6%

Table 4.1: Accuracy of different models trained using quadratic SVM

4.4 Conclusion and Future Directions

Our results shows that the prediction accuracy increases as we scale the individual peaks with the baseline. We see further improvements in classification accuracy for the log transformation of these features. We also show that the predictive accuracy from the single point measurements increase as we include multiple peaks for training rather than using a single peak. We find that the accuracy for the ensemble bagged trees is much superior to the quadratic SVM and even the prediction capability is very high for test data. However, the mechanistic reasoning behind it is yet to be understood.Future direction for the project would involve identifying classification methods to take into additional consideration based on the physics of the signal enhancement process of the sensor to render the algorithm more powerful.

Chapter 5

Conclusion and Future Work

In this chapter, I will be summarizing the results obtained and how they frame the future work that can be implemented to improve the system performance. We introduced a novel substrate-independent technique, dual-modality multi-site sensing, to improve the precision of SERS quantification. The overall reduction in the root mean squared error we obtained allows for better predictability in the determination of analyte concentration and has the potential to be used for quantification of important biomarkers, especially in point-of-care, low-cost assays. This approach also helps in predicting the expected intensity for a given concentration of analyte when there are changes in the underlying nanostructured substrates. Hence, it can help in overcoming the reproducibility issue associated with substrate morphology, a well-recognized issue in SERS. Further improved versions of our approach could represent solutions for such requirements; Improvements to this version could be made using low roughness surfaces to minimize the contribution from the supporting planer substrate. In addition, functionalization with nanoparticles like nanostars which have much higher SERS enhancements could also improve systems performance. In addition, this study provides means and motivation to explore some fundamental questions related to the determination of the Raman-active surface area of a SERS substrate using electrochemical techniques. Based on the few improvement studies, we concluded also that electrochemical measurements should better be performed after the Raman measurement for certain kinds of nanoparticles used. Future work would include optimizing the system for biomarker detection.. We also developed multiple methods for detection of Phe. We found that the detection response is highly dependent on the nanomaterials used for

the substrate preparation and the pH of the system. The combination of pH and substrate material can be used to create multi-site . Hence, it can provide different spectral features in the resulting spectra depending upon the varying molecular vibrations from one substrate to another . Thus, a combination of these could give robust information about the identity of the molecule being tested through different signature Raman peak enhancements . Finalized multi-site features included SWCNT-based sensing sites for neutral to slightly basic solution pH (9.8) and nanostar-based sensing sites for highly acidic and basic solutions. The future directions would involve testing the system out in complex matrix like urine to assess the system performance in realistic conditions. A robust sensing technique for this analyte could reduce the dependence on the monitoring Phe levels in blood, thus providing a simple, low-cost, non-invasive alternative. For machine learning with sensors, we found that the prediction accuracy increases as we scale the individual peaks with the baseline. This feature scaling is based on the information that is already embedded in the Raman spectra collected. We found further improvements in classification accuracy for the normalization of these features. We also found that the predictive accuracy from the single point measurements increases as we include multiple peaks for training rather than using a single peak. We found that the accuracy for the ensemble bagged trees is much superior to the quadratic SVM and even the prediction capability is very high for test data. However, the mechanistic reasoning behind it is yet to be understood. Another, area that could be explored is the identification of spectral signatures from changes in orientation of molecule of the nanoparticles . This could enable to understand the local environment of the spot on the substrate, in turn leading to real-time studies to understand the processes occurring on the substrate.

References

[1] E. C. Le Ru, M. Meyer, and P. G. Etchegoin. Proof of single-molecule sensitivity in surface enhanced raman scattering (sers) by means of a two-analyte technique. *The Journal of Physical Chemistry B*, 110(4):1944–1948, Feb 2006.

[2] Shikuan Yang, Xianming Dai, Birgitt Boschitsch Stogin, and Tak-Sing Wong. Ultrasensitive surface-enhanced raman scattering detection in common fluids. *Proceedings of the National Academy of Sciences*, 113(2):268–273, 2016.

[3] Bhavya Sharma, Renee R. Frontiera, Anne-Isabelle Henry, Emilie Ringe, and Richard P. Van Duyne. Sers: Materials, applications, and the future. *Materials Today*, 15(1):16 – 25, 2012.

[4] Jennifer A. Dougan and Karen Faulds. Surface enhanced raman scattering for multiplexed detection. *Analyst*, 137:545–554, 2012.

[5] Pamela A. Mosier-Boss. Review of sers substrates for chemical sensing. *Nanomaterials*, 7(6), 2017.

[6] Eric C. Le Ru and Pablo G. Etchegoin. Chapter 2 - raman spectroscopy and related optical techniques. In Eric C. Le Ru and Pablo G. Etchegoin, editors, *Principles of Surface-Enhanced Raman Spectroscopy*, pages 29 – 120. Elsevier, Amsterdam, 2009.

[7] Eric C. Le Ru and Pablo G. Etchegoin. Chapter 7 - metallic colloids and other sers substrates. In Eric C. Le Ru and Pablo G. Etchegoin, editors, *Principles of Surface-Enhanced Raman Spectroscopy*, pages 367 – 413. Elsevier, Amsterdam, 2009.

[8] Eric C. Le Ru and Pablo G. Etchegoin. Chapter 6 - em enhancements and plasmon resonances: examples and discussion. In Eric C. Le Ru and Pablo G. Etchegoin, editors, *Principles of Surface-Enhanced Raman Spectroscopy*, pages 299 – 365. Elsevier, Amsterdam, 2009.

[9] Xiang-Tian Kong, Zhiming Wang, and Alexander O. Govorov. Plasmonic nanostars with hot spots for efficient generation of hot electrons under solar illumination. *Advanced Optical Materials*, 5(15), 2017.

[10] Meral Yce and Hasan Kurt. How to make nanobiosensors: surface modification and characterisation of nanomaterials for biosensing applications. *RSC Adv.*, 7:49386–49403, 2017.

[11] Robert Surtees and Nenad Blau. The neurochemistry of phenylketonuria. *European Journal of Pediatrics*, 159(2):S109–S113, Sep 2000.

[12] Nenad Blau. Genetics of phenylketonuria: Then and now. *Human Mutation*, 37(6):508–515, 2016.

[13] Nenad Blau, Francjan J van Spronsen, and Harvey L Levy. Phenylketonuria. *The Lancet*, 376(9750):1417 – 1427, 2010.

[14] A. M. J. van Wegberg, A. MacDonald, K. Ahring, A. Bélanger-Quintana, N. Blau, A. M. Bosch, A. Burlina, J. Campistol, F. Feillet, M. Gizewska, S. C. Huijbregts, S. Kearney, V. Leuzzi, F. Maillot, A. C. Muntau, M. van Rijn, F. Trefz, J. H. Walter, and F. J. van Spronsen. The complete european guidelines on phenylketonuria: diagnosis and treatment. *Orphanet Journal of Rare Diseases*, 12(1):162, 2017.

[15] Anthony P. F. Turner. Biosensors: sense and sensibility. *Chem. Soc. Rev.*, 42:3184–3196, 2013.

[16] Ramn A. Alvarez-Puebla and Luis M. Liz-Marzn. Sers-based diagnosis and biodetection. *Small*, 6(5):604–610.

[17] Neus Feliu, Moustapha Hassan, Eduardo Garcia Rico, Daxiang Cui, Wolfgang Parak, and Ramon Alvarez-Puebla. Sers quantification and characterization of proteins and other biomolecules. *Langmuir*, 33(38):9711–9730, 2017. PMID: 28826207.

[18] Luca Guerrini, Elena Pazos, Cristina Penas, M. Eugenio Vzquez, Jose Luis Mascareas, and Ramon A. Alvarez-Puebla. Highly sensitive sers quantification of the oncogenic protein c-jun in cellular extracts. *Journal of the American Chemical Society*, 135(28):10314–10317, 2013. PMID: 23815097.

[19] Michael J. Natan. Concluding remarks surface enhanced raman scattering. *Faraday Discuss.*, 132:321–328, 2006.

[20] J. A. Guicheteau, A. Tripathi, E. D. Emmons, S. D. Christesen, and AugustusW. Fountain. Reassessing sers enhancement factors: using thermodynamics to drive substrate design. *Faraday Discuss.*, 205:547–560, 2017.

[21] E. C. Le Ru, E. Blackie, M. Meyer, and P. G. Etchegoin. Surface enhanced raman scattering enhancement factors: a comprehensive study. *The Journal of Physical Chemistry C*, 111(37):13794–13803, 2007.

[22] Md. Hakimul Haque, Ripon Bhattacharjee, Md. Nazmul Islam, Vinod Gopalan, Nam-Trung Nguyen, Alfred K. Lam, and Muhammad J. A. Shiddiky. Colorimetric and electrochemical quantification of global dna methylation using a methyl cytosine-specific antibody. *Analyst*, 142:1900–1908, 2017.

[23] Sabine Borgmann. Electrochemical quantification of reactive oxygen and nitrogen: challenges and opportunities. *Analytical and Bioanalytical Chemistry*, 394(1):95–105, May 2009.

[24] S. M. Alamouti. A simple transmit diversity technique for wireless communications. *IEEE Journal on Selected Areas in Communications*, 16(8):1451–1458, Oct 1998.

[25] Xiong Liu, Mark Atwater, Jinhai Wang, and Qun Huo. Extinction coefficient of gold nanoparticles with different sizes and different capping ligands. *Colloids and Surfaces B: Biointerfaces*, 58(1):3 – 7, 2007. Supramolecular Chemistry Applied to Interfaces.

[26] Michael C. Granger and Greg M. Swain. The influence of surface interactions on the reversibility of ferri/ferrocyanide at borondoped diamond thinfilm electrodes. *Journal of The Electrochemical Society*, 146(12):4551–4558, 1999.

[27] Scott H. Brewer, Wilhelm R. Glomm, Marcus C. Johnson, Magne K. Knag, and Stefan Franzen. Probing bsa binding to citrate-coated gold nanoparticles and surfaces. *Langmuir*, 21(20):9303–9307, 2005. PMID: 16171365.

[28] Ernesto J. Calvo and Alejandro Wolosiuk. Donnan permselectivity in layer-by-layer self-assembled redox polyelectrolye thin films. *Journal of the American Chemical Society*, 124(28):8490–8497, 2002. PMID: 12105931.

[29] Yi-Fan Huang, Hong-Ping Zhu, Guo-Kun Liu, De-Yin Wu, Bin Ren, and Zhong-Qun Tian. When the signal is not from the original molecule to be detected: Chemical transformation of para-aminothiophenol on ag during the sers measurement. *Journal of the American Chemical Society*, 132(27):9244–9246, 2010. PMID: 20527877.

[30] De-Yin Wu, Xiu-Min Liu, Sai Duan, Xin Xu, Bin Ren, Sheng-Hisen Lin, and Zhong-Qun Tian. Chemical enhancement effects in sers spectra: a quantum chemical study of pyridine interacting with copper, silver, gold and platinum metals. *The Journal of Physical Chemistry C*, 112(11):4195–4204, 2008.

[31] Yi-Fan Huang, De-Yin Wu, Hong-Ping Zhu, Liu-Bin Zhao, Guo-Kun Liu, Bin Ren, and Zhong-Qun Tian. Surface-enhanced raman spectroscopic study of p-aminothiophenol. *Phys. Chem. Chem. Phys.*, 14:8485–8497, 2012.

[32] Masatoshi Osawa, Naoki Matsuda, Katsumasa Yoshii, and Isamu Uchida. Charge transfer resonance raman process in surface-enhanced raman scattering from p-aminothiophenol adsorbed on silver: Herzberg-teller contribution. *The Journal of Physical Chemistry*, 98(48):12702–12707, 1994.

[33] N. Farsad, H. B. Yilmaz, A. Eckford, C. Chae, and W. Guo. A comprehensive survey of recent advancements in molecular communication. *IEEE Communications Surveys Tutorials*, 18(3):1887–1919, thirdquarter 2016.

[34] De-Yin Wu, Xiu-Min Liu, Yi-Fan Huang, Bin Ren, Xin Xu, and Zhong-Qun Tian. Surface catalytic coupling reaction of p-mercaptoaniline linking to silver nanostructures responsible for abnormal sers enhancement: A dft study. *The Journal of Physical Chemistry C*, 113(42):18212–18222, Oct 2009.

[35] Tai Ha Joo, Myung Soo Kim, and Kwan Kim. Surface-enhanced raman scattering of benzenethiol in silver sol. *Journal of Raman Spectroscopy*, 18(1):57–60, 1987.

[36] M. Baia, F. Toderas, L. Baia, J. Popp, and S. Astilean. Probing the enhancement mechanisms of sers with p-aminothiophenol molecules adsorbed on self-assembled gold colloidal nanoparticles. *Chemical Physics Letters*, 422(1):127 – 132, 2006.

[37] Jian Ye, James Andell Hutchison, Hiroshi Uji-i, Johan Hofkens, Liesbet Lagae, Guido Maes, Gustaaf Borghs, and Pol Van Dorpe. Excitation wavelength dependent surface enhanced raman scattering of 4-aminothiophenol on gold nanorings. *Nanoscale*, 4:1606–1611, 2012.

[38] Tie Wang, Rongbo Zheng, Xiaoge Hu, Lixue Zhang, and Shaojun Dong. Templated assembly of gold nanoparticles into microscale tubules and their application in surface-enhanced raman scattering. *The Journal of Physical Chemistry B*, 110(29):14179–14185, Jul 2006.

[39] Kazumasa Uetsuki, Prabhat Verma, Taka-aki Yano, Yuika Saito, Taro Ichimura, and Satoshi Kawata. Experimental identification of chemical effects in surface enhanced raman scattering of 4-aminothiophenol. *The Journal of Physical Chemistry C*, 114(16):7515–7520, Apr 2010.

[40] Masatoshi Osawa, Naoki Matsuda, Katsumasa Yoshii, and Isamu Uchida. Charge transfer resonance raman process in surface-enhanced raman scattering from p-aminothiophenol adsorbed on silver: Herzberg-teller contribution. *The Journal of Physical Chemistry*, 98(48):12702–12707, Dec 1994.

[41] Yi-Fan Huang, Meng Zhang, Liu-Bin Zhao, Jia-Min Feng, De-Yin Wu, Bin Ren, and Zhong-Qun Tian. Activation of oxygen on gold and silver nanoparticles assisted by surface plasmon resonances. *Angewandte Chemie International Edition*, 53(9):2353–2357, 2014.

[42] Mamdouh E. Abdelsalam, Philip N. Bartlett, Jeremy J. Baumberg, Suzanne Cintra, Tim A. Kelf, and Andrea E. Russell. Electrochemical sers at a structured gold surface. *Electrochemistry Communications*, 7(7):740 – 744, 2005.

[43] Yi-Fan Huang, De-Yin Wu, Hong-Ping Zhu, Liu-Bin Zhao, Guo-Kun Liu, Bin Ren, and Zhong-Qun Tian. Surface-enhanced raman spectroscopic study of p-aminothiophenol. *Phys. Chem. Chem. Phys.*, 14:8485–8497, 2012.

[44] R. S. Venkatachalam, F. J. Boerio, and P. G. Roth. Formation of p, p-azodibenzoate from p-aminobenzoic acid on silver island films during surface-enhanced raman scattering. *Journal of Raman Spectroscopy*, 19(4):281–287, 1988.

[45] Yi-Fan Huang, Hong-Ping Zhu, Guo-Kun Liu, De-Yin Wu, Bin Ren, and Zhong-Qun Tian. When the signal is not from the original molecule to be detected: Chemical transformation of para-aminothiophenol on ag during the sers measurement. *Journal of the American Chemical Society*, 132(27):9244–9246, Jul 2010.

[46] Sakshi Sardar, Laura Fabris, and Mehdi Javanmard. Improved precision in surface-enhanced raman scattering quantification of analyte through dual-modality multi-site sensing. *Analytical Chemistry*, 91(7):4323–4330, 2019. PMID: 30561991.

[47] Francjan J. van Spronsen, Annemiek MJ van Wegberg, Kirsten Ahring, Amaya Bélanger-Quintana, Nenad Blau, Annet M. Bosch, Alberto Burlina, Jaime Campistol, Francois Feillet, Maria Gizewska, Stephan C. Huijbregts, Shauna Kearney, Vincenzo Leuzzi, Francois Maillot, Ania C. Muntau, Fritz K. Trefz, Margreet van Rijn, John H. Walter, and Anita MacDonald. Key european guidelines for the

diagnosis and management of patients with phenylketonuria. *The Lancet Diabetes & Endocrinology*, 5(9):743–756, 2017.

[48] Irina V. Zaporotskova, Natalia P. Boroznina, Yuri N. Parkhomenko, and Lev V. Kozhitov. Carbon nanotubes: Sensor properties. a review. *Modern Electronic Materials*, 2(4):95 – 105, 2016.

[49] L. Valentini, C. Cantalini, I. Armentano, J.M. Kenny, L. Lozzi, and S. Santucci. Highly sensitive and selective sensors based on carbon nanotubes thin films for molecular detection. *Diamond and Related Materials*, 13(4):1301 – 1305, 2004. 14th European Conference on Diamond, Diamond-Like Materials, Carbon Nanotubes, Nitrides and Silicon Carbide.

[50] Qing Cao and John A. Rogers. Ultrathin films of single-walled carbon nanotubes for electronics and sensors: A review of fundamental and applied aspects. *Advanced Materials*, 21(1):29–53, 2009.

[51] Luca Camilli and Maurizio Passacantando. Advances on sensors based on carbon nanotubes. *Chemosensors*, 6(4), 2018.

[52] Erik T Thostenson, Zhifeng Ren, and Tsu-Wei Chou. Advances in the science and technology of carbon nanotubes and their composites: a review. *Composites Science and Technology*, 61(13):1899 – 1912, 2001.

[53] Prabhakar R. Bandaru. Electrical properties and applications of carbon nanotube structures. *Journal of Nanoscience and Nanotechnology*, 7(4-5):1239–1267, 2007.

[54] Qifeng Zhou, Jing Zheng, Zhihe Qing, Mengjie Zheng, Jinfeng Yang, Sheng Yang, Le Ying, and Ronghua Yang. Detection of circulating tumor dna in human blood via dna-mediated surface-enhanced raman spectroscopy of single-walled carbon nanotubes. *Analytical Chemistry*, 88(9):4759–4765, May 2016.

[55] Seunghyun Lee, Myung Gwan Hahm, Robert Vajtai, Daniel P. Hashim, Theerapol Thurakitseree, Alin Cristian Chipara, Pulickel M. Ajayan, and Jason H. Hafner. Utilizing 3d sers active volumes in aligned carbon nanotube scaffold substrates. *Advanced Materials*, 24(38):5261–5266, 2012.

[56] Xiaojing Wang, Chao Wang, Liang Cheng, Shuit-Tong Lee, and Zhuang Liu. Noble metal coated single-walled carbon nanotubes for applications in surface enhanced raman scattering imaging and photothermal therapy. *Journal of the American Chemical Society*, 134(17):7414–7422, May 2012.

[57] Alexey Yashchenok, Admir Masic, Dmitry Gorin, Bong Sup Shim, Nicholas A. Kotov, Peter Fratzl, Helmuth Mhwald, and Andre Skirtach. Nanoengineered colloidal probes for raman-based detection of biomolecules inside living cells. *Small*, 9(3):351–356, 2013.

[58] Nathaniel L. Rosi and Chad A. Mirkin. Nanostructures in biodiagnostics. *Chemical Reviews*, 105(4):1547–1562, Apr 2005.

[59] Narges Elahi, Mehdi Kamali, and Mohammad Hadi Baghersad. Recent biomedical applications of gold nanoparticles: A review. *Talanta*, 184:537 – 556, 2018.

[60] John Turkevich, Peter Cooper Stevenson, and James Hillier. A study of the nucleation and growth processes in the synthesis of colloidal gold. *Discuss. Faraday Soc.*, 11:55–75, 1951.

[61] Xiaohui Ji, Xiangning Song, Jun Li, Yubai Bai, Wensheng Yang, and Xiaogang Peng. Size control of gold nanocrystals in citrate reduction: The third role of citrate. *Journal of the American Chemical Society*, 129(45):13939–13948, Nov 2007.

[62] Anand Gole and Catherine J. Murphy. Seed-mediated synthesis of gold nanorods: Role of the size and nature of the seed. *Chemistry of Materials*, 16(19):3633–3640, Sep 2004.

[63] Agampodi S. De Silva Indrasekara, Sean F. Johnson, Ren A. Odion, and Tuan Vo-Dinh. Manipulation of the geometry and modulation of the optical response of surfactant-free gold nanostars: A systematic bottom-up synthesis. *ACS Omega*, 3(2):2202–2210, Feb 2018.

[64] Xiao-Shan Zheng, Izabella Jolan Jahn, Karina Weber, Dana Cialla-May, and Jrgen Popp. Label-free sers in biological and biomedical applications: Recent progress, current challenges and opportunities. *Spectrochimica Acta Part A: Molecular and Biomolecular Spectroscopy*, 197:56 – 77, 2018. Festschrift in honor of Prof. Yukihiro Ozaki.

[65] Lingyu Piao, Quanrun Liu, Yongdan Li, and Chen Wang. Adsorption of l-phenylalanine on single-walled carbon nanotubes. *The Journal of Physical Chemistry C*, 112(8):2857–2863, 2008.

[66] Qi Dong Zhang, Benoît Piro, Vincent Noël, Steeve Reisberg, and Minh-Chau Pham. Applications of carbon nanotubes to electrochemical dna sensors: a new strategy to make direct and selective hybridization detection from swnts. 1(4):045011, 2011.

[67] Ramon A. Alvarez-Puebla and Luis M. Liz-Marzn. Traps and cages for universal sers detection. *Chem. Soc. Rev.*, 41:43–51, 2012.

[68] Akira Harada, Ying Hu, Shyoko Yamamoto, and Shigetoshi Takahashi. Preparation and properties of inclusion compounds of ferrocene and its derivatives with cyclodextrins. *J. Chem. Soc., Dalton Trans.*, pages 729–732, 1988.

[69] Yinghui Bian, Guifen Zhang, Xian Zhong, Demei Tian, and Haibing Li. Enantioselective recognition of electrochemically inactive phenylalanine by thiolated-cyclodextrin/ferrocene-coated gold nanoparticles. *Supramolecular Chemistry*, 23(6):455–461, 2011.

[70] Yasuhiro Domi, Yusuke Yoshinaga, Katsuaki Shimazu, and Marc D. Porter. Characterization and optimization of mixed thiol-derivatized b-cyclodextrin/pentanethiol monolayers with high-density guest-accessible cavities. *Langmuir*, 25(14):8094–8100, Jul 2009.

[71] Ramon A. Alvarez-Puebla and Luis M. Liz-Marzn. Traps and cages for universal sers detection. *Chem. Soc. Rev.*, 41:43–51, 2012.

[72] J. Bodenheimer, E. Loewenthal, and W. Low. The raman spectra of ferrocene. *Chemical Physics Letters*, 3(9):715 – 716, 1969.

[73] J.S. Bodenheimer and W. Low. A vibrational study of ferrocene and ruthenocene. *Spectrochimica Acta Part A: Molecular Spectroscopy*, 29(9):1733 – 1743, 1973.

[74] Animesh K. Ojha, Achintya Singha, Swagata Dasgupta, Ranjan K. Singh, and Anushree Roy. ph dependent surface enhanced raman study of phe+ag complex and dft calculations for spectral analysis. *Chemical Physics Letters*, 431(1):121 – 126, 2006.

[75] Barbara Fazio, Cristiano D'Andrea, Antonino Foti, Elena Messina, Alessia Irrera, Maria Grazia Donato, Valentina Villari, Norberto Micali, Onofrio M. Maragò, and Pietro G. Gucciardi. Sers detection of biomolecules at physiological ph via aggregation of gold nanorods mediated by optical forces and plasmonic heating. *Scientific Reports*, 6:26952 EP –, Jun 2016. Article.

[76] Beulah J.M Rajkumar and V Ramakrishnan. Infrared and laser raman studies of l-phenylalanine l-phenylalaninium perchlorate and bis(dl-phenylalaninium) sulphate monohydrate. *Spectrochimica Acta Part A: Molecular and Biomolecular Spectroscopy*, 58(9):1923 – 1934, 2002.

[77] S Stewart and P.M Fredericks. Surface-enhanced raman spectroscopy of amino acids adsorbed on an electrochemically prepared silver surface. *Spectrochimica Acta Part A: Molecular and Biomolecular Spectroscopy*, 55(7):1641 – 1660, 1999.

[78] Sang Kyu Kim, Myung Soo Kim, and Se Won Suh. Surface-enhanced raman scattering (sers) of aromatic amino acids and their glycyl dipeptides in silver sol. *Journal of Raman Spectroscopy*, 18(3):171–175, 1987.

[79] Beln Hernndez, Fernando Pflger, Sergei G. Kruglik, and Mahmoud Ghomi. Characteristic raman lines of phenylalanine analyzed by a multiconformational approach. *Journal of Raman Spectroscopy*, 44(6):827–833, 2013.

[80] Guangyong Zhu, Xian Zhu, Qi Fan, and Xueliang Wan. Raman spectra of amino acids and their aqueous solutions. *Spectrochimica Acta Part A: Molecular and Biomolecular Spectroscopy*, 78(3):1187 – 1195, 2011.

[81] Grace Lu, Binaya Shrestha, and Amanda J. Haes. Importance of tilt angles of adsorbed aromatic molecules on nanoparticle rattle sers substrates. *The Journal of Physical Chemistry C*, 120(37):20759–20767, Sep 2016.

[82] Keith T. Carron and L. Gayle Hurley. Axial and azimuthal angle determination with surface-enhanced raman spectroscopy: thiophenol on copper, silver, and gold metal surfaces. *The Journal of Physical Chemistry*, 95(24):9979–9984, Nov 1991.

[83] Xiaoping Gao, John P. Davies, and Michael J. Weaver. Test of surface selection rules for surface-enhanced raman scattering: the orientation of adsorbed benzene and monosubstituted benzenes on gold. *The Journal of Physical Chemistry*, 94(17):6858–6864, Aug 1990.

[84] David I. Ellis, David Broadhurst, Sarah J. Clarke, and Royston Goodacre. Rapid identification of closely related muscle foods by vibrational spectroscopy and machine learning. *Analyst*, 130:1648–1654, 2005.

[85] Alan G. Ryder Michael G. Madden. Machine learning methods for quantitative analysis of raman spectroscopy data, 2003.

[86] Omar Alharbi, Yun Xu, and Royston Goodacre. Simultaneous multiplexed quantification of caffeine and its major metabolites theobromine and paraxanthine using surface-enhanced raman scattering. *Analytical and bioanalytical chemistry*, 407(27):8253–8261, 2015. 26345445[pmid].

[87] Howbeer Muhamadali, Alexandra Watt, Yun Xu, Malama Chisanga, Abdu Subaihi, Carys Jones, David I. Ellis, Oliver B. Sutcliffe, and Royston Goodacre. Rapid detection and quantification of novel psychoactive substances (nps) using raman spectroscopy and surface-enhanced raman scattering. *Frontiers in Chemistry*, 7:412, 2019.